PhD Thesis

Photovoltaic Power Converters for Large Scale Applications

Cristian Verdugo Retamal

Barcelona, April 2021

Photovoltaic Power Converters for Large Scale Applications

Cristian Verdugo Retamal

Dissertation submitted to the PhD Doctorate Office of the Universitat Politècnica de Catalunya in partial fulfillment of the requirements for the degree of Doctor of Philosophy by the

UNIVERSIDAD DE MÁLAGA

UNIVERSIDAD DE SEVILLA

UNIVERSIDAD DEL PAÍS VASCO/EUSKAL ERRIKO UNIBERTSITATEA

UNIVERSITAT POLITÈCNICA DE CATALUNYA

Joint Doctoral Programme in

Electric Energy Systems

Barcelona, April 2021

Photovoltaic Power Converters for Large Scale Applications

Printed by the UPC
Barcelona, April 2021

ISBN:–.
Research Project: ENE2017-88889-C2-1-R
H2020-LCE-2016-2017-SGS-774407

UNIVERSITAT POLITÈCNICA DE CATALUNYA
Escola de Doctorat
Edifici Vertex. Pl. Eusebi Güell, 6
08034 Barcelona.
Web: http://www.upc.edu

UNIVERSIDAD DE MALAGA
Escuela de Doctorado
Pabellón de Gobierno - Plaza el Ejido s/n
(29013) Málaga.
Web: http://www.uma.es

UNIVERSIDAD DE SEVILLA
Escuela Internacional de Doctorado
Pabellón de México - Paseo de las Delicias, s/n
41013 Sevilla.
Web: http://www.us.es

UNIVERSIDAD DEL PAÍS VASCO/EUSKAL ERRIKO UNIBERTSITATEA
Escuela de Master y Doctorado
Edificio Aulario II - Barrio Sarriena, s/n
48940- Leioa (Bizkaia) Spain.
Web: http://www.ehu.eus/es

To my wife Magda

Acknowledgements

I would like to thank my supervisor, Prof. Pedro Rodriguez Cotes, for providing me the opportunity to carry out my PhD at the Polytechnic University of Catalunya. His guidance and critical but constructive comments gave me the strength to get through this program.

I would also like to thank my co-supervisor Dr. Jose Ignacio Candela for always being there to support me during this journey. I really appreciate your endless patience and complete availability to discuss any topic. Your enthusiasm and deep knowledge in many topics kept me all the time with the desire to improve and learn more.

My sincere gratitude to Dr. Alvaro Luna for his advice and continuously reminding me to publish. Without his accurate comments during writing papers, it would have been more difficult to get through all challenges. I also thank you for being there to support and provide us a perfect environment for working.

My acknowledgments to Dr. Joan Rocabert for being an important cornerstone of the group. Without your designs and laboratory equipment, it would be more difficult to carry out our experiments.

I would also like to thank Khadija for supporting me in the organizational and administrative processes during my time in Spain. With your help all the bureaucracy processes were managed more quickly.

I express my special gratitude to all people at SEER. In special to my PhD fellows: Andres Tarrasó, Leonardo Marin, Mohamed Atef, Weiyi Zhang, Nurul Rosland, Mosfafa Abdullahi and Kumars Rouzbehi for the time we spent together not only in the office, but also in social circumstances. You guys made my PhD program more pleasant. I also thank

Borja Garcia, Josep Oltra, Dr. Mahdi Shahparasti, Raul Muñoz, Ruben Capo and Victor Fauquet for your absolute support.

Many thanks to Dr. Rodrigo Alvarez for providing me the opportunity to conduct my PhD internship at Siemens in the Transmission Solution division. This experience gave me the chance to put in practice all the knowledge I have learnt during the last years, and also to see how research is conducted in such amazing company.

To my family who have supported me during these years, thank you for understanding the effort needed to succeed in this journey. I really sorry for not being there in special moments but, nonetheless, you always have tried to make me feel as if I were at home. I really appreciate that.

Finally, these last words are specially for my wife who has been with me from the beginning of this process. Magda, thank you for providing me unconditional support, for being strong when I felt tired and for being my partner in everything. You make my life more beautiful every day.

Cristian Verdugo
Terrassa, Barcelona, Spain
April 2021

Abstract

Photovoltaic energy systems require power electronics interfaces to convert the energy generated and transfer it to the electrical grid. Depending on the power level, grid connected PV systems can be grouped into four types of configurations: centralized, string, multistring and ac-module, which can be used based on the application and power rating of the PV installation. Most of large scale applications are based on centralized configurations with inverters of two or three voltage levels connected to hundreds of PV arrays. However, with the development of high power multilevel converters, new possibilities have come out to implement multilevel converters in PV systems with higher efficiency and power quality.

One of the main challenges of using multilevel converter in PV applications are the appearance of leakage currents and high floating voltages in the PV panels. To solve this issue, high or low frequency transformers are required to provide galvanic isolation. The Cascaded H-Bridge converter with high frequency transformers in the dc side has been widely studied as a promising solution for large scale applications. However, the implementation of high frequency transformers require a second conversion stage. In an effort to integrate ac transformers to reduce the number of conversion stages by using medium or low frequency components, cascaded transformer multilevel inverters (CTMI) have been proposed. Such configurations are connected in series through the secondary windings of the transformers, satisfying required isolation requirements and providing winding connection options for symmetrical and asymmetrical configurations. Based on such approach, this PhD dissertation presents the Isolated Multi-Modular Converter, characterized by a cascaded configuration of two arms connected in parallel. The objective of the proposed configuration is to enable the integration of a multilevel converter with galvanic isolation and the capability of operating at different power levels.

First, an introduction of multilevel converters with dc and ac galvanic isolation is reviewed. This approach defines the basis of the converter proposed. Then, a mathematical analysis of the IMMC for a single and three phase configuration is presented. This study demonstrates that the IMMC can be represented based on two electrical circuits whose purpose is to emulate the dynamic response of the output and circulating currents based on the current arms. Furthermore, the relationship between the power flow and the current arms is also revealed to define later the current references in the control loops.

As the IMMC requires a dedicated control strategy to regulate the energy and the current signals, a central control architecture is addressed. This approach is essential for regulating the total energy per arm, giving rise to a proper converter operation. In order to provide a stable response in dynamic and steady state, the well-known crossover frequency and phase margin technique is used to determine the control parameters in the inner and outer control loops.

As PV panels can operate at different conditions, they are prone to generate different power levels. Therefore, all power modules connected in series must provide a high flexibility to allow possible power imbalance scenarios. In this regard, two control strategies embedded in each module are evaluated. Through the amplitude and quadrature voltage compensation techniques, the converter demonstrates its functionality under power imbalances, while fulfilling the required control objectives. Moreover, by combining both control strategies, it is possible to extend the operating range, enabling higher levels of power imbalances.

The work presented in this PhD dissertation is supported by simulation results. Additionally, a complete experimental setup was built to endorse the conclusions. Simulation and experimental results include balance and imbalance power scenarios, demonstrating a flexible multilevel converter for PV applications.

Contents

Acknowledgements ..... **i**
Abstract ..... **iii**
Contents ..... **v**
List of Figures ..... **ix**
List of Tables ..... **xv**
Nomenclature ..... **xvii**
1 Introduction **1**
1.1 Background 1
1.1.1 Utility scale photovoltaic power plants 4
1.1.2 Multilevel converters in photovoltaic applications 6
1.2 Problem definition 14
1.3 Objectives of the PhD Dissertation 15
1.4 Outline of the PhD Dissertation 16
1.5 List of publications and contributions 17
1.5.1 Journal Papers: 18
1.5.2 Conference papers: 18
1.5.3 Patents: 19
2 Isolated Multi-Modular Converter **21**
2.1 Single-phase configuration 21
2.1.1 Fundamental principle 23
2.1.2 Output and circulating current model 26
2.1.3 Average dc voltage model 29
2.2 Three-phase IMMC 32
2.2.1 Stationary and synchronous reference frame 33

2.2.2 Three-phase current model 35
2.2.3 Three-phase average dc voltage model....42
2.3 Summary of the chapter 44
3 Control of the IMMC 47
3.1 Control architecture....47
3.2 Output and circulating current controllers 48
3.2.1 Tuning of control parameters....51
3.2.2 Design of output current control....51
3.2.3 Design of circulating current control 56
3.2.4 Output and circulating current control architecture 57
3.3 Third harmonic compensation....60
3.4 Average DC voltage controllers....60
3.5 Synchronization control loop 64
3.6 General control architecture....65
3.7 Simulation results....68
3.7.1 Study case I: Irradiation step in upper and lower arms....72
3.7.2 Study case II: DC voltage step in lower arm 75
3.8 Summary of the chapter 78
4 Amplitude and Quadrature Voltage Compensation 79
4.1 Concept description....79
4.2 Amplitude voltage compensation....81
4.2.1 Control description 82
4.2.2 Effect of amplitude voltage compensation on imbalance operation....85
4.2.3 Experimental results 90
4.3 Quadrature voltage compensation....93
4.3.1 Dependency between circulating current and modulation index 95
4.3.2 Effect of quadrature voltage compensation on imbalance operation....99
4.3.3 Experimental results 105
4.4 Combination of both control strategies 108
4.4.1 Experimental results 111
4.5 Summary of the chapter 114
5 Conclusions and future work 117
5.1 Conclusions....117

5.2 Future works 120
References 123
References 123
6 Laboratory Setup 133
6.1 Laboratory description 133

List of Figures

Fig. 1.1 Photovoltaic power capacity installed per continent and its projection for the next 30 years [2] 3
Fig. 1.2 Photovoltaic power capacity and power deployment per GW installed and its projection for the next 30 years [2] 3
Fig. 1.3 PV power plant configurations. (a) Central, (b) String, (c) Multistring configuration 5
Fig. 1.4 (a) 2 Level voltage source converter used in central inverters, (b) Neutral point clamped, (c) T-Type converter 8
Fig. 1.5 Cascaded configuration with dc-dc stage. (a) Cascaded H-Bridge converter, (b) Multi-Modular cascaded dc-dc converter 9
Fig. 1.6 Dc power module for dc-dc stage with high frequency isolation. (a) Flyback, (b) Full bridge configuration 10
Fig. 1.7 Single phase cascaded transformer multilevel inverter. (a) Classical configuration, (b) reduced number of switches. 12
Fig. 1.8 Three-phase cascaded transformer multilevel inverter. (a) Independent dc sources [66], (b) common dc source 12
Fig. 1.9 Three-phase cascaded transformer multilevel inverter [67]. 13
Fig. 2.1. Isolated Multi-Modular Converter (IMMC) 22
Fig. 2.2. H-Bridge module of the isolated multi-modular converter 23
Fig. 2.3. Electric model of the single-phase IMMC 26
Fig. 2.4. Average current model of the IMMC 28
Fig. 2.5 Power exchange representation of *N* modules in series-connection 30

Fig. 2.6 Three-phase Isolated Multi-Modular Converter 35
Fig. 2.7 Electric model of the three-phase IMMC.....36
Fig. 2.8 Thee-Phase output current model.....41
Fig. 2.9 Three-Phase circulating current model 41
Fig. 3.1 General control structure of the IMMC 48
Fig. 3.2 Control structure of the output and circulating current controller.....49
Fig. 3.3 Control structure of the output and circulating current controller considering a time delay G_d 50
Fig. 3.4 Simplified output current model 52
Fig. 3.5 Step response of complementary sensitivity function in output current controller 54
Fig. 3.6 Step response of load disturbance sensitivity function in output current controller 55
Fig. 3.7 Bode diagram of open loop in output current controller.....55
Fig. 3.8 Simplified circulating current model 56
Fig. 3.9 Bode diagram of open loop in circulating current controller 57
Fig. 3.10 Output current control based on PI controllers 58
Fig. 3.11 Circulating current control based on PI controllers.....58
Fig. 3.12 PI control with anti-windup 59
Fig. 3.13 Average dc voltage control loop 62
Fig. 3.14 Bode diagram of open loop in average dc voltage controller.....62
Fig. 3.15 Step response of complementary sensitivity function in the average dc voltage controller.....63
Fig. 3.16 Step response of load disturbance sensitivity function in the average dc voltage controller.....63
Fig. 3.17 Synchronous-Reference-Frame PLL.....65
Fig. 3.18 Central control architecture of the IMMC.....66
Fig. 3.19 Simulation setup of the three-phase IMMC 68
Fig. 3.20 Control configuration used in simulation results 69
Fig. 3.21 Active power response under different temperature and irradiation conditions. 71
Fig. 3.22 Simulation results of total power delivered into the grid, average power produced by the upper and lower arms, irradiation steps in the equivalent PV modules. ..72

Fig. 3.23 DC voltage response in modules of the upper and lower arm under irradiation steps 73
Fig. 3.24 Dynamic and steady state response of current arms, circulating current and output current under irradiation steps. 74
Fig. 3.25 Simulation results of total power and average power produced by the upper and lower arms under irradiation and dc voltage changes. 76
Fig. 3.26 DC voltage response in modules of the upper and lower arms under irradiation and dc voltage changes. 76
Fig. 3.27 Dynamic and steady state response of current arms, circulating current, output current and modulation indexes under irradiation and dc voltage changes. 77
Fig. 4.1 Amplitude voltage compensation strategy for modules in upper and lower arm . 84
Fig. 4.2 Control architecture based on the amplitude voltage compensation 85
Fig. 4.3 Simulation results of dc voltages and active power in modules of the upper and lower arms using the amplitude voltage compensation 86
Fig. 4.4 Simulation results of current arms, circulating current and output current using the amplitude voltage compensation. (a) Irradiation step in module M_{u2}, (b) Irradiation step in module M_{l3} 87
Fig. 4.5 Simulation results of modulation indexes in modules of the upper and lower arms under irradiation steps. (a) Event 1, (b) Event 2, (c) Event 3 89
Fig. 4.6 Experimental results of dc voltage steps in modules of upper and lower arms using the amplitude voltage compensation 90
Fig. 4.7 Experimental results of first event. Current arm, and circulating current using the amplitude voltage compensation 91
Fig. 4.8 Experimental results of second event. Current arm and circulating current using the amplitude voltage compensation 92
Fig. 4.9 Experimental result of active power using the amplitude voltage compensation . 92
Fig. 4.10 Representation of output voltage based on the series connection of three consecutive modules 95
Fig. 4.11 Active power response in balance operation under circulating current and phase angle variations. (a) Power in module of upper arm, (b) Power in module of lower arm . 96

Fig. 4.12 Active power response in imbalance operation under circulating current and phase angle variations. (a) Power in module of upper arm, (b) Power in module of lower arm 97
Fig. 4.13 Quadrature voltage compensation strategy for modules in upper and lower arms 99
Fig. 4.14 Simulation results of dc voltages and active power in modules of the upper and lower arms using the quadrature voltage compensation.....100
Fig. 4.15 Simulation results of first irradiation step using the quadrature voltage compensation. Current arms, circulating current and output current 101
Fig. 4.16 Simulation results of third irradiation step using the quadrature voltage compensation. Current arms, circulating current and output current 102
Fig. 4.17 Simulation results of modulation indexes in modules of upper and lower arms under irradiation steps. (a) Event 1, (b) Event 2, (c) Event 3 103
Fig. 4.18 Maximum power imbalance affordable under different circulating current levels 104
Fig. 4.19 Experimental results of dc voltage steps in modules of upper and lower arms using the quadrature voltage compensation 105
Fig. 4.20 Experimental results of first event. Current arm and circulating current using the quadrature voltage compensation.....106
Fig. 4.21 Experimental results of second event. Current arm and circulating current using the quadrature voltage compensation 107
Fig. 4.22 Experimental result of active power using the quadrature voltage compensation 108
Fig. 4.23 Combination of amplitude and quadrature voltage compensation in one module 109
Fig. 4.24 Power response using the amplitude and quadrature voltage compensation. (a) Analysis based on $\Delta m_{id,k} = 0$, (b) Analysis based on $\Delta m_{id,k} = -0.1$, (c) Analysis based on $\Delta m_{id,k} = -0.15$ 111
Fig. 4.25 Experimental results of dc voltage steps in modules M_{u1} and M_{l2} using the amplitude and quadrature voltage compensation 112
Fig. 4.26 Experimental results of first event based on the amplitude and quadrature voltage compensation. Current arm and circulating current 113

Fig. 4.27 Experimental results of second event based on the amplitude and quadrature voltage compensation. Circulating and output current 114
Fig. 4.28 Experimental result of active power using the amplitude and quadrature voltage compensation..... 114
Fig. 6.1 Block diagram of testbench laboratory setup 134
Fig. 6.2 Laboratory setup..... 134
Fig. 6.3 Electrical representation of the programmable dc source connected to each module. Power behavior based on dc voltage regulation 135
Fig. 6.4 AC transformers and central control platform..... 137
Fig. 6.5 Electric diagram of two transformers connected in series..... 137
Fig. 6.6 Module configuration..... 138
Fig. 6.7 Electrical representation of one module 138
Fig. 6.8 Configuration of control platform. 139

List of Tables

Table 1.1 Comparative between central, string and multistring configurations 6
Table 1.2 Summarize of multicell converters with dc and ac galvanic isolation..... 14
Table 3.1. Parameters of simulation setup..... 53
Table 3.2 Control parameters of output current controller 55
Table 3.3 Control parameters of circulating current controller 57
Table 3.4 Control parameters of average dc voltage controller..... 64
Table 3.5. Parameters of simulation setup..... 70
Table 6.1 Parameters of experimental setup..... 136

Nomenclature

Acronyms	Abbreviations
ac	Alternating current
adc	Analog digital converter
CAN	Controller Area Network
CHB	Cascaded H-Bridge
CTMI	Cascaded Transformer Multilevel Inverter
dc	Direct current
DSP	Digital Signal Processor
HVDC	High Voltage Direct Current
IMMC	Isolated Multi-Modular Converter
MMC	Modular Multilevel Converter
NPC	Neutral Point Clamped
PCC	Point of Common Coupling
PI	Proportional Integrator
PLL	Phase-Locked Loop
PR	Proportional Resonant
PV	Photovoltaic
PWM	Pulse Width Modulation
QSG	Quadrature Signal Generator
RES	Renewable Energy Sources

SCR	Short Circuit Ratio
SOGI	Second Order Generalized Integrator
SRF	Synchronous Reference Frame
STATCOM	Static Synchronous Compensator
VCO	Voltage Controlled Oscillator
VSC	Voltage Source Converter

Chapter 1.

Introduction

This chapter introduces the background of this PhD dissertation, including the state of the art and objectives. A review of photovoltaic power plants and their challenges are first revealed. Then, the power electronics technologies used and proposed in the literature for utility scales are summarized. This stablishes a framework for this thesis, which is addressed in the objectives. Finally, a brief description of each chapter is presented.

1.1 Background

The new era of power generation is strongly driven by the awareness of environment problems and the importance of caring our planet. Social and economic progress have provided tools to develop clean energy sources highly reliable and efficient, capable to supply energy from small to large power levels. These energy sources also known as renewable energies can be classified as bioenergy, hydropower, geothermal, solar and wind energy. According to [1], the year 2019 a total of 2.537 gigawatts (GW) of renewable power capacity was installed, being the solar and wind energy the top of these energy sources. The annual global market for solar PV exceed the 580.15 GW at the end of 2019 [2], while the wind market exceed the 622.70 GW [3].

The significant deployment of renewable energies around the world is triggered in part by the rapid declines in the generation costs. In fact, it is expected that the increasing economies of scale and further technological improvements will continue to reduce the cost of photovoltaic energies. According to [2], the levelized cost of electricity (LCOE) in

photovoltaic energy drastically fell in 77% from 2010 to 2018 that means 0.37 USD per kWh to 0.085 USD per kWh, and the projection of the average falling energy by 2030 is expected to be 0.02 USD per kWh and 0.05 USD per kWh by 2050.

This accelerated deployment of renewable energies would reduce in 90% the carbon dioxide emission (CO_2) by 2050, in which photovoltaic energy would lead significant reductions, representing 21% of the total emission mitigation [2]. This will come with the fast growing of photovoltaic energy expected for the next 30 years. By 2050 photovoltaic energy would represent the second largest power generation source, just behind wind energy, generating a quarter of total electricity needs with a capacity power of 2840 GW by 2030 and 8519 GW by 2050. That means six times and eighteen times the power capacity installed in 2018.

In Fig. 1.1 and Fig. 1.2 is illustrated the power capacity installed worldwide between 2010-2018 and its projection for the next 30 years. The global capacity installed in 2010 was 40 GW with an annual deployment of 17 GW. Similarly, in 2018 the global capacity installed was 480 GW with an annual deployment of 94 GW. Leaving Asia as the continent with the largest PV production, followed by Europe in the second position and North America in the third position. By 2030, it is expected that the global market will continue to be driven by Asia with a global capacity of 1860 GW, but North America will take the second position with a power capacity of 437 GW. By 2050 the power installed will continue to grow, with Asia representing more than half of the addition capacity with 4.837 GW. The second largest photovoltaic market will be led by North America with 1.728 GW, followed by Europe with 891 GW. This huge different between each continent is mainly given by the investment levels. According to [2], it is expected that Asia invests 113 USD billion per year from now until 2050, followed by North America with an investment of 37 USD billion per year and Europe with 19 USD billion per year.

Due to the policies and financial support provided by several countries, most of this power increase comes from grid connection systems, mainly utility scale PV plants. The size and the number of large PV plant projects during 2018 rounded about 235 with power levels above 50 MW, which are distributed in at least 37 countries [3]. Considering the significant market potential and cost competitiveness, it is expected that utility-scale projects will still predominate by 2050. Nonetheless, distributed generations such as rooftop technologies, electric vehicles (EV) and building integrated PV(BIPV) systems would have a huge impact on power generation levels.

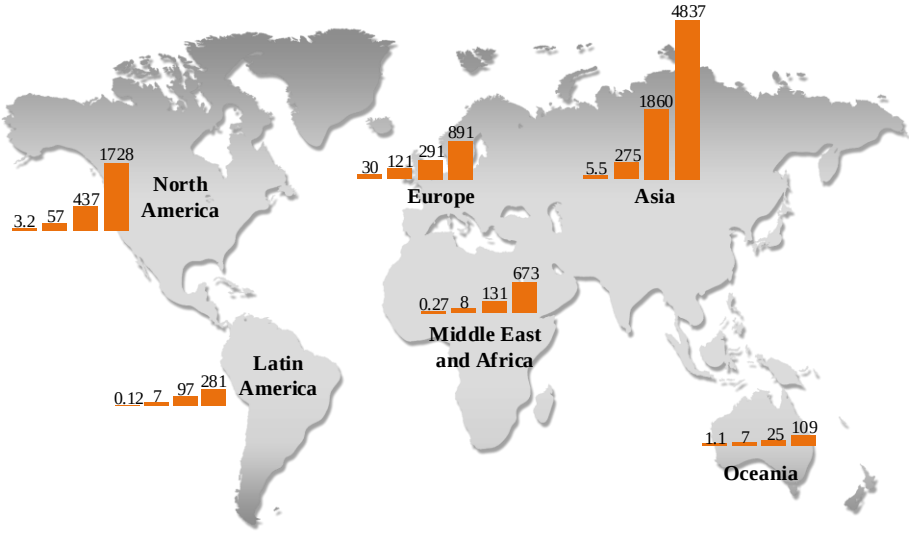

Fig. 1.1 Photovoltaic power capacity installed per continent and its projection for the next 30 years [2]

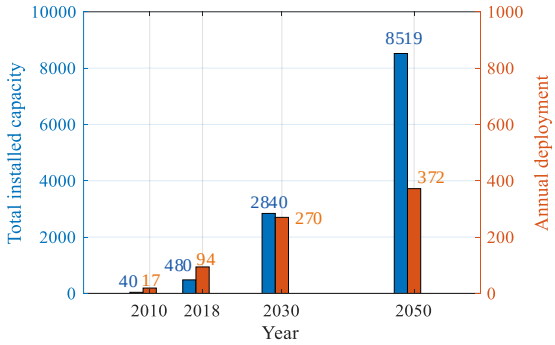

Fig. 1.2 Photovoltaic power capacity and power deployment per GW installed and its projection for the next 30 years [2]

The industry would need to be prepared for such a significant power increase over the next 30 years. Therefore, better technological solutions and more innovations are expected to integrate the rising shares of photovoltaic power generation. These new innovations are focused on providing new markets to use this energy source, designing more efficient technologies in PV panels, providing more flexible power systems to integrate variable renewable energy sources and developing new configurations of power converters to manage large amount of power levels. Having in mind the requirements of new

configurations of power converter to deal with the future power generation levels, this thesis study a multilevel configuration to be used in PV applications.

1.1.1 Utility scale photovoltaic power plants

Grid connection of PV power plants are based on three different configurations: central, multistring and string topologies. The choice of one over another will depend on several aspects such as: power level, location, cost and reliability which are summarized in [4]–[11]. In this section, a review of each of them is described, including their main features and advantages.

1.1.1.1 Utility scale configurations

a. Central

Central configuration illustrated in Fig. 1.3.a is the most common configuration used for large PV applications. This topology interconnects several PV panels to one inverter. The disposition of the panels is grouped into hundreds of arrays which have hundreds of PV strings connected in parallel. Similarly, these strings have several PV panels connected in series to reach the proper voltage level in the dc side. In the case of large power plants, several central inverters are connected to medium voltage collectors through low to medium voltage transformers (LV-MV), and then a medium - high voltage (MV-HV) transformer is used to connect the power plant to the transmission line [10].

b. String

String configuration illustrated in Fig. 1.3.b connects one PV string to one individual inverter. This modularity provides independent MPPTs, increasing the efficiency of power generation over the central configuration when partial shading happens.

To eliminate leakage currents and avoid voltage levels beyond the maximum level allowed in the PV panels, power converters with galvanic isolation and two conversion stages may be implemented. Typically, dc-dc with high frequency transformers or dc-ac converters with low frequency transformers can be used [12]–[15].

c. Multistring

Multistring configuration shown in Fig. 1.3.c combines the architecture of string and central configurations described before. It contains string of PV panels connected to individual dc-dc converters, which are connected to a common central inverter [16]. In this sense, independent MPPTs are also possible, increasing the maximum power generated over

the central configuration. Additionally, dc-dc converters can boost the dc voltage, creating a medium voltage collector between the dc-dc converters and the inverter.

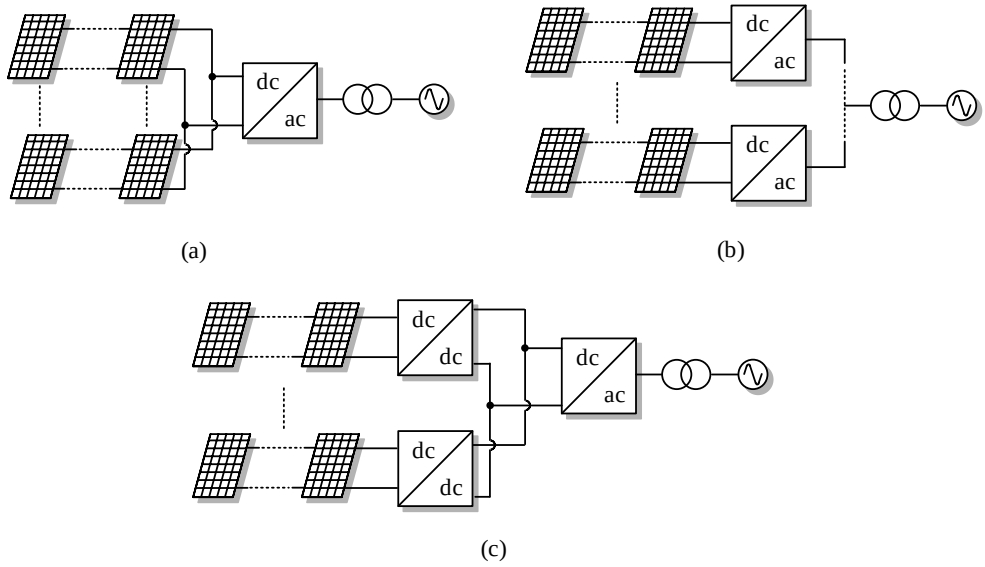

Fig. 1.3 PV power plant configurations. (a) Central, (b) String, (c) Multistring configuration

A comparative analysis of all configurations is described in the following section.

1.1.1.2 Comparative analysis between central, string and multistring configurations

Based on the analysis introduced in [4], the three different configurations are evaluated according to: robustness, reliability, flexibility, power losses and cost. In Table 1.1 is illustrated the impact of each category, where it can be seen how the central configuration has the highest robustness compared to the string and multistring configurations. This is because one central inverter manages the power of hundreds of PV arrays at the same time. However, this structure reduces considerably the flexibility, in contrast to string topology, which connects individual PV string to each inverter, making it the configuration with the highest flexibility and reliability.

According to the power losses category, power mismatches trigger to large impacts on central configurations. These losses are inevitable in any PV array and they depend on uneven degradation, shading and MPPT efficiency. The dc losses are also high in central inverters since many strings are connected in parallel to the same dc bus. However, this configuration has small ac losses, as LV-MV transformers are connected to create a

common collector inside the PV plant. In the case of string and multistring topologies, the dc losses are less than central configurations because they can step up the dc voltages if a dc-dc stage with galvanic isolation is used. Nevertheless, more electronics components are required to achieve this purpose.

The last category considers maintenance and installation cost. The comparison shows that central configuration is by far the cheapest technology in contrast to string and multistring. This characteristic makes central topology very appealing for large PV projects.

Summarizing, central configuration has the following characteristics: high robustness, low flexibility, high losses due to power mismatches and dc cables, low losses in the ac side and low maintenance and installation costs. On the other hand, string and multistring are highly flexible and reliable, low dc side losses and high maintenance and installation cost when power levels increase.

Table 1.1 Comparative between central, string and multistring configurations

		Central	String	Multistring
Robustness				
Flexibility				
Reliability				
Power losses	Switching			
	Mismatching			
	dc side			
	ac side			
Cost	Maintenance			
	Installation			

1.1.2 Multilevel converters in photovoltaic applications

Multilevel converters come up to overcome the limitation faced in the traditional 2L-VSC converter. The ability to provide more than 2 levels in the ac side brings several favorable advantages in many industrial applications such as those described in [12], [15].

In the classical two-level converter illustrated in Fig. 1.4.a, the output voltage is always switched between the maximum and the minimum dc voltage level, giving rise to high dv/dt and high electromagnetic interference (EMI), especially with high switching frequency operation. Besides that, low frequency harmonic components in the ac current caused by

the voltage waveform in the converter terminals requires high ac filters to reduce harmonics, increasing cost and size of the converter.

Another limitation of two-level converters is the voltage rating of semiconductor devices available in the market [17]–[20]. Because most of high-power applications operate at medium or high voltage levels [13], [21], the voltage ratings of semiconductor devices have to be large enough to withstand high dc voltage levels. Therefore, semiconductor components are series-connected in order to reach the desired voltage level. As a result, the reliability of the converter is affected due to the increase in the number switches connected.

Unlike two-level converters, multilevel converters split the dc voltage in several modules, and as the blocking capability of the switching device is determined by the dc capacitor rather than the full dc link voltage, the voltage stress in each semiconductor is considerably reduced. Additionally, the capability of providing an output voltage with multiple stepped levels aids to improve the quality waveform, thus reducing harmonic components.

Some of multilevel converters used in the industry have been implemented in many applications such as: motor drives, fans, traction and high power transmission systems [12], [14]. These multilevel converters can be classified into two main families: single dc source converters and multicell topologies. The early multilevel converters are those based on single dc sources and are described as configurations with a single dc-link capacitor or a series connection of capacitors connected to the pole-to-pole dc side. The most common topologies belonging to this family are the neutral point clamped [22]–[25] and the T-Type converter [26]–[28] illustrated in Fig. 1.4.b and Fig. 1.3.c, which generate three output voltage levels. They can be typically found in central configurations of PV power plants. Additionally, other configurations can be found in the literature [29]–[32]. The number of voltage levels is generally limited by the number of dc-link capacitors connected and they cannot be easily extended to high levels. Hence, their application is mainly oriented to low and medium voltage range.

Compared to the single dc source family, multicell converters are able to operate at higher voltage levels. The series connection of converters also referred as modules reduces the complexity of increasing the stepped voltage levels, since modules are connected to independent dc supplies which can be easily added or removed. Among the most popular multicell converters we can find: the cascade multilevel converter based on H-bridge modules (CHB) [33]–[37], the modular multilevel converter (MMC) [38]–[40] used for HVDC systems and the matrix converter [41]–[43]. However, the use of multilevel

converter for PV applications is limited due to insulation constraints in PV panels [44], which is defined by the maximum voltage level allowed in their terminals. In order to solve this problem, converters with galvanic isolation in the dc or ac side are used. In the next subsection we introduce some of the multicell configurations found in PV applications.

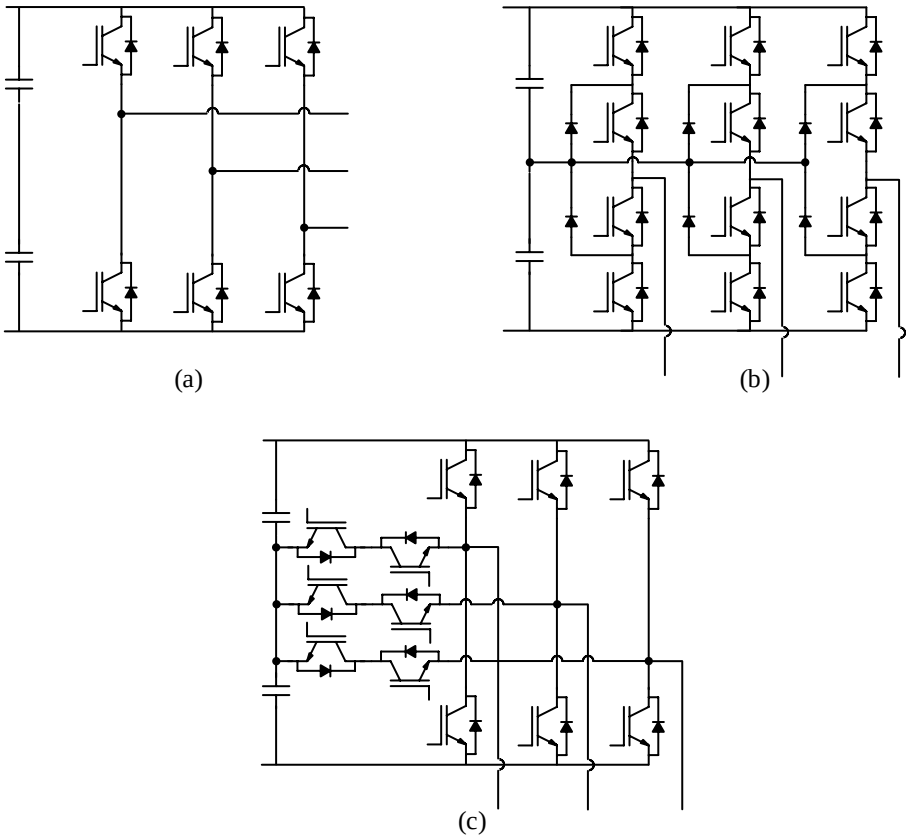

Fig. 1.4 (a) 2 Level voltage source converter used in central inverters, (b) Neutral point clamped, (c) T-Type converter

1.1.2.1 Multicell converters with dc isolation

One of the most common multicell converters introduced for PV applications is the cascaded H-bridge converter (CHB) illustrated in Fig. 1.5. This configuration appeared first in 1988 [45], but it was during the 90's when gained more attention [46]. Nowadays, the main application of this topology is in medium voltage, high-power drives and PV systems. The CHB is formed by the series connection of H-bridge cells, where each of them is connected to independent dc sources. In the case of PV application, a dc-dc stage with high

frequency isolation is used to avoid high floating voltages [47]. A generalized three phase CHB multilevel converter with equal dc voltage distribution and k modules generate $2k+1$ output voltage levels. One of the strong points of this topology is its modularity, which permits the connection of unlimited modules, increasing the power level and power quality.

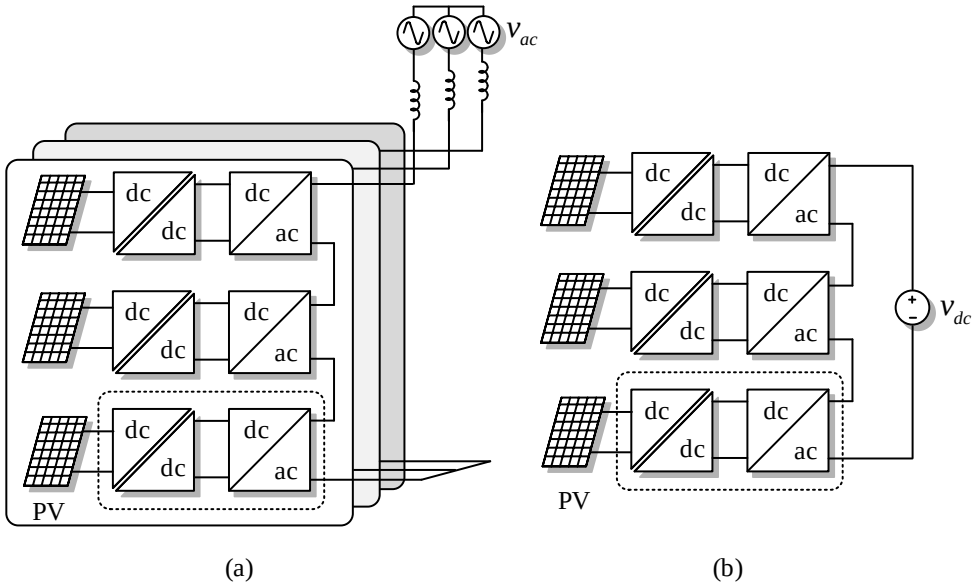

Fig. 1.5 Cascaded configuration with dc-dc stage. (a) Cascaded H-Bridge converter, (b) Multi-Modular cascaded dc-dc converter

CHB can be used with equal and unequal dc sources. In equal dc sources all modules generate the same voltage. For instance, four modules in series connection will generate up to 9 voltage levels. On the other hand, CHB based on unequal dc sources also known as hybrid or asymmetric CHB inverter [48]–[50] operates at different dc voltage levels. The use of asymmetric input voltages reduces the redundancy of voltage levels, maximizing the number of different levels generated by the inverter. Therefore, this topology can achieve the same output voltage quality but with less number of modules. In the case of four modules in series connection, the converter is able to generate up to 81 voltage levels. However, the main drawback is the fact that different power rating of modules are required, which force to special designs.

A second multicell topology proposed for large scale PV applications is the Multi-Modular Cascaded dc-dc (MMC dc-dc) converter presented in [51] and illustrated in Fig. 1.5.b. This converter is composed by several modules with two dc-dc converter stages. The

first stage isolates the PV string, eliminating leakage currents and high floating voltages. The second stage is connected in series to the other modules, increasing the dc voltage level. Compared to the Modular Multilevel Converter (MMC), the MMC dc-dc converter does not require line inductances [51]. Additionally, multiple legs can be used for multiterminal HVDC systems, in which several converters are connected to the same dc transmission line.

In CBH and MMC dc-dc configurations, the high frequency galvanic isolation provided by the first stage can be implemented with different configurations of dc-dc converters. In Fig. 1.6 is illustrated two common dc-dc converters widely used in the industry, which are connected to an H-bridge module. The Flyback illustrated in Fig. 1.6.a is a configuration based on the buck-boost converter [52]–[54]. It is composed of an isolated transformer, a switch in series to the primary side of the transformer, a diode and an output filter. The second dc-dc converter shown in Fig. 1.6.b is based on a full bridge configuration, which has a diode rectifier connected to the secondary side of the transformer to generate the dc voltage level.

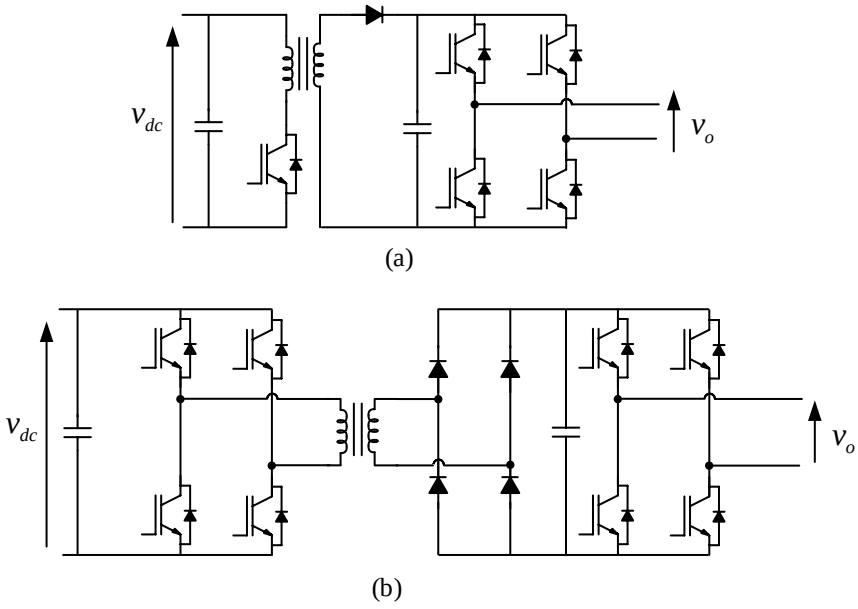

Fig. 1.6 Dc power module for dc-dc stage with high frequency isolation. (a) Flyback, (b) Full bridge configuration

Multiple flybacks and full bridge modules can be used in parallel to generate an interleaved circuit, which enable the current distribution among all converters, allowing an increase in the apparent switching frequency and thus a reduction of the HF transformer.

1.1.2.2 Multicell converters with ac isolation

A second family of multicell converters with galvanic isolation used in PV applications are based on low frequency transformers. These group of converters called cascaded transformer multilevel inverters (CTMI) connect several modules in series through the secondary side of the transformer, while the primary side is connected to the converter terminals [55]. In this sense, a stepped voltage level is achieved, while providing isolation to each module. In Fig. 1.7.a is illustrated the classical single-phase configuration of a CTMI [56]. This configuration was first proposed for a single dc source, where several H-bridge converters are connected in parallel. Note that, the connection to a single dc source eliminates energy imbalances due to power mismatches in PV panels [35], [57], [58].

The amplitude of the output voltage in the secondary side of the transformer is defined by the dc voltage and the turn ratio of the transformer. The possibility of using equal or unequal number of turn ratios results in two different CTMI classifications: symmetrical and asymmetrical configurations. Traditional CTMIs use equal number of turn ratios, giving rise to an output voltage with $2k+1$ number of levels [59]. For instance, a CTMI based on three modules generates up to 9 voltage levels. On the other hand, asymmetrical configurations can considerably increase the number of voltage levels. In [60] a study of an asymmetrical CTMI has presented that by using binary geometric progression in the turn ratio, it is possible to reach up to $2^{k+1}-1$ voltage levels. Similarly, using ternary geometric progression, the number of levels obtained is 3^N. For instance, considering a converter with three modules, an asymmetric binary ratio 1:2:4 generates up to 15 levels and in the case of a ternary ratio of 1:3:9, we obtain up to 27 levels. However, this asymmetric ratio trigger to an unbalanced power distribution [61], demanding special designs.

Other configurations of CTMI with reduced number of switches have been proposed based on single dc sources [55], [62]–[65]. They take benefit from the transformer isolation and connect several H-bridge and half bridge modules in parallel. In this sense, a similar number of voltage levels can be achieved but with less number of switches. An example of CTMI with reduced number of switches is illustrated in Fig. 1.7.b. The converter consists of four legs with two of them connected to each transformer and adjacent to each other. Additionally, one transformer terminal is connected to the midpoint of the dc link. Using this configuration, it is possible to achieve up to nine voltage levels [55].

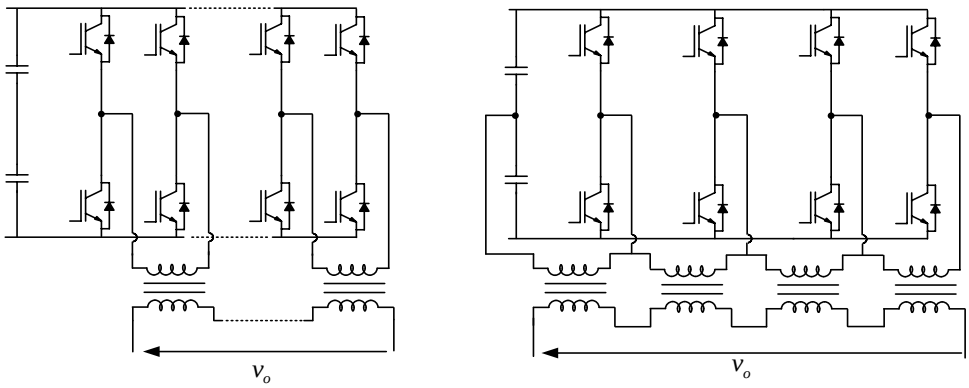

Fig. 1.7 Single phase cascaded transformer multilevel inverter. (a) Classical configuration, (b) reduced number of switches.

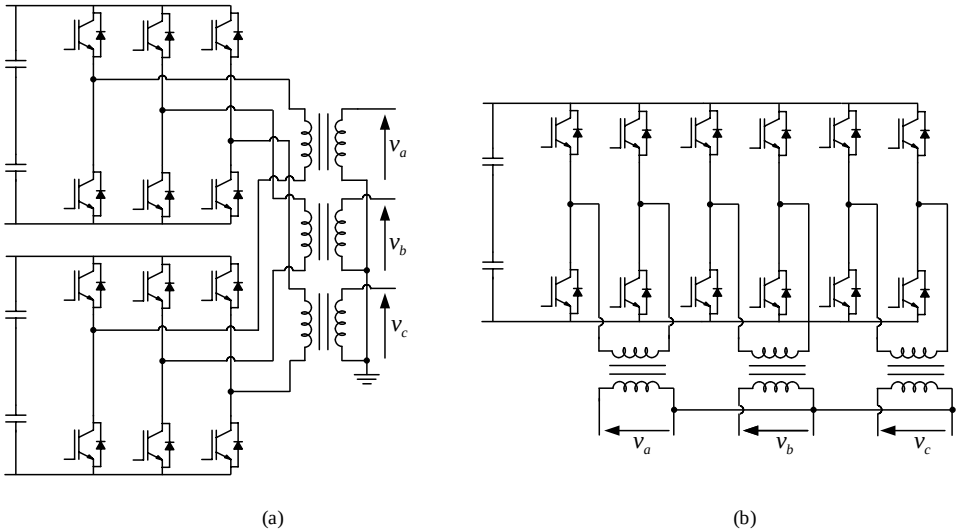

Fig. 1.8 Three-phase cascaded transformer multilevel inverter. (a) Independent dc sources [66], (b) common dc source

Similarly, three-phase CTMI configurations have also been proposed. As in single-phase CTMIs, they connect the converter terminals to a low frequency transformer, while the secondary windings are connected in series, providing isolation between the dc and ac side. In [66] a CTMI based on two level inverters has been introduced for STATCOM applications. The configuration illustrated in Fig. 1.8.a connects the inverters to the low-voltage side of two transformers and the high-voltage side to the grid. The dc-link is

independent of each inverter and are maintained constant, while the modulation index is controlled to achieve the required objective.

Using the classical CTMI, a three-phase configuration connected to a single dc-source is also possible. In Fig. 1.8.b is illustrated the basic three-phase CTMI with one H-bridge module per arm and in the case of using multiple modules, it is possible to use the configuration shown in Fig. 1.9 and proposed in [67].

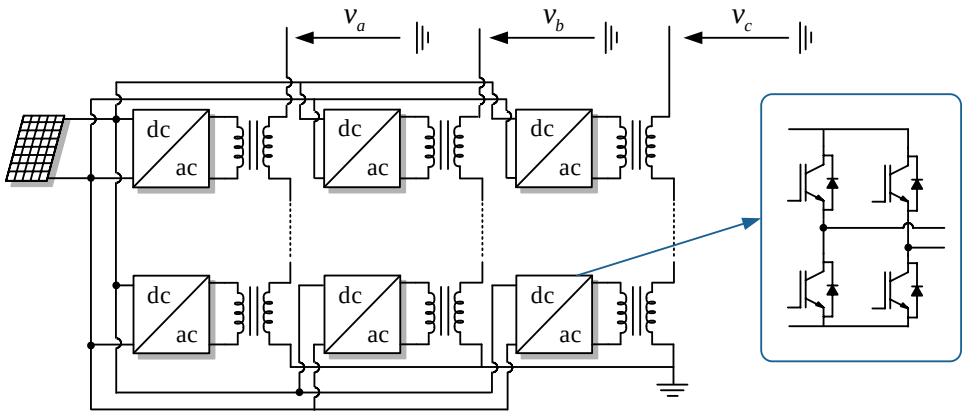

Fig. 1.9 Three-phase cascaded transformer multilevel inverter [67].

1.1.2.3 Summarize of multicell converter with galvanic isolation

In previous sections we introduced some of the classical multicell configurations that can be used for PV applications. They are divided in two groups: multicell converters with dc isolation and multicell converters with ac isolation. While dc isolation requires a dc-dc converters with high frequency transformers, multicell converters with ac isolation use medium or low frequency transformers connected to the ac terminals. Additionally, some multicell converters can be connected to a single dc source, eliminating voltage differences due to imbalances in the primary source, or they can be connected to multiple dc sources. Therefore, dedicated MPPTs are possible, but also more complex control strategies are required to operate under power imbalances.

Table 1.2 summarizes some of the configurations found in the literature.

Table 1.2 Summarize of multicell converters with dc and ac galvanic isolation

Multicell converters	Configuration	Publications
Dc isolation		
	Cascaded H-Bridge converter	[35], [37], [68]–[71]
	Modular Multilevel converter with dc isolation	[72], [73], [82]–[85], [74]–[81]
	Multi-Modular Cascaded dc-dc converter	[51], [86]–[88]
Ac isolation (CTMI)		
	Classica CTMI (single and three phase, symmetric and asymmetric configuration)	[56], [59], [94], [95], [60], [66], [67], [89]–[93]
	Reduced number of switches	[55], [62]–[65], [95]–[98]
	Four wire connection	[99]

1.2 Problem definition

Because power demands have increased considerably fast. Higher levels of power generation are required every day. Large amount of this new power generation comes from renewable energies such as wind and solar which are under continues improvements. In the case of photovoltaic energy sources, it has reported a high level of penetration due to improvements in its technology, cost reduction and high reliability. Therefore, it is expected that the levels of the power installed continue growing. However, these new demands bring several challenges and needs that must be covered. For instance, improvements in the PV panels to increase the efficiency and generate more power per m2, provide auxiliary services in frequency and voltage support, emulate inertia to deal with the lack of synchronous generators, ensure a constant power generation to supply the required levels at any time and develop new configuration of power converters capable to deal with large levels of power generation.

Few years ago, we used to discuss about large PV power plants which were able to generate hundreds of MW. Today we talk about very large PV power plants with hundreds of GW of power installed [100]. In many cases, this huge amount of power is provided by

a single power plant with hundreds or thousands of power converters installed and distributed in the field. As described in previous section, centralize, string and multistring are the configurations used based on their robustness, flexibility, reliability, power losses and costs. However, the choice of the converter technology is still under discussion.

It is a fact that multicell converters are one of the best options to be used in PV power plants, as they provide high quality power, reduced harmonic components and independent MPPT to extract the maximum power available. Nevertheless, considering some limitations such as: isolation requirements and reliability, it is necessary to continue looking for new configurations to find the suitable converter topology capable of satisfying the future trend of PV systems.

1.3 Objectives of the PhD Dissertation

This thesis presents the work carried out during the PhD program aimed towards the designing of a multilevel converter for photovoltaic energy systems. The definition of the PhD project considered the high penetration of renewable energies and the requirements of new power electronics configurations capable to deal with medium or high power and voltage levels. The objectives also include the study of multilevel configurations used for such application.

The proposed configuration would provide access to deal with medium voltage level, by integrating a series connection of power converters connected to PV panels. The objectives stated to guide this PhD thesis are summarized as follows:

1. Propose a multilevel converter for photovoltaic power plants, capable of connecting several converters in series to take advantage of multilevel configurations. Additionally, the configuration proposed must provide galvanic isolation to avoid leakage currents and high floating voltage levels in the PV panels.
2. Implement a control architecture and evaluate it for the proposed converter configuration, including the correct power sharing in normal and imbalance operation.
3. Because multilevel converter are prone to imbalance power levels, the control strategy propose has to be able to withstand large power imbalances, including critical scenarios.

The results in this PhD dissertation aim to report the investigation of the three-phase multilevel converter proposed and the control strategies required to achieve its optimal operation. These objectives are carry out based on the following aspects.

- Model and design of the Isolated multilevel converter

Due to the fact that power converters with galvanic isolation are required in photovoltaic applications. Based on the concept presented in [60], [66], [93] for cascaded transformer multilevel inverters, the operation principle can be extended to a power converter with multiple modules connected to isolated PV panels. Additionally, a mathematical analysis is required to provide a reliable model of the configuration proposed.

- Control architecture

Based on the concept described in [101] a control algorithm can be proposed to regulate the voltage level and current injected to the grid. This PhD dissertation will focus on providing a control architecture to achieve the requirements described by introducing an algorithm where the output and the circulating currents are regulated. Further enhancements are proposed to solve technical aspects which include power imbalances due to unpredictive conditions in the primary sources, allowing at any time the maximum power point operation.

- Evaluation methods

The isolated multilevel converter is evaluated based on the equivalent model proposed. Through this model approach, accurate simulations are presented and executed under several scenarios. In order to create a more realistic environment, several imbalance power operation states are analyzed and evaluated under two different control strategies. Additionally, a downscale prototype is built to reinforce through experimental results the scope of this PhD dissertation.

1.4 Outline of the PhD Dissertation

The following chapters in this PhD dissertation are organized as follows.

Chapter 2 introduces the Isolated Multi-Modular Converter (IMMC) proposed. First, the single-phase IMMC is studied based on an equivalent model per arm. This is followed by the energy analysis that aim at defining the power response based on the output and circulating current components. Afterwards, the three-phase IMMC is studied using a matrix representation, providing y simplified model of the converter. Then, the energy is studied using a similar analysis to the one introduced in the single-phase configuration.

In chapter 3, the control architecture of the IMMC is defined. The analysis includes the control design of the output current, the circulating current and the average dc voltage per arm. The tuning of the control parameters is performed using the phase margin and crossover frequency technic. Then, the central control architecture used to regulate the average dc voltage is introduced.

Chapter 4 exhibits two control strategies to withstand power imbalances as a result of mismatches in the primary sources. These control strategies are embedded in each module and are responsible of adjusting the modulated voltage given by the central controller. Afterwards, both control strategies are combined, demonstrating the higher capability of tolerating larger power imbalances in comparison to the control strategies operating individually. Additionally, this chapter includes experimental results by using a downscale protype.

Finally, chapter 5 draws the conclusions of this dissertation and identifies possible open points to be discussed in future works.

1.5 List of publications and contributions

This section includes the main contributions of this PhD thesis, classified as journals, conferences papers and patents. Some of the contributions deviate slightly from the main topic of this work. However, they complement and reinforce the knowledge obtained during this journey.

The first three journal papers are the main contribution of this PhD dissertation and are the publications used to fulfill the requirements of this program. Their topics cover the concept behind the Isolated Multi-Modular Converter, including different control strategies to operate under imbalance power scenarios. The analysis and results are introduced in the next chapters and discussed with more details in each publication. Additionally, some conference papers and one patent has been published to provide partial results about the converter proposed for photovoltaic energy systems.

The remaining contributions cover other aspects of photovoltaic applications. They describe a control strategy proposed for grid support functionalities and a cascaded converter with ac isolation provided by a custom active transformer. Both concepts have been studied in collaboration with other researchers. The control proposed is called Synchronous Central Angle Controller and its purpose is to emulate the inherent inertia response of a synchronous generator in a PV power plant. On the other hand, the cascaded

converter based on a custom active transformer provides galvanic isolation, while the series connection is given by the magnetic circuit of the transformer.

1.5.1 Journal Papers:

1. **C. Verdugo**, J. I. Candela, F. Blaabjerg and P. Rodriguez, "Three-Phase Isolated Multimodular Converter in Renewable Energy Distribution Systems," in IEEE Journal of Emerging and Selected Topics in Power Electronics, vol. 8, no. 1, pp. 854-865, March 2020.
2. **C. Verdugo**, J. I. Candela and P. Rodriguez, "Energy Balancing with Wide Range of Operation in the Isolated Multi-Modular Converter," in IEEE Access, vol. 8, pp. 84479-84489, 2020.
3. **C. Verdugo**, J. I. Candela and P. Rodriguez, "Quadrature Voltage Compensation in the Isolated Multi-Modular Converter", Energies 2021
4. **C. Verdugo**, A. Tarraso, J. I. Candela, J. Rocabert and P. Rodriguez, " Centralized Synchronous Controller based on Load Angle Regulation for Photovoltaic Power Plants," in IEEE Journal of Emerging and Selected Topics in Power Electronics, 2020.
5. A. Tarrasó, Ngoc-B. Lai, **C. Verdugo**, J. I. Candela and P. Rodriguez, "Design of Controller for Virtual Synchronous Power Plant", in IEEE Industry Applications, 2021.

1.5.2 Conference papers:

1. **C. Verdugo**, A. Tarraso, J. I. Candela, J. Rocabert and P. Rodriguez, "Synchronous Frequency Support of Photovoltaic Power Plants with Inertia Emulation," 2019 IEEE Energy Conversion Congress and Exposition (ECCE), Baltimore, MD, USA, 2019, pp. 4305-4310.
2. **C. Verdugo**, J. I. Candela, M. A. Elsaharty and P. Rodriguez, "Multilevel Single Phase Isolated Inverter with Reduced Number of Switches," 2018 7th International Conference on Renewable Energy Research and Applications (ICRERA), Paris, 2018, pp. 1202-1208.
3. **C. Verdugo**, M. Atef Elsaharty and P. Rodriguez, "Integrated Series Transformer in Cascade Converters for Photovoltaic Energy Systems," 2018 IEEE Energy Conversion Congress and Exposition (ECCE), Portland, OR, 2018, pp. 6263-6269.

4. **C. Verdugo**, J. I. Candela, F. Blaabjerg and P. Rodriguez, "Model and control of the isolated multi-modular converter," IECON 2017 - 43rd Annual Conference of the IEEE Industrial Electronics Society, Beijing, 2017, pp. 1286-1292.
5. **C. Verdugo**, J. I. Candela, A. Luna and P. Rodriguez, "Power station for large scale photovoltaic power plants," 2017 IEEE 6th International Conference on Renewable Energy Research and Applications (ICRERA), San Diego, CA, 2017, pp. 768-773.
6. **C. Verdugo**, J. I. Candela and P. Rodriguez, "Re-synchronization strategy for the synchronous power controller in HVDC systems," 2017 IEEE Energy Conversion Congress and Exposition (ECCE), Cincinnati, OH, 2017, pp. 5186-5191.
7. **C. Verdugo**, J. I. Candela and P. Rodriguez, "Local and centralized control strategy for capacitor voltage balancing of modular multilevel converter," 2016 IEEE International Conference on Renewable Energy Research and Applications (ICRERA), Birmingham, 2016, pp. 253-258.
8. **C. Verdugo**, J. I. Candela and P. Rodriguez, "Grid support functionalities based on modular multilevel converters with synchronous power control," 2016 IEEE International Conference on Renewable Energy Research and Applications (ICRERA), Birmingham, 2016, pp. 572-577.
9. A. Tarraso, **C. Verdugo**, N. B. Lai, J. Ignacio Candela and P. Rodriguez, "Synchronous Power Controller for Distributed Generation Units," 2019 IEEE Energy Conversion Congress and Exposition (ECCE), Baltimore, MD, USA, 2019, pp. 4660-4664.

1.5.3 Patents:

1. **C. Verdugo**, P. Rodriguez, J. Ignacio Candela, A. Luna and J. Rocabert, “Convertidor Modular Multinivel con Transformadores de Aislación”, Spain, 2018, Patent number ES2684445A1.

Chapter 2.

Isolated Multi-Modular Converter

This chapter explains the fundamental principle and the main functionalities of the single and three-phase Isolated Multi-Modular Converter (IMMC). The chapter starts by studying the output current, the circulating current and the total dc voltage models for a single-phase configuration. Then, in the three-phase configuration, the IMMC is described based on two independent electrical circuits which represent the entire behavior of the converter operation. The main concept of this chapter is covered by the publication: C. Verdugo, J. I. Candela, F. Blaabjerg and P. Rodriguez, "Three-Phase Isolated Multi-Modular Converter in Renewable Energy Distribution Systems," in IEEE Journal of Emerging and Selected Topics in Power Electronics. JESTPE.2020.

2.1 Single-phase configuration

The mathematical model of the IMMC carried out in this chapter is based on the converter diagram shown in Fig. 2.1. Although the three-phase configuration is the main concern of this work, there is a direct relationship between the single-phase and the three-phase structure. Therefore, the dynamic model can be properly studied in a single-phase system and later extended to more phases.

The IMMC is formed by two arms referred as upper and lower arms. They are connected in parallel through a coupling inductance L_T and a common neutral point *n*, as seen in Fig.

2.1. Each arm has *N* modules in series connection which are formed by a dc source v_{dc}, a dc-ac inverter and an ac transformer T_R. All modules are electrically connected through the secondary winding of each transformer giving rise to a stepped voltage v_o. The number of voltage levels are directly related to the ac-dc topology used and the number of modules connected in series.

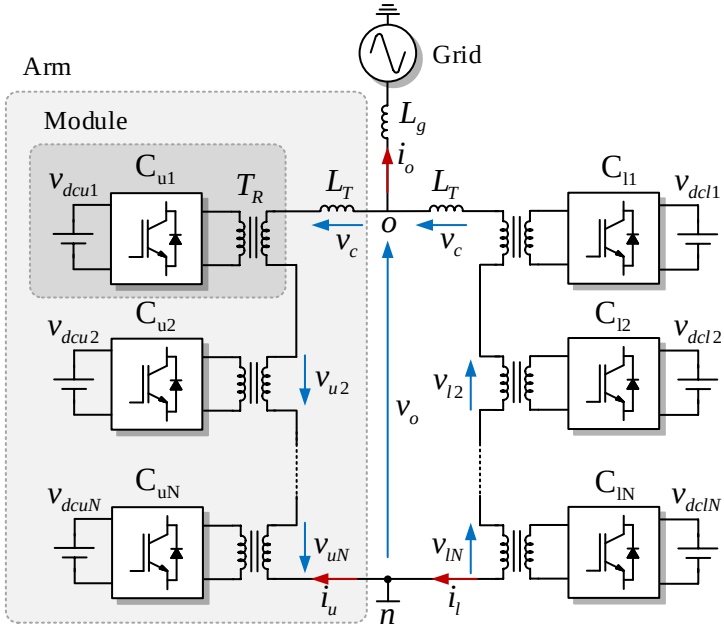

Fig. 2.1. Isolated Multi-Modular Converter (IMMC)

To provide a bidirectional power flow, each dc-ac inverter is represented through an H-bridge configuration as shown in Fig. 2.2. The inverter has two legs and each of them has two switches operating in unipolar modulation [102]. Therefore, three voltage levels are achieved at the ac side $v_{i,k,T}$. Generally, an Insulated Gate Bipolar Transistor (IGBT) with an anti-parallel diode is employed as a switching device. However, for higher commutation speed and greater efficiency during operation at low voltages, MOSFET (Metal Oxide Field Effect Transistor) are more suited. The control signals for the upper switches are numbered as s_1 and s_2, meanwhile the control signals for the lower switches are numbered as s_3 and s_4 respectively. The dc side is connected to a dc capacitor which maintains the dc voltage approximately constant, regardless the current level in the ac side.

The switching states are commanded through a pulse width modulation strategy in which a high frequency triangle waveform, the carrier signal, is compare with a slow frequency waveform known as the modulation signal. The comparison between the carrier and the

modulation signal provides the switching states. These states are defined as 1 when the switching device is turned on and 0 when the switching is turned off.

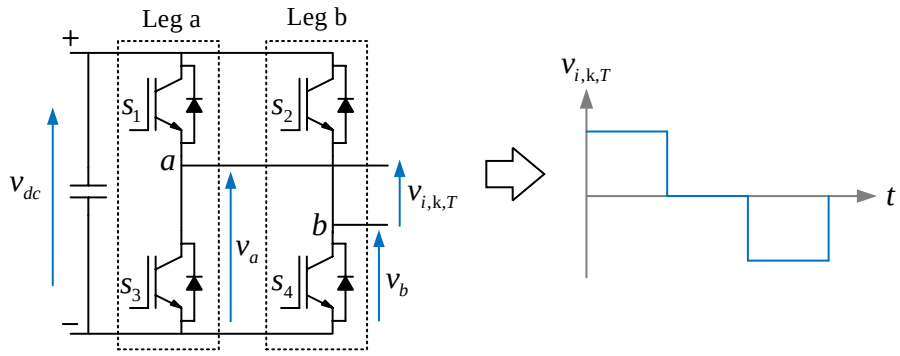

Fig. 2.2. H-Bridge module of the isolated multi-modular converter

For the purpose of providing galvanic isolation between the dc and ac side, the ac terminals are connected to a low frequency transformer. In this sense, the dc side is totally isolated from the series-connected modules, avoiding high floating voltages in the external dc source due to high voltage levels generated at the ac side. Remember that the insulation constrain in PV panels limit the maximum voltage level unless a high or low frequency isolation stage is included.

2.1.1 Fundamental principle

The operation principle of the IMMC can be studied from the dynamic model presented in this section, which is geared towards the average model of a single-phase configuration and later extended to three-phases. This model provides the basis for the control design presented in next chapter.

As reported earlier, the IMMC is formed by two arms connected in parallel through a coupling inductance L_T and a common connection point *n*. According to Fig. 2.1, through the upper arm flows the current i_u, while in the lower arm flows the current i_l. The upper and the lower current arms depend on the power supplied by the arm and the voltage level achieved in the output terminals. By definition from the nomenclature presented in Fig. 2.1 and according to the Kirchhoff's current law, the current difference between i_u and i_l provides the output current injected into the grid by means of the following expression:

$$i_o = i_u - i_l \tag{2.1}$$

The parallel connection between the arms and the possibility of power imbalances between modules will result in a circulating current flowing through the converter. According to Fig. 2.1, the circulating current also knows as internal current is represented by the addition of the upper and lower current arms as follows.

$$i_c = \frac{i_u + i_l}{2} \tag{2.2}$$

Previous expression considers a circulating current flowing from the upper to the lower arm, which does not have any influence on the output current. In contrast to the MMC, where the upper arm is connected to the positive pole of the dc side and the lower arm to the negative pole, i.e. a dc current flows to maintain a dc voltage in each module, the IMMC has independent dc sources connected. Therefore, no dc current flows through the arms.

Combining the output and the circulating current expressions described in (2.2), it is possible to define the current arms as:

$$\begin{aligned} i_u &= \frac{i_o}{2} + i_c \\ i_l &= -\frac{i_o}{2} + i_c \end{aligned} \tag{2.3}$$

The mathematical model of the IMMC studies the dynamic response of the current and voltage signals. Focus our attention on the circuit formed by each arm, the voltage in the upper and lower arms are described by:

$$\begin{aligned} v_u &= -v_c - v_o \\ v_l &= v_o - v_c \end{aligned} \tag{2.4}$$

Where v_u and v_l represent the equivalent voltage arms, v_o represents the output voltage generated between the upper and lower arms and v_c represents the internal voltage drop in the coupling inductance L_T. Further down, we will show how the output voltage drives the output current, while the internal voltage drives the circulating current.

Note that the addition of the voltages $-v_c$ and $-v_o$ gives rise to the total voltage in the upper arm, while the difference between the voltages v_o and v_c generates the total voltage in the lower arm. By adding the expressions presented in equation (2.4), the internal voltage is reduced to:

$$v_c = -\frac{v_u + v_l}{2} \tag{2.5}$$

Considering the fact that each module generates an output voltage $v_{i,k}$ in the secondary side of the transformer, where i represents the upper or the lower arm and k represents the number of module. The total voltage in one arm is given by the series connection of modules as follows.

$$v_i = \sum_{k=1}^{N} v_{i,k} \tag{2.6}$$

This expression describes the behavior of the entire arm as an equivalent module. The switching function of each H-bridge can be used to determine the instantaneous value of the current and voltage signals. However, for a dynamic analysis, the high frequency components in the switching devices are often neglected, as the control loop and the filters typically have a low-pass response. For this reason, the output voltage can be studied in terms of its average value rather than its instantaneous value. The average model of the H-bridge allows to describe the converter based on the modulation index and the dc voltage level through:

$$v_{i,k} = v_{dc,i,k} m_{i,k} \tag{2.7}$$

The modulation index $m_{l,k}$ describes the relationship between the dc voltage and the ac voltage. Its value operates between -1 and 1. Consequently, the voltage $v_{i,k}$ describes a lineal response between the positive and negative value of $v_{dc,i,k}$. The total voltage arm can be expressed in terms of the modulation index by substitution of equation (2.7) in expression (2.6) as.

$$v_i = \sum_{k=1}^{N} v_{dc,i,k} m_{i,k} \tag{2.8}$$

Since external dc sources are connected to each module, different dc voltage levels can appear. However, as a first approach, we can assume that all modules operate at similar dc voltage levels. Although, this is not the most realistic scenario as we will describe in next chapter. Considering N modules per arm, the total voltage in equation (2.8) can be replaced by:

$$v_i = \frac{v_{dc,i}^{\Sigma}}{N} \sum_{k=1}^{N} m_{i,k} \tag{2.9}$$

Each dc capacitor is charged with the mean voltage $v_{dc,i}^{\Sigma} / N$, where $v_{dc,i}^{\Sigma}$ represents the sum of all dc voltages measured in one arm. The second part of equation (2.9) can be replaced by introducing the mean modulation index through the following expression:

$$m_i = \frac{1}{N}\sum_{k=1}^{N} m_{i,k} \tag{2.10}$$

As was aforementioned, the modulation index $m_{i,k}$ operates between -1 and 1. According to (2.10), if all modules generate their maximum voltage, the sum of $m_{i,k}$ will be N. On the other hand, if all modules generate their minimum voltage, the sum of $m_{i,k}$ will be $-N$. Therefore, the average modulation index also operates between -1 to 1.

Substituting the average modulation index of equation (2.10) in equation (2.9), the total voltage arm yields.

$$v_i = v_{dc,i}^{\Sigma} m_i \tag{2.11}$$

The average model can be used for analysis and for control design of the IMMC. This model disregards the switching states, representing each module as a controlled voltage source.

2.1.2 Output and circulating current model

The operation principle and the dynamic response of the output and circulating currents can be studied from the electric model of the single-phase configuration shown in Fig. 2.3. Assuming a dc bus well-balanced in all modules, the upper and lower arm can be considered as series-connected controlled voltage sources, in which each source represents the simplified model of one module. The controlled voltage sources are defined according to equation (2.7) and the total voltage arm is described by equation (2.11).

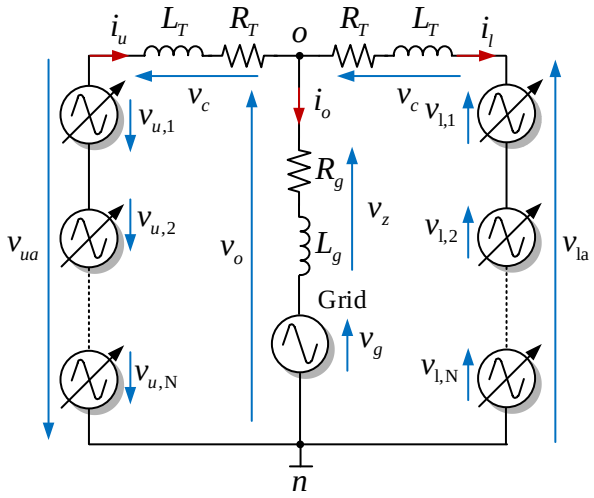

Fig. 2.3. Electric model of the single-phase IMMC

The ac terminals between the coupling inductance L_T and the common point n are connected to the ac grid v_g through a L_g inductance and a R_g resistance, which represent the grid impedance. Additionally, a R_T resistance is included in the arm just for modelling the losses in the series-connected modules. Focus our attention in the close circuit formed by the arms, the dynamic model of the upper and lower arm is given by:

$$\begin{aligned} R_T i_u + L_T \frac{di_u}{dt} &= -v_u - v_o \\ R_T i_l + L_T \frac{di_l}{dt} &= v_o - v_l \end{aligned} \tag{2.12}$$

Remember that the series-connected modules provide the total voltage arms v_u and v_l respectively. By adding and subtracting previous expressions, it is possible to define the dynamic model in terms of the internal and external signals of the converter. Note that the current arms have been replaced by the circulating and output current through equations (2.1) and (2.2).

$$\begin{aligned} \frac{R_T}{2} i_o + \frac{L_T}{2} \frac{di_o}{dt} &= \frac{-v_u + v_l}{2} - v_o = v_s - v_o \\ R_T i_c + L_T \frac{di_c}{dt} &= -\frac{v_u + v_l}{2} = v_c \end{aligned} \tag{2.13}$$

The difference between the total voltage arm v_s and the output voltage v_o drives the output current, whereas the internal voltage drop v_c drives the circulating current.

The substitution of the average modulation index described in equation (2.11) in the close circuit formed by the arms in equation (2.13) defines the average model.

$$\begin{aligned} \frac{R_T}{2} i_o + \frac{L_T}{2} \frac{di_o}{dt} &= \frac{-v_{dc,\mathrm{u}}^{\Sigma} m_u + v_{dc,l}^{\Sigma} m_l}{2} - v_o \\ R_T i_c + L_T \frac{di_c}{dt} &= -\frac{v_{dc,\mathrm{u}}^{\Sigma} m_u + v_{dc,l}^{\Sigma} m_l}{2} \end{aligned} \tag{2.14}$$

The advantage of representing the voltages in terms of the average modulation indexes becomes evident in (2.14). As m_i changes from -1 to 1, the total voltage in the upper and lower arms operate between $-v_{dc,i}^{\Sigma}$ and $v_{dc,i}^{\Sigma}$. This representation will help us to determine the relationship between the output and circulating currents with regard to the average modulation indexes and the total dc voltages. For instance, if we consider a similar voltage value in the upper and lower arm, i.e. $v_{dc,u}^{\Sigma} = v_{dc,l}^{\Sigma} = v_{dc}^{\Sigma}$ and an average modulation index equal to -1 in the upper arm and 1 in the lower arm, the voltage $v_s = v_{dc}^{\Sigma}$ and the internal

voltage drop v_c is equal to zero. Therefore, the output current is driven by v_{dc}^{Σ} and no circulating current flows through the arms. Instead, if the modulation index $m_u = 0$ and m_l reaches its maximum value, the internal voltage drop will be different from zero and thus a circulating current will flow through the arms.

The average modulation index controls the output and the circulating currents through the voltage arms. In order to find an appropriate value for the modulation indexes, the voltage difference v_s and the drop voltage v_c in equation (2.13) can be replaced by equation (2.14), giving rise to the following expressions.

$$\begin{aligned} m_u &= \frac{1}{v_{dc,u}^{\Sigma}}(-v_s - v_c) \\ m_l &= \frac{1}{v_{dc,l}^{\Sigma}}(v_s - v_c) \end{aligned} \tag{2.15}$$

The appropriate value for v_s and v_c define the modulation index reference to control the upper and lower current arms.

Using the output and the circulating current models described previously, the IMMC can be represented through the block diagram depicted in Fig. 2.4. This diagram introduces equations (2.14) and (2.15) respectively. The input signals of the model are the average modulation indexes, which are multiplied and decoupled to define the voltages v_s and v_c. Then, the voltages are used by the transfer function blocks which represent the dynamic model of equation (2.14) to generate the output and the circulating currents.

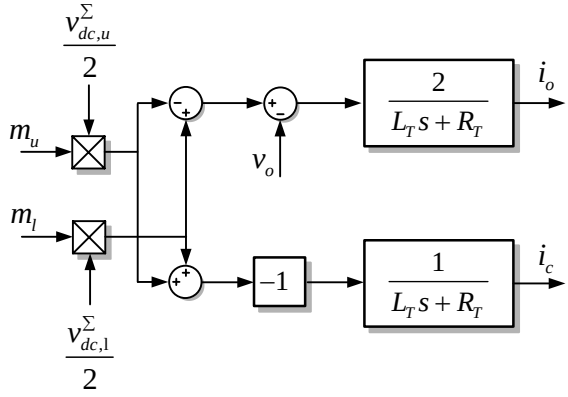

Fig. 2.4. Average current model of the IMMC

2.1.3 Average dc voltage model

Previously, it was demonstrated how the inner current model set the output and the circulating current through the modulation index in the upper and lower arms. The theory presented in previous section states that the voltage difference v_s affects the output current behavior, and the drop voltage v_c affects the circulating current. Now, it is necessary to define the appropriate output and circulating current references which define the converter operation between the arms.

Considering the current and voltage nomenclature used in the average model of Fig. 2.3, the total power in one arm is given by:

$$P_{oi} = \sum_{k=1}^{N} P_{oi,k} \tag{2.16}$$

Where P_{oi} is the total power produced by the arm i and $P_{oi,k}$ is the power produced by the module k. This power is commanded by the voltage in the ac terminals $v_{i,k}$ and the current arm.

$$P_{oi} = \sum_{k=1}^{N} v_{i,k} i_i \tag{2.17}$$

The purpose of the active and reactive power loops is to define the power exchange between the external sources connected to the dc terminals and the ac grid. In many applications such as PV systems, the dc bus is not fixed, being affected by the active power delivered or absorbed from the grid. Hence, the dc-bus must be regulated to set the correct power level.

Considering an ideal dc source which enables a bidirectional power flow, the power balance in one module is described by:

$$P_{oi,k} = P_{dci,k} - P_{ci,k} \tag{2.18}$$

Where $P_{dci,k}$ is the power produced by the external dc source and $P_{ci,k}$ is the rate of change of the energy in the dc-bus capacitor. The representation of the power balance is illustrated in Fig. 2.5, where the conduction and switching losses have been neglected and the power generated by the external dc source is defined by the voltage $v_{dci,k}$ and the current $i_{dci,k}$.

The power produced by the series connection of modules gives rise to the total power P_{oi}. This power is reduced to.

$$P_{oi} = \sum_{k=1}^{N} P_{dci,k} - \sum_{k=1}^{N} P_{ci,k} \tag{2.19}$$

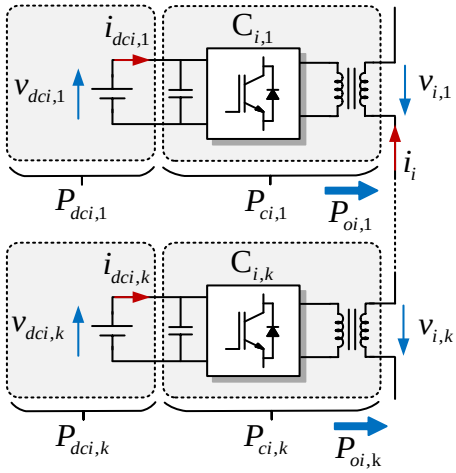

Fig. 2.5 Power exchange representation of *N* modules in series-connection

The rate of change of the energy in the dc-bus capacitor defines the dynamic response of the voltage in the dc terminals and thus, the power exchange with the ac grid. The rate of change in the dc voltage is represented by:

$$P_{ci,k} = \frac{C_{sm}}{2} \frac{dv_{dci,k}^2}{dt} \tag{2.20}$$

Where C_{sm} is the dc capacitor. Using expression (2.20) in (2.19), the total rate of change of energy in one arm is defined as.

$$\sum_{k=1}^{N} P_{ci,k} = \frac{d}{dt} \sum_{k=1}^{N} \frac{C_{sm}}{2} v_{dci,k}^2 \tag{2.21}$$

It is expected that all modules are connected to power sources with similar dc voltage levels. Therefore, as was described in equation (2.9), we can assume a dc voltage equal to the mean value v_{dci}^{Σ} / N in all modules. Hence, the relation described in equation (2.21) can be rewritten as:

$$\begin{aligned} \sum_{k=1}^{N} P_{ci,k} &= \frac{d}{dt} \sum_{k=1}^{N} \frac{C_{sm}}{2} \left(\frac{v_{dci}^{\Sigma}}{N} \right)^2 \\ &= \frac{C_{sm}}{2N} \frac{d}{dt} \left(v_{dci}^{\Sigma} \right)^2 \end{aligned} \tag{2.22}$$

Where C_{sm} / N represents the equivalent capacitance in one arm. Combining the power balance expression and the total rate of change of the energy, the relationship between the dc voltage and the active power is given by:

$$\begin{aligned}\frac{C_{sm}}{2N}\frac{d}{dt}\left(v_{dci}^{\Sigma}\right)^2 &= \sum_{k=1}^{N} P_{dci,k} - p_{oi} \\ &= \Delta P_i\end{aligned} \tag{2.23}$$

The expression (2.23) proves how a dc voltage variation increases or decreases the power exchange between a dc source and the ac grid. When the external dc sources are affected but unpredictable conditions, there is not a direct control over $P_{dci,k}$. Therefore, it is considered as a disturbance, while P_{oi} is the control variable.

To find a relationship between the current arms and the dc voltage, we need to find the relationship between the current and the power arms. Defining P_{ou} as the upper power and P_{ol} as the lower power arm, the total power delivered or absorbed from the ac grid P_T is given by.

$$P_T = P_{ou} + P_{ol} \tag{2.24}$$

The theory introduced in equation (2.17) states that the power arms can be replaced by the voltage and current signals. Therefore, the power arms are given by:

$$\begin{aligned}P_{ou} &= v_u i_u \\ &= v_u\left(\frac{i_o}{2} + i_c\right)\end{aligned} \tag{2.25}$$

$$\begin{aligned}P_{ol} &= v_l i_l \\ &= v_l\left(-\frac{i_o}{2} + i_c\right)\end{aligned} \tag{2.26}$$

Replacing previous expressions in equation (2.24), we obtain:

$$P_T = \frac{i_o}{2}\left(v_u - v_l\right) + i_c\left(v_u + v_l\right) \tag{2.27}$$

Note that the voltage difference between the upper and lower arms is multiplied by the output current, while the addition of both voltages is multiplied by the circulating current. Normally, the voltage drop in the coupling inductance is considered significantly small compared to the voltage arms, i.e., it can be neglected. Hence, the voltage arms are simplified to.

$$\begin{aligned} v_u &\approx -v_o \\ v_l &\approx v_o \end{aligned} \tag{2.28}$$

Replacing the voltage arms in equation (2.27), the total power is reduced to.

$$P_T = -i_o v_o \tag{2.29}$$

Equation (2.29) states that P_T is driven by the output current. Therefore, the sum of the upper and lower power defined by the total dc voltage provides the output current reference.

Similar to previous analysis, the power difference between the upper and lower arms is used to generate the circulating current reference. This assumption makes sense since the circulating current arises when there is a power difference between both arms. The aforementioned will produce a current flowing through the arms without having any influence on the output current such as described in equation (2.1). Considering P_Δ as the power difference, we obtain:

$$P_\Delta = P_{ou} - P_{ol} \tag{2.30}$$

Replacing the power arm described in equations (2.25) and (2.26) in (2.30), the power difference is rewritten as:

$$P_\Delta = \frac{i_o}{2}\left(v_u + v_l\right) + i_c\left(v_u - v_l\right) \tag{2.31}$$

Note that the sum of the voltage arms is multiplied by the output current, while the difference between these voltages is multiplied by the circulating current. Replacing the expressions for the voltage arms outlined in (2.28), the addition of the voltage arm is eliminated and the relationship between the power difference and the circulating current is reduced to:

$$P_\Delta = -2 v_o i_c \tag{2.32}$$

In conclusion, with the total and the difference power expressions we can define the output and the circulating current references.

2.2 Three-phase IMMC

So far we have investigated the single-phase IMMC model, where the output and the circulating current represent the behavior of the upper and lower current arms. Henceforth, the three-phase IMMC is studied based on the fundamental principle described in section 2.1.1.

In the three-phase configuration we assume that the converter is connected to a three-phase ac grid, whose signals are shifted 120º. Each phase is denoted as *a*, *b* and *c* respectively, with the phase *a* set at 0º. In steady state operation the three phases are well balanced and have the following expressions.

$$\begin{aligned} v_a &= \hat{v}_a \cos(\omega t + \phi_v) \\ \mathrm{v}_b &= \hat{v}_b \cos(\omega t - 2\pi/3 + \phi_v) \\ \mathrm{v}_c &= \hat{v}_c \cos(\omega t + 2\pi/3 + \phi_v) \end{aligned} \tag{2.33}$$

Where $\hat{v}$ is the voltage amplitude, ω is the grid frequency and ϕ_v is the phase angle. A similar analysis can be introduced in the grid currents, which are defined as:

$$\begin{aligned} i_a &= \hat{i}_a \cos(\omega t + \phi_i) \\ i_b &= \hat{i}_b \cos(\omega t - 2\pi/3 + \phi_i) \\ i_c &= \hat{i}_c \cos(\omega t + 2\pi/3 + \phi_i) \end{aligned} \tag{2.34}$$

The current amplitude is denoted by $\hat{i}$ and its phase angle by ϕ_i. Note that an angle difference between ϕ_v and ϕ_i will affect the active and reactive power flow in the converter.

2.2.1 Stationary and synchronous reference frame

The stationary reference frame denoted as $\alpha\beta 0$ -frame is implemented to define a three-phase system into an equivalent two-phase sinusoidal system whose signals are shifted 90º and a zero-component produced by an unbalance operation. The α and β coordinates represent the real and the imaginary axes and are used to define a space vector signal. According to (2.35), the matrix transposition T_{C3} multiplies the three-phase signals in order to define the $\alpha\beta 0$ components. This mathematical transformation is also known as the Clark transformation.

$$\begin{bmatrix} f_\alpha \\ f_\beta \\ f_o \end{bmatrix} = \frac{2}{3} \begin{bmatrix} 1 & -1/2 & -1/2 \\ 0 & \sqrt{3}/2 & -\sqrt{3}/2 \\ 1/2 & 1/2 & 1/2 \end{bmatrix} \begin{bmatrix} f_a \\ f_b \\ f_c \end{bmatrix} \tag{2.35}$$

As previous expression provides the $\alpha\beta 0$ components from a three-phase system, the inverse transform T_{C3}^{-1} can be used to generate the three-phase signals from the $\alpha\beta 0$ reference frame.

$$\begin{bmatrix} f_a \\ f_b \\ f_c \end{bmatrix} = \begin{bmatrix} 1 & 0 & 1 \\ -1/2 & \sqrt{3}/2 & 1 \\ -1/2 & -\sqrt{3}/2 & 1 \end{bmatrix} \begin{bmatrix} f_\alpha \\ f_\beta \\ f_o \end{bmatrix} \tag{2.36}$$

The variables f_α and f_β represent the projections of the space vector signal $\vec{f}_{\alpha\beta}$ on the real and the imaginary axes, whose definition is given by:

$$\vec{f}_{\alpha\beta} = f_\alpha + jf_\beta \tag{2.37}$$

The Clark transformation can be used to convert the current and voltage signals of the three-phase IMMC into the $\alpha\beta 0$-frame and thus, control the output and the circulating current through two independent systems. A second option is to use a synchronous reference frame denoted as *dq*-frame, which rotates the $\alpha\beta$ signals through an angle ωt, making it similar to a complex phasor with dc components at the fundamental frequency. This characteristic permits the implementation of PI compensators with simple structures to provide zero steady state error at the fundamental frequency.

Similar to the stationary reference frame, the dq-frame also known as Park transformation is defined by:

$$\vec{f}_{dq} = f_d + jf_q \tag{2.38}$$

The f_d and f_q signals represent the real and the imaginary components in a complex structure and are derived from the stationary reference frame through the following expression.

$$\begin{bmatrix} f_d \\ f_q \end{bmatrix} = \begin{bmatrix} \cos(\omega t) & \sin(\omega t) \\ -\sin(\omega t) & \cos(\omega t) \end{bmatrix} \begin{bmatrix} f_\alpha \\ f_\beta \end{bmatrix} \tag{2.39}$$

The matrix transformation can be represented using the complex expression through the Euler identity $e^{j\omega t}$. Note that the Park transformation can be applied not only to the fundamental frequency, but also to multiple frequencies to regulate harmonic components. To better describe the previous expression, the dq-frame transformation can be rewritten as:

$$\vec{f}_{dq} = \vec{f}_{\alpha\beta} e^{-j\omega t} = \vec{f}_{\alpha\beta}(\cos(\omega t) - j\sin(\omega t)) \tag{2.40}$$

Even though, a three-phase system can be performed either in the $\alpha\beta 0$ frame or the dq frame. The three-phase IMMC model will be studied in the $\alpha\beta 0$ frame and later extended to the dq frame.

2.2.2 Three-phase current model

The three-phase IMMC model presented in this section is based on the structure illustrated in Fig. 2.6. As the single-phase configuration, the three-phase IMMC is formed by two arms with several modules connected in series through the secondary side of three-phase transformers. The voltages $v_{u,abc}$ and $v_{l,abc}$ denote the equivalent upper and lower voltage arms, while $v_{c,abc}$ denotes the voltage drop in the coupling inductance. The current arms flow through the converter, providing the three-phase output and circulating currents.

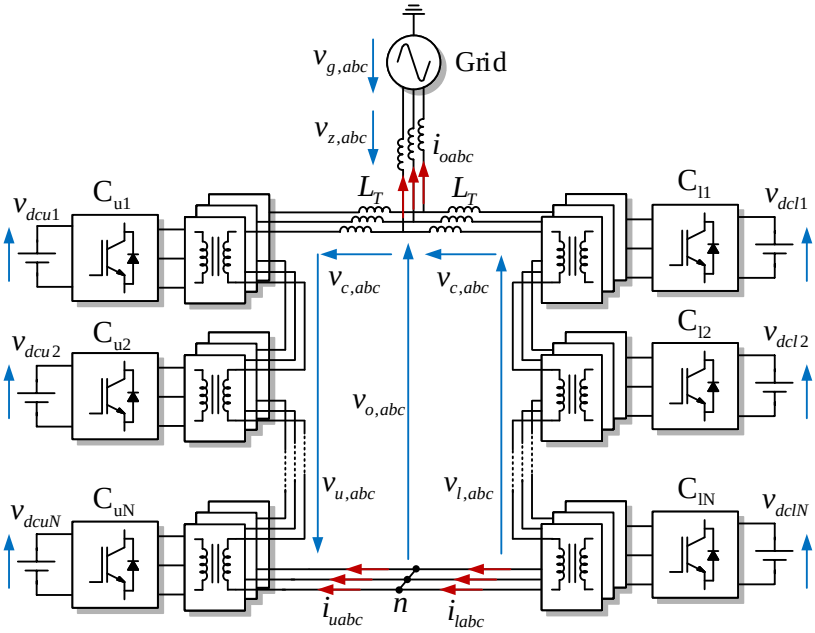

Fig. 2.6 Three-phase Isolated Multi-Modular Converter

The mathematical model of the three-phase converter can be studied considering the electrical model of Fig. 2.7. A controlled voltage source represent the voltage arm v_u and v_l. The coupling inductance L_T in series with a resistance R_T model the equivalent inductance and arm losses. The output voltage v_o measured between the connection point of both arms and the common point n represents the output voltage of the converter. The six equations which define the dynamic model per arm are described in (2.41).

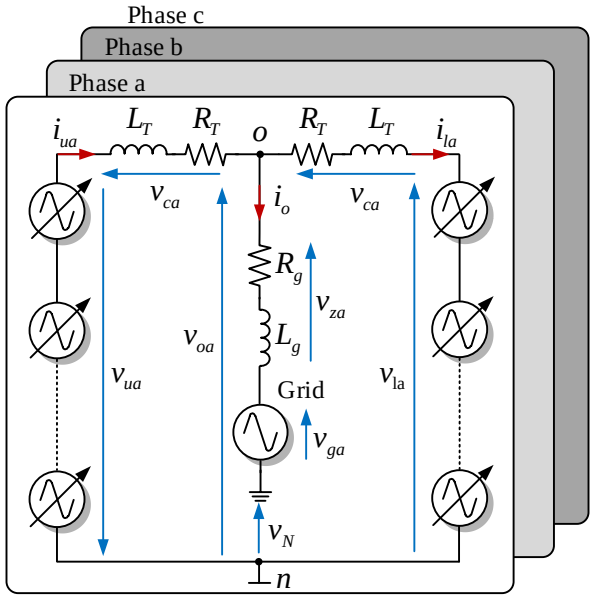

Fig. 2.7 Electric model of the three-phase IMMC

$$
\begin{aligned}
v_{ua} &= -L_T \frac{di_{ua}}{dt} - R_T i_{ua} - v_{oa} \\
v_{ub} &= -L_T \frac{di_{ub}}{dt} - R_T i_{ub} - v_{ob} \\
v_{uc} &= -L_T \frac{di_{uc}}{dt} - R_T i_{uc} - v_{oc} \\
v_{la} &= -L_T \frac{di_{la}}{dt} - R_T i_{la} + v_{oa} \\
v_{lb} &= -L_T \frac{di_{lb}}{dt} - R_T i_{lb} + v_{ob} \\
v_{lc} &= -L_T \frac{di_{lc}}{dt} - R_T i_{lc} + v_{oc}
\end{aligned}
\tag{2.41}
$$

The mathematical model of equation (2.41) can be simplified in one single expression by replacing the voltage and current signals in a matrix form. To make this possible, the three-phase voltage and current signals are rewritten through the following expressions.

$$
\mathbf{i_o} = \begin{bmatrix} i_{oa} \\ i_{ob} \\ i_{oc} \end{bmatrix} \qquad \mathbf{i_c} = \begin{bmatrix} i_{ca} \\ i_{cb} \\ i_{cc} \end{bmatrix} \qquad \mathbf{i_u} = \begin{bmatrix} i_{ua} \\ i_{ub} \\ i_{uc} \end{bmatrix} \qquad \mathbf{i_l} = \begin{bmatrix} i_{la} \\ i_{lb} \\ i_{lc} \end{bmatrix} \tag{2.42}
$$

$$\mathbf{v_i} = \begin{bmatrix} v_{ia} \\ v_{ib} \\ v_{ic} \end{bmatrix} \qquad \mathbf{v_c} = \begin{bmatrix} v_{ca} \\ v_{cb} \\ v_{cc} \end{bmatrix} \qquad \mathbf{v_s} = \begin{bmatrix} v_{sa} \\ v_{sb} \\ v_{sc} \end{bmatrix} \qquad \mathbf{v_o} = \begin{bmatrix} v_{oa} \\ v_{ob} \\ v_{oc} \end{bmatrix} \tag{2.43}$$

Now the six equations described in (2.41) can be rewritten as.

$$\begin{bmatrix} \mathbf{v_u} \\ \mathbf{v_l} \end{bmatrix} = \begin{bmatrix} -\mathbf{L_T} & 0 \\ 0 & -\mathbf{L_T} \end{bmatrix} \frac{d}{dt} \begin{bmatrix} \mathbf{i_u} \\ \mathbf{i_l} \end{bmatrix} + \begin{bmatrix} -\mathbf{R_T} & 0 \\ 0 & -\mathbf{R_T} \end{bmatrix} \begin{bmatrix} \mathbf{i_u} \\ \mathbf{i_l} \end{bmatrix} + \begin{bmatrix} -\mathbf{v_o} \\ \mathbf{v_o} \end{bmatrix} \tag{2.44}$$

The matrix $\mathbf{L_T}$ and $\mathbf{R_T}$ are 3x3 diagonal matrixes, which are defined in term of the coupling inductance and the series resistance.

$$\mathbf{L_T} = \begin{bmatrix} L_T & 0 & 0 \\ 0 & L_T & 0 \\ 0 & 0 & L_T \end{bmatrix} \qquad \mathbf{R_T} = \begin{bmatrix} R_T & 0 & 0 \\ 0 & R_T & 0 \\ 0 & 0 & R_T \end{bmatrix} \tag{2.45}$$

To determine the output and the circulating current model, similar to the single-phase configuration presented in (2.13), we define a matrix transformation which decouples the output and the circulating current by transforming the converter signals. The idea is exemplified below.

$$\begin{bmatrix} \mathbf{i_{o\alpha\beta}} \\ \mathbf{i_{c\alpha\beta}} \end{bmatrix} = T_{IMMC} \begin{bmatrix} \mathbf{i_u} \\ \mathbf{i_l} \end{bmatrix} \qquad \begin{bmatrix} \mathbf{i_u} \\ \mathbf{i_l} \end{bmatrix} = T_{IMMC}^{-1} \begin{bmatrix} \mathbf{i_{o\alpha\beta}} \\ \mathbf{i_{c\alpha\beta}} \end{bmatrix} \tag{2.46}$$

Where the current vectors $\mathbf{i_{o\alpha\beta}}$ and $\mathbf{i_{c\alpha\beta}}$ denote the output and the circulating currents in the $\alpha\beta 0$ frame.

$$\mathbf{i_{o\alpha\beta}} = \begin{bmatrix} i_{o\alpha} \\ i_{o\beta} \\ i_{oN} \end{bmatrix} \qquad \mathbf{i_{c\alpha\beta}} = \begin{bmatrix} i_{c\alpha} \\ i_{c\beta} \\ i_{cN} \end{bmatrix} \tag{2.47}$$

It is important to mention that the common mode of the output current is zero because the neutral is not connected to the grid. Furthermore, the circulating currents flow through the arms without affecting the ac side, therefore i_{cN} is also zero. Previous expressions are reduced to.

$$\mathbf{i_{o\alpha\beta}} = \begin{bmatrix} i_{o\alpha} \\ i_{o\beta} \\ 0 \end{bmatrix} \qquad \mathbf{i_{c\alpha\beta}} = \begin{bmatrix} i_{c\alpha} \\ i_{c\beta} \\ 0 \end{bmatrix} \tag{2.48}$$

The matrix transformation T_{IMMC} defines the output and the circulating currents from the current arms. Likewise, the inverse transformation T_{IMMC}^{-1} provides the current arms from the output and the circulating currents. Based on the Clark transform T_{C3} described in equation (2.35), the matrix T_{IMMC} and T_{IMMC}^{-1} are given by.

$$T_{IMMC} = \frac{1}{2}\begin{bmatrix} 2T_{C3} & -2T_{C3} \\ T_{C3} & T_{C3} \end{bmatrix} \qquad T_{IMMC}^{-1} = \frac{1}{2}\begin{bmatrix} T_{C3}^{-1} & 2T_{C3}^{-1} \\ -T_{C3}^{-1} & 2T_{C3}^{-1} \end{bmatrix} \tag{2.49}$$

The dynamic model of the three-phase IMMC presented in (2.44) can be rewritten introducing the inverse matrix transformation. Therefore, the output and the circulating current model results in.

$$T_{IMMC}^{-1}\begin{bmatrix} \mathbf{v}_{\Delta\alpha\beta 0} \\ \dfrac{\mathbf{v}_{\Sigma\alpha\beta 0}}{2} \end{bmatrix} = \begin{bmatrix} -\mathbf{L_T} & 0 \\ 0 & -\mathbf{L_T} \end{bmatrix} T_{IMMC}^{-1} \frac{d}{dt}\begin{bmatrix} \mathbf{i}_{o\alpha\beta} \\ \mathbf{i}_{c\alpha\beta} \end{bmatrix} + \begin{bmatrix} -\mathbf{R_T} & 0 \\ 0 & -\mathbf{R_T} \end{bmatrix} T_{IMMC}^{-1}\begin{bmatrix} \mathbf{i}_{o\alpha\beta} \\ \mathbf{i}_{c\alpha\beta} \end{bmatrix} + T_{IMMC}^{-1}\begin{bmatrix} -2\mathbf{v}_{o\alpha\beta} \\ 0 \end{bmatrix} \tag{2.50}$$

Note that the multiplication between the matrix transformation and the output voltage have the following expression.

$$\begin{bmatrix} -2\mathbf{v}_{o\alpha\beta} \\ 0 \end{bmatrix} = T_{IMMC}\begin{bmatrix} -\mathbf{v}_o \\ \mathbf{v}_o \end{bmatrix} \tag{2.51}$$

Where $\mathbf{v_{o\alpha\beta}}$ is given by.

$$\mathbf{v}_{o\alpha\beta} = \begin{bmatrix} v_{o\alpha} \\ v_{o\beta} \\ v_N \end{bmatrix} \tag{2.52}$$

The common mode voltage v_N is a fraction of the output voltage and it can be used to increase the ac voltage operation, avoiding overmodulation in large overshoots. Usually, the third harmonic injection method [103] can be introduced to modify the modulating signals, where the common mode voltage is represented as.

$$v_N = -\frac{1}{6}\hat{v}_g \cos(3\omega t) \tag{2.53}$$

Vectors $\mathbf{v_{\Delta\alpha\beta}}$ and $\mathbf{v_{\Sigma\alpha\beta}}$ represent the multiplication between the matrix transformation and the voltage arms. The voltage $\mathbf{v_{\Delta\alpha\beta}}$ is the difference voltage and $\mathbf{v_{\Sigma\alpha\beta}}$ is the total voltage in the $\alpha\beta 0$ coordinates. According to the single-phase model described in equation (2.13), the voltages v_Δ and v_Σ are reduced to.

$$\begin{bmatrix} \mathbf{v}_{s\alpha\beta} \\ \mathbf{v}_{c\alpha\beta} \end{bmatrix} = -\frac{1}{2}\begin{bmatrix} \mathbf{v}_{\Delta\alpha\beta} \\ 2\mathbf{v}_{\Sigma\alpha\beta} \end{bmatrix} \tag{2.54}$$

Applying equation (2.54) to equation (2.50) and multiplying them by the matrix transformation T_{IMMC} yields.

$$\begin{bmatrix} 2\mathbf{v}_{s\alpha\beta} \\ \mathbf{v}_{c\alpha\beta} \end{bmatrix} = T_{MMC}\begin{bmatrix} \mathbf{L_T} & 0 \\ 0 & \mathbf{L_T} \end{bmatrix}T_{MMC}^{-1}\frac{d}{dt}\begin{bmatrix} \mathbf{i}_{o\alpha\beta} \\ \mathbf{i}_{c\alpha\beta} \end{bmatrix} + T_{MMC}\begin{bmatrix} \mathbf{R_T} & 0 \\ 0 & \mathbf{R_T} \end{bmatrix}T_{MMC}^{-1}\begin{bmatrix} \mathbf{i}_{o\alpha\beta} \\ \mathbf{i}_{c\alpha\beta} \end{bmatrix} + \begin{bmatrix} 2\mathbf{v}_{o\alpha\beta} \\ 0 \end{bmatrix} \tag{2.55}$$

The multiplication between the matrix transformation and the diagonal matrix $\mathbf{L_T}$ and $\mathbf{R_T}$ give rise to.

$$\begin{bmatrix} \mathbf{L_T} & 0 \\ 0 & \mathbf{L_T} \end{bmatrix} = T_{MMC}\begin{bmatrix} \mathbf{L_T} & 0 \\ 0 & \mathbf{L_T} \end{bmatrix}T_{MMC}^{-1} \qquad \begin{bmatrix} \mathbf{R_T} & 0 \\ 0 & \mathbf{R_T} \end{bmatrix} = T_{MMC}\begin{bmatrix} \mathbf{R_T} & 0 \\ 0 & \mathbf{R_T} \end{bmatrix}T_{MMC}^{-1} \tag{2.56}$$

Finally, the three-phase output and circulating current models are reduced to.

$$\begin{bmatrix} \mathbf{R_T} & 0 \\ 0 & \mathbf{R_T} \end{bmatrix}\begin{bmatrix} \mathbf{i}_{o\alpha\beta} \\ \mathbf{i}_{c\alpha\beta} \end{bmatrix} + \begin{bmatrix} \mathbf{L_T} & 0 \\ 0 & \mathbf{L_T} \end{bmatrix}\frac{d}{dt}\begin{bmatrix} \mathbf{i}_{o\alpha\beta} \\ \mathbf{i}_{c\alpha\beta} \end{bmatrix} = \begin{bmatrix} 2\mathbf{v}_{s\alpha\beta} \\ \mathbf{v}_{c\alpha\beta} \end{bmatrix} + \begin{bmatrix} -2\mathbf{v}_{o\alpha\beta} \\ 0 \end{bmatrix} \tag{2.57}$$

The matrix form can be divided in two different expression, which associate the output and circulating current in two independent models.

$$\begin{aligned} \frac{\mathbf{R_T}}{2}\mathbf{i}_{o\alpha\beta} + \frac{\mathbf{L_T}}{2}\frac{d}{dt}\mathbf{i}_{o\alpha\beta} &= \mathbf{v}_{s\alpha\beta} - \mathbf{v}_{o\alpha\beta} \\ \mathbf{R_T}\mathbf{i}_{c\alpha\beta} + \mathbf{L_T}\frac{d}{dt}\mathbf{i}_{c\alpha\beta} &= \mathbf{v}_{c\alpha\beta} \end{aligned} \tag{2.58}$$

We can see the same expressions presented in the single-phase configuration of equation (2.13). However, as we have a three-phase system, the current and voltage signals are in $\alpha\beta 0$ coordinates.

Remember that the converter can be studied either in the $\alpha\beta 0$ frame or in the dq frame. By introducing the synchronous reference transformation presented in equation (2.40), the output and circulating current models are rewritten as.

$$\begin{aligned} \frac{\mathbf{R_T}}{2}\mathbf{i}_{odq}e^{j\omega t} + \frac{\mathbf{L_T}}{2}\frac{d}{dt}\mathbf{i}_{odq}e^{j\omega t} &= \mathbf{v}_{sdq}e^{j\omega t} - \mathbf{v}_{odq}{}^{j\omega t} \\ \mathbf{R_T}\mathbf{i}_{cdq}e^{j\omega t} + \mathbf{L_T}\frac{d}{dt}\mathbf{i}_{cdq}e^{j\omega t} &= \mathbf{v}_{cdq}e^{j\omega t} \end{aligned} \tag{2.59}$$

Decomposing (2.59) into real and imaginary components, we obtain:

$$\begin{aligned}\frac{R_T}{2}i_{od}+\frac{L_T}{2}\frac{di_{od}}{dt}-\frac{L_T\omega_s}{2}i_{oq}&=v_{sd}-v_{od}\\ \frac{R_T}{2}i_{oq}+\frac{L_T}{2}\frac{di_{oq}}{dt}+\frac{L_T\omega_s}{2}i_{od}&=v_{sq}-v_{oq}\end{aligned} \tag{2.60}$$

$$\begin{aligned}R_T i_{cd}+L_T\frac{di_{cd}}{dt}-L_T\omega_s i_{cq}&=v_{cd}\\ R_T i_{cq}+L_T\frac{di_{cq}}{dt}+L_T\omega_s i_{cd}&=v_{cq}\end{aligned} \tag{2.61}$$

Note that the derivative component in dq frame has a cross coupling between the dq axes in the output and circulating current models, later we will introduce a decoupled current feedback to remove these components and increase the performance of the current controllers [104].

The voltage difference $\mathbf{v_{sdq}}$ and the drop voltage $\mathbf{v_{cdq}}$ can be replaced in term of the average modulation indexes. According to (2.15), the three-phase modulation indexes in the upper and lower arm are reduced to.

$$\mathbf{m_{udq}}=\frac{1}{v_{dc,u}^{\Sigma}}(-\mathbf{v_{sdq}}-\mathbf{v_{cdq}}) \tag{2.62}$$

$$\mathbf{m_{ldq}}=\frac{1}{v_{dc,l}^{\Sigma}}(\mathbf{v_{sdq}}-\mathbf{v_{cdq}}) \tag{2.63}$$

The dq-frame model and the modulation indexes presented in (2.62) and (2.63) can be used to describe the three-phase output and circulating current behavior. The block diagrams illustrated in Fig. 2.8 and Fig. 2.9 show the representation of these currents. The input signals are the modulation vectors $\mathbf{m_{udq}}$ and $\mathbf{m_{ldq}}$ which set the voltage difference $\mathbf{v_{sdq}}$ and the drop voltage $\mathbf{v_{cdq}}$ respectively. Then, the real and the imaginary voltage components are decoupled and processed through the transfer functions of the dynamic model in Laplace transform to define the output and the circulating currents.

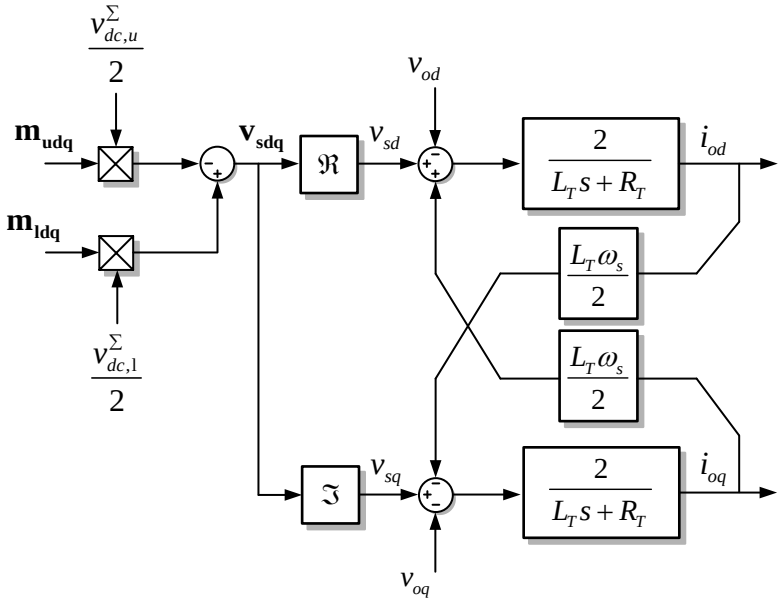

Fig. 2.8 Thee-Phase output current model

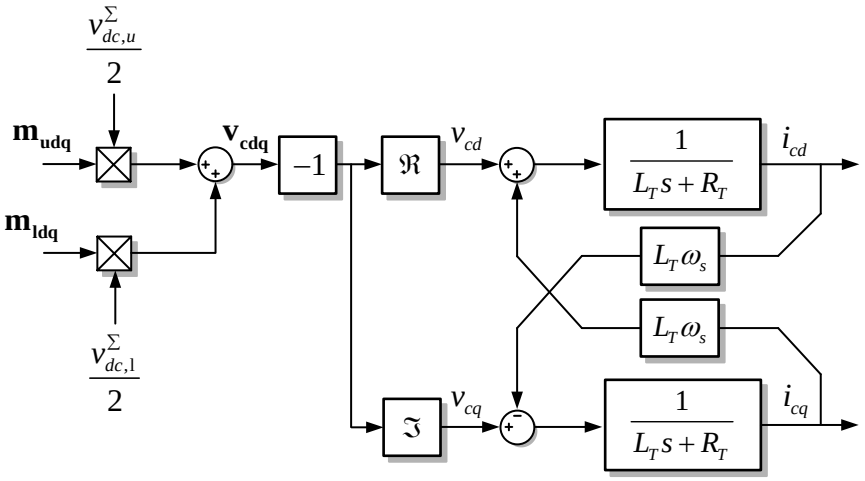

Fig. 2.9 Three-Phase circulating current model

2.2.3 Three-phase average dc voltage model

The dc voltage in each module changes according to the active power sharing between the dc source and the ac grid. Since the external dc sources are affected by a bidirectional power flow, we need to control the dc voltage variation through the correct power balance. In a three-phase system, the power balance of both arms is formulated as.

$$\begin{aligned}\frac{C_{sm}}{2N}\frac{d}{dt}\left(v_{dci}^{\Sigma}\right)^2 &= \sum_{k=1}^{N} P_{dci,k} - p_{oi} \\ &= \Delta P_i\end{aligned} \tag{2.64}$$

The previous expression is defined according to the analysis described in the single-phase configuration of equation (2.23), where the switching and conduction losses have been disregarded. The first term at the left-hand side of equation (2.64) correspond to the rate of change of energy in the dc capacitor, while P_{oi} represents the output power in the upper and lower arm. The power arms in $\alpha\beta$ frame are given by.

$$\begin{aligned}P_{ou} &= \Re\left\{\frac{3}{2}\mathbf{v}_{\mathbf{u\alpha\beta}}\mathbf{i}^{*}_{\mathbf{u\alpha\beta}}\right\} \\ P_{ol} &= \Re\left\{\frac{3}{2}\mathbf{v}_{\mathbf{u\beta}}\mathbf{i}^{*}_{\mathbf{u\alpha\beta}}\right\}\end{aligned} \tag{2.65}$$

Where the current and voltage arms are expressed in matrix form. To find the current references of the three-phase model described in previous section, the power arms are represented in terms of the dq reference frame.

$$\begin{aligned}P_{ou} &= \Re\left\{\frac{3}{2}\mathbf{v}_{\mathbf{udq}}e^{j\omega t}\mathbf{i}^{*}_{\mathbf{udq}}e^{-j\omega t}\right\} \\ P_{ol} &= \Re\left\{\frac{3}{2}\mathbf{v}_{\mathbf{ldq}}e^{j\omega t}\mathbf{i}^{*}_{\mathbf{ldq}}e^{-j\omega t}\right\}\end{aligned} \tag{2.66}$$

The previous expression can be reduced to.

$$\begin{aligned}P_{ou} &= \frac{3}{2}\left(v_{ud} + jv_{uq}\right)\left(i_{ud} - ji_{uq}\right) \\ P_{ol} &= \frac{3}{2}\left(v_{ld} + jv_{lq}\right)\left(i_{ld} - ji_{lq}\right)\end{aligned} \tag{2.67}$$

We can see that the current arms define the circulating and the output currents. According to equation (2.3), the upper and lower power arms are rewritten as.

$$\begin{aligned} P_{ou} &= \frac{3}{2}\left(v_{ud} + jv_{uq}\right)\left(i_{ud} - ji_{uq}\right) \\ &= \frac{3}{2}\left(v_{ud} + jv_{uq}\right)\left(\frac{i_{od} - ji_{oq}}{2} + i_{cd} - ji_{cq}\right) \\ &= \frac{3}{2}v_{ud}\left(\frac{i_{od}}{2} + i_{cd}\right) + \frac{3}{2}v_{uq}\left(\frac{i_{oq}}{2} + i_{cq}\right) \end{aligned} \tag{2.68}$$

$$\begin{aligned} P_{ol} &= \frac{3}{2}\left(v_{ld} + jv_{lq}\right)\left(i_{ld} - ji_{lq}\right) \\ &= \frac{3}{2}\left(v_{ld} + jv_{lq}\right)\left(-\frac{i_{od} - ji_{oq}}{2} + i_{cd} - ji_{cq}\right) \\ &= \frac{3}{2}v_{ld}\left(-\frac{i_{od}}{2} + i_{cd}\right) + \frac{3}{2}v_{lq}\left(-\frac{i_{oq}}{2} + i_{cq}\right) \end{aligned} \tag{2.69}$$

Note that the d and q components of the current and voltage variables impact in the active power. In order to define the appropriate current components, we define the total three-phase power P_T and the difference power P_Δ. As mentioned, the total power is associated to the output current and the difference power is associated to the circulating current. In a three-phase system, the total power in dq frame can be expressed as.

$$P_T = P_{ou} + P_{ol} \tag{2.70}$$

Where the upper and lower active powers are replaced by.

$$P_T = \frac{3}{2}\left[\left(v_{ud} - v_{ld}\right)\frac{i_{od}}{2} + \left(v_{ud} + v_{ld}\right)i_{cd}\right] + \frac{3}{2}\left[\left(v_{uq} - v_{lq}\right)\frac{i_{oq}}{2} + \left(v_{uq} + v_{lq}\right)i_{cq}\right] \tag{2.71}$$

The difference between the voltage arms is multiplied by the output current, while the addition is multiplied by the circulating current. Since the voltage drop in the coupling inductance can be considered significantly small compared to the voltage arms, the upper voltage is approximated to $v_{udq} \approx -v_{odq}$, meanwhile the lower voltage is approximated to $v_{ldq} \approx v_{odq}$. Therefore, the total power P_T is reduced to.

$$P_T = -\frac{3}{2}\left(v_{od}i_{od} + v_{oq}i_{oq}\right) \tag{2.72}$$

Despite possible power imbalances, previous expression shows that only the output current affects the total power, while the circulating current does not have any influence on it.

Remember that a synchronization control loop defines an appropriate phase-angle to force the voltage $v_{oq} = 0$ in the dq reference frame. Hence, the total active power is reduced to

$$P_T = -\frac{3}{2} v_{od} i_{od} \tag{2.73}$$

In a similar fashion, we determine the power difference between the upper and lower arm through the expressions described in (2.68) and (2.69) respectively, giving rise to.

$$P_\Delta = \frac{3}{2}\left[\left(v_{ud} + v_{ld}\right)\frac{i_{od}}{2} + \left(v_{ud} - v_{ld}\right) i_{cd} \right] + \frac{3}{2}\left[\left(v_{uq} + v_{lq}\right)\frac{i_{oq}}{2} + \left(v_{uq} - v_{lq}\right) i_{cq} \right] \tag{2.74}$$

Since the voltage arms were approximated to $v_{udq} \approx -v_{odq}$ and $v_{ldq} \approx v_{odq}$, the power difference is simplified to.

$$P_\Delta = -3\left(v_{od} i_{cd} + v_{oq} i_{cq}\right) \tag{2.75}$$

Note that the power difference is only driven by the circulating current. Since the voltage v_{oq} is forced to zero by the synchronization control loop, the power difference is defined by.

$$P_\Delta = -3 v_{od} i_{cd} \tag{2.76}$$

By using the power expressions introduced in (2.73) and (2.76) we can define the references for the output and circulating currents.

2.3 Summary of the chapter

While previous chapter introduces different configurations of power converters used in PV applications, we focused this chapter to introduce the single-phase and three-phase Isolated Multi-Modular Converter proposed. First, the single-phase model was studied based on the output and circulating current models and then extended to the three-phase configuration.

Two dynamic models were derived from the mathematical analysis to represent the upper and lower current arm response. Additionally, the power exchange between the dc and ac side was analyzed according to the average dc voltage model. We demonstrated that the total active power was related to the output current, while the active power difference was associated to the circulating current. This concept will be used later to define the current references in the control design.

In the three-phase system, a transformation matrix was introduced to represent the output and circulating current models in the $\alpha\beta$-frame. By introducing this matrix transformation, it is possible to define two decouple models in the three-phase configuration, similar to the one described in the single-phase IMMC.

Chapter 3.

Control of the IMMC

Previous chapter provided a mathematical analysis of the IMMC to determine its operation principle based on the output and circulating current models. In this chapter we introduce the central control used to regulate these currents and the total energy of the converter. First, an overview of the entire control is presented and then a control methodology based on the crossover frequency and phase margin technique is studied to define the optimal parameters for the internal and external control loops. Moreover, the dynamic and steady state operation of a three-phase IMMC with three modules per arm is simulated to evaluate the converter performance working in balance and imbalance conditions.

3.1 Control architecture

The configuration of the control proposed for the IMMC is illustrated in Fig. 3.1. The control architecture has a cascaded configuration for controlling: the average dc voltages, the output current and the circulating current. The input signals are the quadratic value of the total dc voltages whose role is to define the current references for the internal control loops [105]. Using a current controller, it is possible to limit the maximum current level and achieve a perfect tracking of the references.

The output of the current controllers define the general modulation indexes for the upper and lower arms. Then, the voltage balancing control loops is used to modify these signals to provide a tailored modulation index. Because modules are connected to independent dc sources, the possibility of different power level may lead to control instabilities if all modules operate with the same modulation index. Therefore, the voltage balancing control block is embedded in each module.

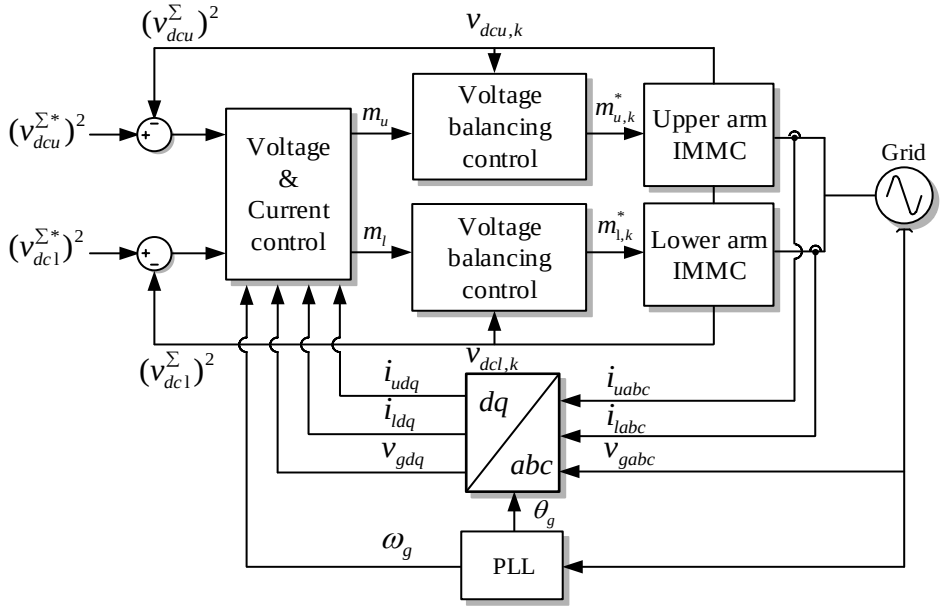

Fig. 3.1 General control structure of the IMMC

In order to synchronize the voltage and current signals with the ac grid. A synchronization control block set the grid angle. Then, the Park transformation converts the *abc* voltage and current signals into a synchronous reference frame.

The cascaded configuration of the control structure presented in Fig. 3.1 is widely used in multilevel converters connected to the ac grid. However, some differences may appear based on the requirements of each converter. In the following sections, we will describe each block based on the specifications for the IMMC.

3.2 Output and circulating current controllers

In this section the output and the circulating current controllers based on the dynamic models described in Chapter 2 are analyzed. These control loops are called inner controllers and are necessary for a perfect tracking and current limitation in the power exchange

between the dc and ac side. For a proper operation, they are adjusted as fast and accurate as possible to operate under different scenarios. The matrix transformation described in the three-phase configuration of the IMMC provides a decoupling model of the output and circulating currents, so each control system can be independently studied.

The design of the current control loops is critical for the optimal operation of the IMMC, otherwise the performance and stability of the converter may be drastically affected. Therefore, a control strategy for tuning the control parameters is also studied.

The control loops of the output and circulating current controllers are represented through the general close loop diagram illustrated in Fig. 3.2. According to the control theory, the system consists of two main components, the process G_P and the control system G_c [105]. There is a disturbance acting on the process called load disturbance *d*, which may affect the control stability of the system. The signal y is the measurement signal and the variable to be controlled. The reference r is the setpoint and its difference with the measurement signal is processed through the controller G_c to determine the actuator u.

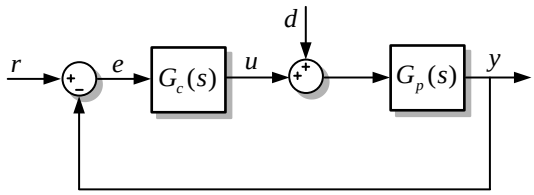

Fig. 3.2 Control structure of the output and circulating current controller

The control target of the close loop is to avoid instabilities in the system, while the process follows the reference signal. The control system should also be able to reduce the effect of load disturbances, particularly in the case of steady state operation. To comply all these requirements, we have defined two difference relationships to study how the system responds under setpoint changes and load disturbances.

The complementary sensitivity function G_{ry} described in equation (3.1) represents the relationship between the reference and the measurement signal. Therefore, it gives us the response of the process under setpoint changes.

$$G_{ry} = \frac{G_c G_p}{1 + G_c G_p} \tag{3.1}$$

Similarly, the load disturbance sensitivity function G_{dy} described in equation (3.2) evaluates the dynamic response of the output signal under load disturbances.

$$G_{dy} = \frac{G_p}{1 + G_c G_p} \tag{3.2}$$

Regardless of the numbers of phases, the controller G_c can be based on either a Proportional Integrator (PI) or a Proportional Resonant (PR) controller. The PI controller operates in a dq synchronous reference frame and it requires a phase angle to rotate the voltage and current signals. If the phase-angle matches with the grid angle, the current components will be associated to the active and reactive power as long as the grid voltage is aligned to the d or q axis. The control structure of the PI controller is presented in equation (3.3), a proportional gain K_p and an integrative gain T_i provide the required control signals to ensure zero steady state error at zero frequency component.

$$G_c(s) = K_p\left(1 + \frac{1}{T_i s}\right) = K_p \frac{T_i s + 1}{T_i s} \tag{3.3}$$

The controller G_c processes the difference between the reference and the measurement signal. But, as digital processors are used to implement the control and the modulation technique, an inherent time delay has to be considered. According to [106], [107], the computational time delay can be modeled considering half-carrier sampling time and the measurement delay, creating an overall delay T_d equal to 1.5 times the sampling time. This delay is introduced in the close loop system through the following expression.

$$G_d(s) = \frac{1}{c_{pk}} e^{-T_d s} \tag{3.4}$$

Where c_{pk} is the peak-to-peak value of the carrier waveform in the PWM modulation. Introducing the time delay in the close loop system, the control structure presented in Fig. 3.2 can be adapted to Fig. 3.3.

It only remans to find the optimal parameters of G_c. These parameters can be estimated based on the crossover frequency and phase margin technique described in the following section.

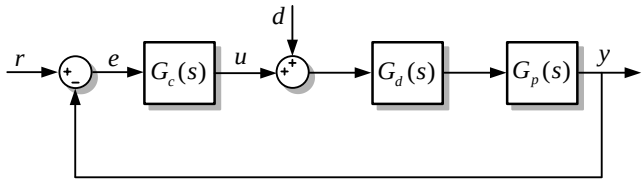

Fig. 3.3 Control structure of the output and circulating current controller considering a time delay G_d.

3.2.1 Tuning of control parameters

In the control design, it is possible to go beyond the close loop stability. In particular, we can obtain relevant information from the instability boundaries in the open loop configuration by defining a relative stability. This is achieved by introducing an open loop frequency response close to the critical stability border defined in the Nyquist method [105]. This analysis can be done through the crossover frequency and phase margin technique. Basically, the idea is to maximize the control parameters under an unity open loop gain at a specific crossover frequency ω_c.

The phase margin represents the stability and the crossover frequency the bandwidth of the controller. Since, an unity open-loop gain is expected, the open loop G_{OL} can be expressed as follows.

$$G_{OL}\left(j\omega_c\right) = 1\angle -\pi + \phi_m \tag{3.5}$$

To achieve an acceptable damped response, the phase margin value is usually set between 40º to 70º [105]. Considering an unitary open loop gain and a phase margin between the mentioned range, the control parameters are estimated by.

$$\left|G_{OL}\left(j\omega_c\right)\right| = 1 \tag{3.6}$$

$$\angle G_{OL}\left(j\omega_c\right) = -\pi + \phi_m \tag{3.7}$$

Where the open-loop angle $\angle G_{OL}\left(j\omega_c\right)$ is reduced to.

$$\angle G_{OL}\left(j\omega_c\right) = tg^{-1}\left(\frac{\Im\left\{G_{OL}\left(j\omega_c\right)\right\}}{\Re\left\{G_{OL}\left(j\omega_c\right)\right\}}\right) \tag{3.8}$$

To ensure a close-loop stability in a wide range of frequencies, the crossover frequency is selected to be larger than the ac grid frequency and smaller than the switching frequency. According to [108], the crossover frequency can be set around twenty and ten times smaller than the switching frequency.

3.2.2 Design of output current control

In previous chapter it was identified the relationship between the output current and the voltage arms. Now, in order to control this current, we introduce a current controller to achieve zero steady-state error, this is easily done using the close loop diagram presented in Fig. 3.3. The dynamic model of the output current in equation (2.60) has been rewritten in

equation (3.9), however the matrix notation is omitted as it is understood that the subscript *dq* represent the *d* and *q* components. Note that the cross coupling components between the *dq* axes have been disregarded as they are compensated in the control loop.

$$\frac{R_T}{2} i_{odq} + \frac{L_T}{2} \frac{d}{dt} i_{odq} = v_{sdq} - v_{odq} \tag{3.9}$$

The connection between the converter and the grid can be represented through the output current model shown in Fig. 3.4. In this sense, the output voltage v_o is defined as a controlled voltage source connected to the grid voltage v_g through an impedance Z_g, which represents the equivalent impedance given by the ac filter, transformer and cables. Note that a common mode voltage v_N is defined between the common point of the converter and the grid to represent a possible fault operation or third harmonic compensation.

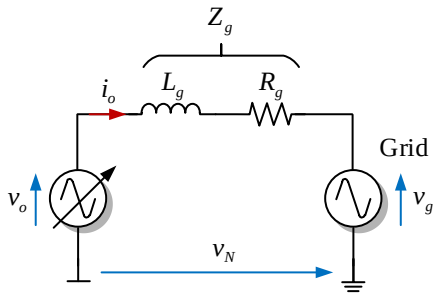

Fig. 3.4 Simplified output current model

The grid voltage represents the measurement voltage at the point of common coupling (PCC). Introducing the grid impedance and the common mode voltage in (3.9), the output current model can be rewritten as.

$$\left(\frac{R_T}{2} + R_g\right) i_{odq} + \left(\frac{L_T}{2} + L_g\right) \frac{d}{dt} i_{odq} = v_{sdq} - v_{gdq} - v_N \tag{3.10}$$

The dynamic response is defined based on the arm and grid impedance. In Laplace domain, the current model is defined by equation (3.11), where the equivalent inductance and resistance are simplified by L_{Tg} and R_{Tg}.

$$\begin{aligned} G_p(s) &= \frac{1}{\left(\frac{L_T}{2} + L_g\right) s + \left(\frac{R_T}{2} + R_g\right)} \\ &= \frac{1}{L_{Tg} s + R_{Tg}} \end{aligned} \tag{3.11}$$

The output current model has a first order transfer function with a constant time response equal to L_{Tg} / R_{Tg}. As v_{sdq} represents the voltage difference between the upper and lower arms, any voltage deviation will change the output current with a dynamic response given by L_{Tg} / R_{Tg}. However, when a PI controller is introduced, the dynamic response is settled by the control parameters and the plant.

In this analysis, the sensitivity functions described in previous section evaluate the dynamic response of the close-loop system. Thus, replacing the plant and the PI controller in equations (3.1) and (3.2) respectively, the complementary and the load disturbance sensitive functions are reduced to.

$$G_{ry} = \frac{\frac{K_p}{L_{Tg}}\left(s + \frac{1}{T_i}\right)}{s^2 + \frac{R_{Tg} + K_p}{L_{Tg}} s + \frac{K_p}{L_{Tg}} \frac{1}{T_i}} \tag{3.12}$$

$$G_{dy} = \frac{\frac{s}{L_{Tg}}}{s^2 + \frac{R_{Tg} + K_p}{L_{Tg}} s + \frac{K_p}{L_{Tg}} \frac{1}{T_i}} \tag{3.13}$$

The simulation setup considers a three-phase IMMC with three modules per arm. The converter has a nominal power of 6MW connected to an electrical grid of 32 kV/50 Hz. In order to determine the proportional and integrative gains, simulation parameters are illustrated in Table 3.1.

Table 3.1. Parameters of simulation setup

Parameters	**Symbol**	**Value**
Nominal power	P_T	6 MW
Grid voltage (rms)	v_g	32 kV
Grid frequency	f_s	50 Hz
Number of modules per arm	N	3
Switching frequency	f_c	2500 Hz
Equivalent transformer resistance	R_T	1.05 Ω
Equivalent transformer inductance	L_T	7.6 mH

The grid impedance is defined based on the short-circuit-ratio (SCR), which represents the relationship between the short circuit power at the point of common coupling and the

converter power [109]. In the control design, it is considered a stiff grid (SCR = 20), giving rise to a small grid impedance.

For tuning the controller parameters, the crossover frequency is set 15 times smaller than the switching frequency while the phase margin is evaluated under three different values. In Fig. 3.5 and Fig. 3.6 the complementary and load disturbance sensitivity functions are observed under a step response with a phase margin equal to 40º, 50º and 60º respectively.

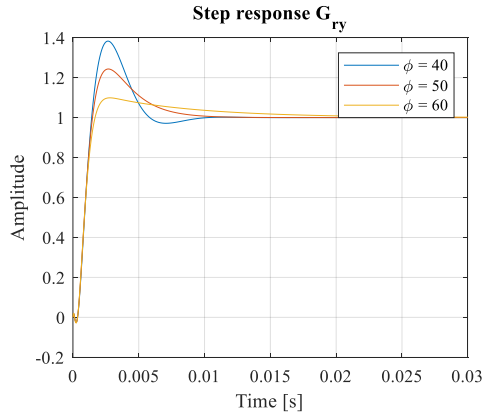

Fig. 3.5 Step response of complementary sensitivity function in output current controller

Note how the step response has a higher overshoot as the phase margin decreases. A similar result is observed in the load disturbance sensitive function of Fig. 3.6, where the highest undershoot is observed with the smallest phase margin. We can conclude that a phase margin equal to 50º represents a reasonable step response in the complementary and load disturbance sensitivity functions. Thus, for the output current controller, it is defined a phase margin of 50º.

In Fig. 3.7 the bode diagram of the open loop transfer function shows how the magnitude crosses zero with a phase margin of 50º at 1047 rad/s, while the gain margin is 11.5 dB at 3740 rad/s.

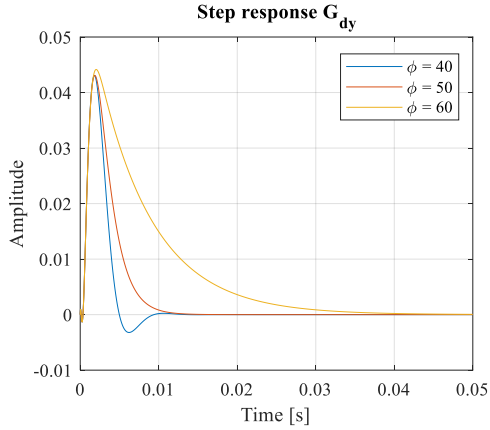

Fig. 3.6 Step response of load disturbance sensitivity function in output current controller

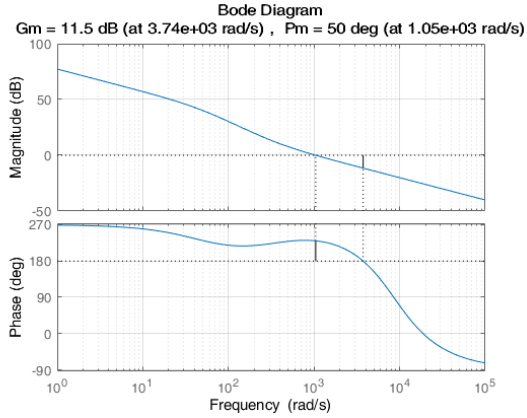

Fig. 3.7 Bode diagram of open loop in output current controller

Based on the bode diagram shown in Fig. 3.7, the proportional and integrative gain parameters of the PI controller for the output current control loop are shown in Table 3.2.

Table 3.2 Control parameters of output current controller

Parameters	**Symbol**	**Value**
Proportional gain	k_{pio}	24.97
Integrative gain	k_{iio}	3968
Phase margin	ϕ_m	50°
Cross-over frequency	ω_c	1047 rad/s

3.2.3 Design of circulating current control

Following the same analysis introduced in previous section to define the control parameters of the output current, the circulating current controller is based on a PI configuration to ensure zero steady state error. According to Chapter 2, the circulating current depends on the total voltage arm and the coupling inductance. Simplifying the matrix notation of the model described in equation (2.61), the circulating current model is rewritten in equation (3.14). Once again the cross coupling components have been disregarded as they are compensated in the control loops.

$$R_T i_{cdq} + L_T \frac{d}{dt} i_{cdq} = v_{cdq} \tag{3.14}$$

Previous equation can be represented based on the electrical circuit illustrated in Fig. 3.8, where the voltage arms regulate the circulating current flowing through the coupling inductance.

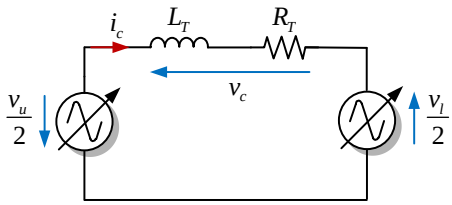

Fig. 3.8 Simplified circulating current model

Using the Laplace transform, the circulating current model described in (3.14) can be represented as follows.

$$G_p(s) = \frac{1}{L_T s + R_T} \tag{3.15}$$

Similar to the output current model, the circulating current has a first order transfer function with a constant time response of L_T / R_T. However, on this occasion, the grid impedance does not have any effect on the current. For tuning the control parameters, a similar bandwidth to the one used in the output current is considered. Therefore, the crossover frequency is set 15 times smaller than the switching frequency and the phase margin is set at 50º. Because the grid impedance has a small effect on the output current design, the complementary and load disturbance sensitive functions are not analyzed. The bode diagram of the circulating current response is shown in Fig. 3.9.

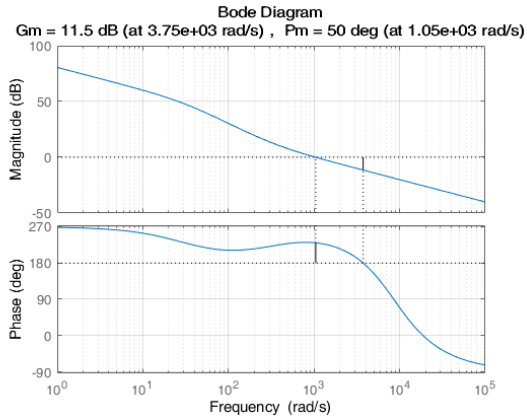

Fig. 3.9 Bode diagram of open loop in circulating current controller

As seen in Fig. 3.9, the open loop magnitude decreases as the frequency increases. The zero-crossing point happens at 1047 rad/s with a phase margin of 50º, complying with the control requirements. Additionally, the zero-phase margin happens at 3750 rad/s with an open loop magnitude equal to 11.5 dB. The circulating current parameters are shown in Table 3.3.

Table 3.3 Control parameters of circulating current controller

Parameters	**Symbol**	**Value**
Proportional gain	k_{pic}	20.22
Integrative gain	k_{iic}	6768
Phase margin	ϕ_m	50º
Cross-over frequency	ω_c	1047 rad/s

3.2.4 Output and circulating current control architecture

Current controllers are required to generate the voltage difference v_s and the drop voltage v_c. The configuration used in both control loops are illustrated in Fig. 3.10 and Fig. 3.11 respectively. They are formed by two PI controllers with a current coupling between the axis. So, the cross coupling given by the synchronous rotation in the *dq* reference frame is removed. The *d* axis compensator processes the *d* error and provides the voltage difference v_{sd} and the drop voltage v_{cd}. Similarly, the *q* axis compensator processes the *q* error and provides the voltages v_{sq} and v_{cq}. Then, both components are used to define the

average modulation indexes in the upper and lower arms. According to previous chapter, the average modulation indexes are reduced to.

$$\mathbf{m}^*_{\mathbf{udq}} = \frac{1}{v^*_{dc,u}}\left(-\mathbf{v}^*_{\mathbf{sdq}} - \mathbf{v}^*_{\mathbf{cdq}}\right)$$
$$\mathbf{m}^*_{\mathbf{ldq}} = \frac{1}{v^*_{dc,l}}\left(\mathbf{v}^*_{\mathbf{sdq}} - \mathbf{v}^*_{\mathbf{cdq}}\right) \tag{3.16}$$

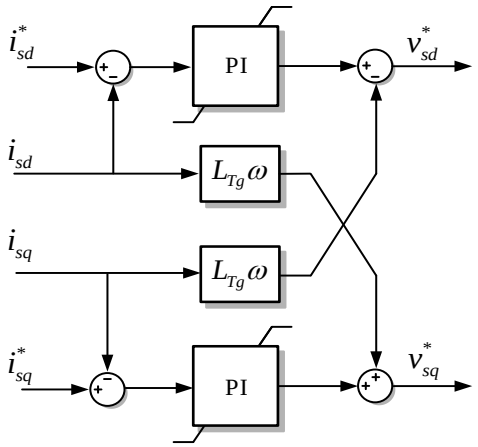

Fig. 3.10 Output current control based on PI controllers

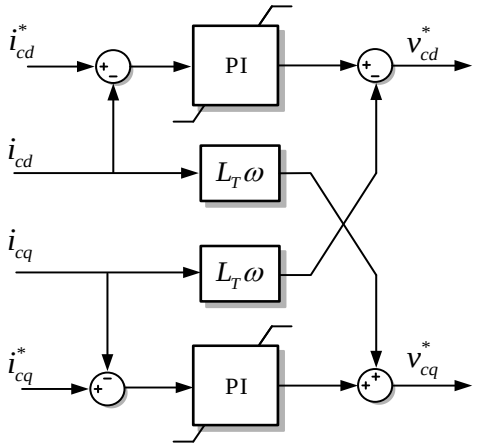

Fig. 3.11 Circulating current control based on PI controllers

Where voltage $\mathbf{v}^*_{\mathbf{sdq}}$ and $\mathbf{v}^*_{\mathbf{cdq}}$ are the vectors given by the output and circulating current controllers, while $v^*_{dc,u}$ and $v^*_{dc,l}$ are the total dc voltages in the upper and lower arms. Additionally, the modulation indexes are represented according to their *dq* components as:

$$\mathbf{m}^{*}_{\mathbf{udq}} = \begin{bmatrix} m^{*}_{ud} \\ m^{*}_{uq} \end{bmatrix} \qquad \mathbf{m}^{*}_{\mathbf{ldq}} = \begin{bmatrix} m^{*}_{ld} \\ m^{*}_{lq} \end{bmatrix} \tag{3.17}$$

For a proper converter operation, there is an important aspect to be considered. A current saturation is required to avoid high currents and power levels out of range. However, a common consequence of the saturation limit is that the integrator controller will continue to integrate while the input is limited. This means that the state of the integrator can reach high values, leading to poor transient responses. For this reason, an anti-windup scheme is required to make sure that the state of the controller is driven by the actual input. In Fig. 3.12, it is illustrated a PI controller with anti-windup. Note that if the output *u* (the actuator) is saturated, the input of the integrator is forced to zero, avoiding an increase in the cumulative state.

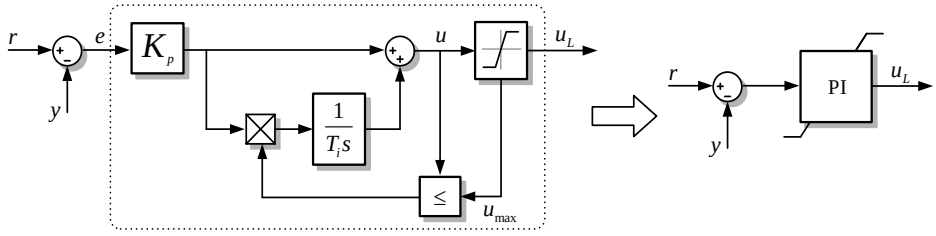

Fig. 3.12 PI control with anti-windup

Denoting u_L as the desired actuator of the PI controller, the saturation limit with anti-windup can be described as follows.

$$u_L = \begin{cases} u_{\max} & \text{if} \quad u(t) > u_{\max} \\ u(t) & \text{if} \quad u_{\min} < u(t) < u_{\max} \\ u_{\min} & \text{if} \quad u(t) < u_{\min} \end{cases} \tag{3.18}$$

Voltage $u_{\max}$ and $u_{\min}$ represent the boundary conditions of the control operation, so any voltage beyond these levels will force the output of the comparator to zero. Therefore, the input of the integrator will be forced to zero as well. By doing this, the integrator will provide the last value set before the actuator *u* is saturated. When the actuator operates between its maximum and minimum levels, the output of the comparator is one and the integrator operates in normal condition.

3.3 Third harmonic compensation

As we defined in section 3.2, the common-mode voltage v_N can be used to extend the operating range of the converter by injecting a third-harmonic component.

The average modulation index is a function of time that can be affected by unpredictable transient conditions. If these conditions surpass the converter boundaries, the modulated voltage may operate in overmodulation, thus distorting the output voltage. However, injecting a third harmonic component, it is possible to extend the maximum operating range. Introducing this concept, the modulation index is represented as follows.

$$\begin{aligned} m_{i,a} &= \hat{m}_i \cos(\omega t) - \frac{1}{6}\hat{m}\cos(3\omega t) \\ m_{i,b} &= \hat{m}_i \cos(\omega t - \frac{2\pi}{3}) - \frac{1}{6}\hat{m}\cos(3\omega t) \\ m_{i,c} &= \hat{m}_i \cos(\omega t + \frac{2\pi}{3}) - \frac{1}{6}\hat{m}\cos(3\omega t) \end{aligned} \tag{3.19}$$

The third-harmonic injection extends the operating range of the converter in 15% [102]. This scenario can also be reached by decreasing the range of the ac side or increasing the equivalent dc voltage level.

The implementation of the third harmonic injection can be performed using the min-max zero sequence compensation technique [110], which adjusts the amplitude of the modulation index by adding the maximum and minimum instantaneous ac voltage level. The min-max zero sequence compensation is given by.

$$v_N = \frac{\min\left\{v_{sa}^*.v_{sb}^*, v_{sc}^*\right\}}{2} + \frac{\max\left\{v_{sa}^*.v_{sb}^*, v_{sc}^*\right\}}{2} \tag{3.20}$$

3.4 Average DC voltage controllers

So far, we have studied the output and circulating current controllers for setting the average modulation index in the upper and lower arms. While the output current regulates the voltage difference v_s, the circulating current controls the drop voltage v_c. Now, in order to define the current references, we are going to take a look at the outer controllers to regulate the total and the difference active power through power in the upper and lower arms.

According to (2.72), the total active power represents the addition of the upper and lower power arms, and it defines the *d* component of the output current reference. Similarly,

equation (2.75) defines the *d* component of the circulating current through the power difference between both arms.

The relationship between the active power and the dc voltage was described in previous chapter. The analysis demonstrated that the rate of change of energy in the dc capacitor defines the power difference between the dc and ac side. Considering the dc power as a perturbation to the system, the relationship between the output power and the dc voltage is given by.

$$P_{oi} = -\frac{C_{sm}}{2N}\frac{d}{dt}\left(v_{dci}^{\Sigma}\right)^2 \tag{3.21}$$

Where C_{sm} is the dc capacitor and N is the number of modules per arm. The objective of this control loop is to regulate the total voltage v_{dci}^{Σ}. Therefore, any voltage difference in the series connection of modules is not observed. This is not the most realistic scenario, as all modules can operate at different voltage levels. However, this controller is focused on regulating the total power per arm and not the power of each module. In next chapter a local control strategy embedded in each module is proposed to withstand different power imbalances.

Using the Laplace transform in equation (3.21), the plant between the output power and the total dc voltage is given by.

$$\left(v_{dci}^{\Sigma}\right)^2 = -\frac{2N}{C_{sm}}\frac{1}{s}P_{oi}(s) \tag{3.22}$$

Where $(v_{dci}^{\Sigma})^2$ is the output signal and P_{oi} is the input. Remember that the total and the difference power between the arms defines the *d* component of the output and circulating currents. Considering the plant model described in (3.22) and the current expression given by (2.73) and (2.76), the block diagram of the average dc voltage control loop is represented in Fig. 3.13.

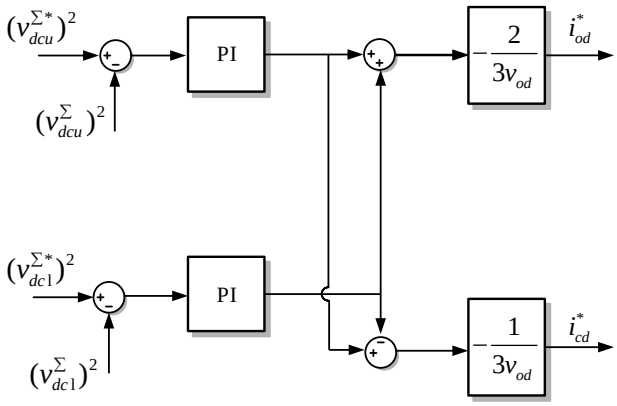

Fig. 3.13 Average dc voltage control loop

As illustrated in Fig. 3.13, the square value of the voltage reference in the upper and lower arms are compared to the square value of the voltage measurements. The error is processed by two PI controllers which define the active powers. Then, these components are added and subtracted to generate the total and the difference power whose purpose is to define later the current references. Note that PI controllers are implemented to compensate the dc voltages as they ensure zero steady state error.

Similar to the current control design, the PI parameters are defined based on the crossover frequency and phase margin technique. On this occasion, the phase margin is set at 60º and the crossover frequency is set 15 times smaller than the current controller, thus a coupling between both control loops is avoided. The bode diagram of the average dc voltage open-loop is shown in Fig. 3.14.

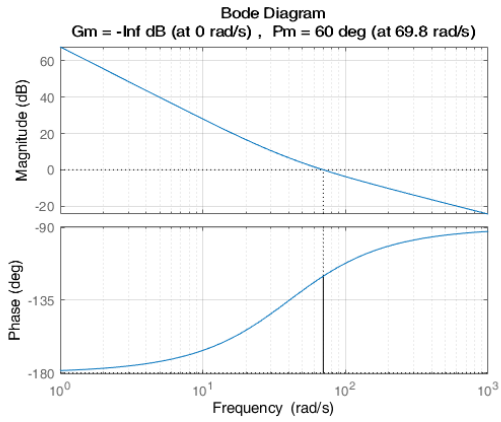

Fig. 3.14 Bode diagram of open loop in average dc voltage controller

We can see that the phase margin of 60º is achieved at 69.8 rad/s. In order to analyze the dynamic response of the close loop system, the complementary and load disturbance sensitivity functions described in (3.1) and (3.2) are evaluated with the control parameters depicted in Table 3.4.

In Fig. 3.16 and Fig. 3.17, the complementary and load disturbance sensitivity functions show a step response with a dynamic behavior according to the control parameters described in Table 3.4. The overshoot in the complementary sensitivity function is around 1.12 with a settle time of 120ms.

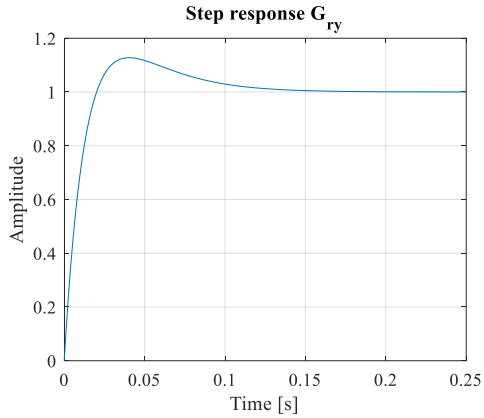

Fig. 3.15 Step response of complementary sensitivity function in the average dc voltage controller

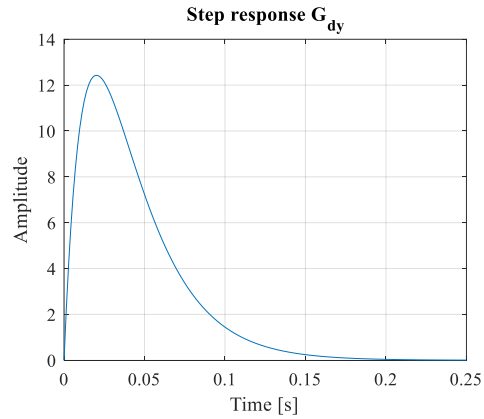

Fig. 3.16 Step response of load disturbance sensitivity function in the average dc voltage controller

Table 3.4 Control parameters of average dc voltage controller

Parameters	Symbol	Value
Proportional gain	k_{pvdc}	0.035
Integrative gain	k_{ivdc}	1.72
Phase margin	ϕ_m	50º
Cross-over frequency	ω_c	69.8 rad/s

3.5 Synchronization control loop

As current controllers operate in a synchronous reference frame, a phase angle is required to synchronize the voltage and current signals with the ac grid. Typically, grid synchronization techniques are based on time-domain methods which calculate the phase angle or the grid frequency. The phase angle strategy also known as phase-locked loop (PLL) [111] is used in several applications and it consists of a close-loop system with an internal oscillator to synchronize the output signal with the input signal by shifting the frequency. The basic structure of the PLL is analyzed in [111], where a phase detector set a signal proportional to the phase difference between the input and the output signal. Then, a low-pass filter is implemented to attenuate high frequency components, and finally a voltage controller oscillator (VCO) generates the output signal.

The phase detector requires a quadrature signal generator (QSG), which provides two quadrature signals without introducing delays. For single-phase configurations, the phase detector is commonly provided by a transport delay whose value is set to ¼ cycle of the fundamental frequency and then a Park transformation [112] is required to calculate the direct and quadrature signals. Since the transport delay operates at the fundamental frequency, if the grid frequency changes, the output of the QSG will not generate perfect orthogonal signals, giving rise to errors in the PLL synchronization. For this reason, other PLL strategies based on the Hilbert transform, the Inverse Park transform and adaptive filters [112] have been proposed to solve this problem. The PLL based on adaptive filters provides the ability to adjust its own parameters automatically [113], removing the requirement to know information about the input signal in advance.

The second-order-generalized integrator quadrature signal generator (SOGI-QSG) is an adapter filter, whose bandwidth is not a function of the fundamental frequency. Therefore, it is suitable for variable frequency applications. The SOGI-QSG in combination with the Park transformation are used as a phase detector in the PLL to create the SOGI-PLL.

According to [112], this control strategy has a double feedback loop which provides the phase-angle to the Park transformation and the central frequency to the SOGI.

In a three-phase configuration, the Clark transform can replace the SOGI-QSG to generate the quadrature signals and then the Park transformation is used as a phase detector. Fig. 3.17 shows the synchronization control loop for a three-phases system. This configuration is also known as Synchronous-Reference-Frame PLL (SRF-PLL).

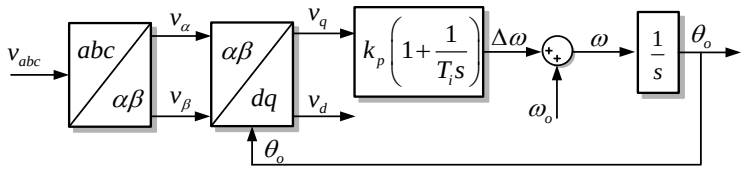

Fig. 3.17 Synchronous-Reference-Frame PLL

In the SRF-PLL a PI controller processes the voltage v_q to define the frequency deviation, which is added to the nominal frequency to generate the instantaneous synchronous frequency. Then, this signal is integrated to set the angle required to rotate the quadrature components in the Park transformation.

According to [112], when the grid voltage is not affected by harmonic components, a high bandwidth in the close loop system yields a fast and precise detection of the phase angle. However, when harmonic components are presented in the grid voltage, a small error in the instantaneous position of the input voltage vector appear and consequently v_q may be different from zero. This is the reason why, a slight reduction on the bandwidth may improve the close loop response, rejecting the effect of harmonic components in the output signal. The strategy to define the control parameters of the SRF-PLL are described in [114]. Note that the grid synchronization in the control proposed is based on the SRF-PLL.

3.6 General control architecture

In previous sections it was described how the cascaded control structure formed by the square value of the average dc voltage and the internal current controllers set the average modulation indexes for the upper and lower arms. Additionally, in order to inject the correct active and reactive current into the grid, a synchronization technique was also analyzed. The synchronous angle θ_g provided by the SRF-PLL is used in the Park transformation to rotate the voltage and current components into a *dq* reference frame. As these control loops regulate the power of the entire arm, the cascaded configuration is called central control.

To describe the complete control architecture of the IMMC, the central controller is illustrated in Fig. 3.18. The dc voltage in the upper and lower arms define the total and the difference active power which are adapted through equations (2.73) and (2.76) to define the *d* components of the output and circulating current references. The measured current arms are transformed into the output and circulating currents through the matrix transformation T_{IMMC}, and then they are rotated to a synchronous reference frame through the Park transformation. The difference between the reference and the measured currents are processed through two current control loops based on PI controllers. Consequently, the output voltages are rotated to the stationary reference frame and then adjusted to define the voltage arms through the inverse matrix transformation T_{IMMC}^{-1}.

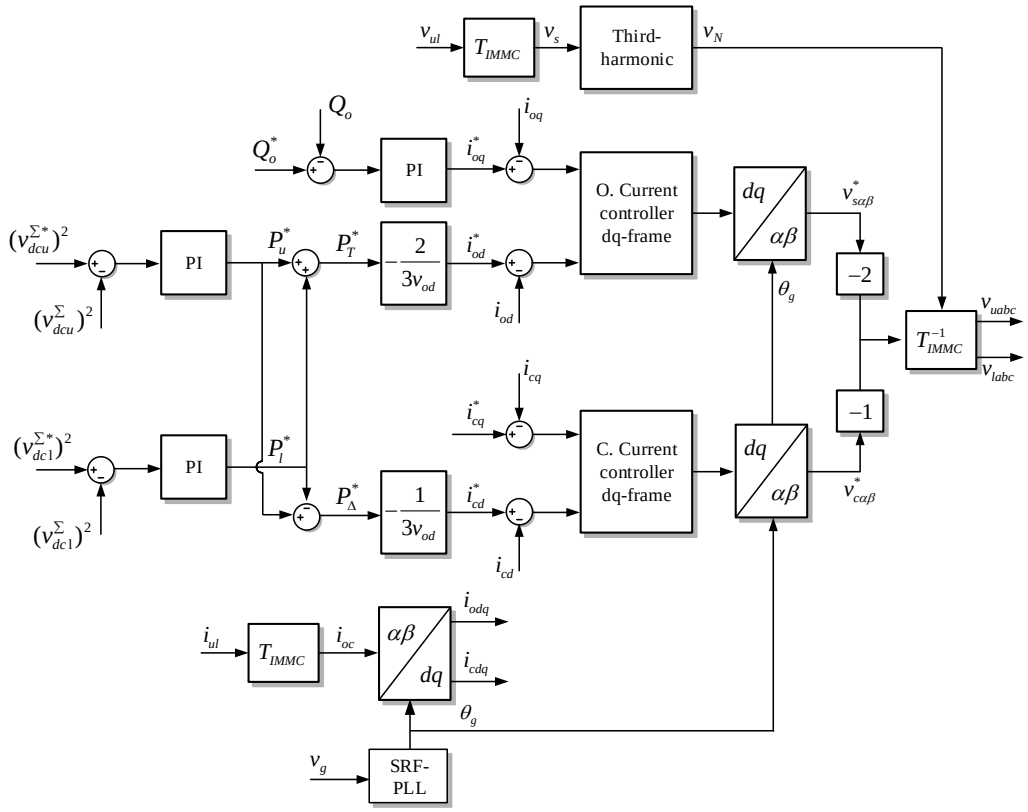

Fig. 3.18 Central control architecture of the IMMC

As described in previous chapter, the relationship between the voltage difference $v_{s\alpha\beta}$ and the drop voltage $v_{c\alpha\beta}$ are related to the voltages $v_{\Delta\alpha\beta 0}$ and $v_{\Sigma\alpha\beta 0}$ by.

$$\begin{bmatrix} 2\mathbf{v}_{\mathbf{s\alpha\beta 0}} \\ \mathbf{v}_{\mathbf{c\alpha\beta}} \end{bmatrix} = -\begin{bmatrix} \mathbf{v}_{\mathbf{\Delta\alpha\beta}0} \\ \dfrac{\mathbf{v}_{\mathbf{\Sigma\alpha\beta}0}}{2} \end{bmatrix} \tag{3.23}$$

Introducing the inverse matrix transformation, the upper and lower voltage arms are defined as follows.

$$\begin{bmatrix} \mathbf{v}_{\mathbf{u}} \\ \mathbf{v}_{\mathbf{l}} \end{bmatrix} = T_{IMMC}^{-1} \begin{bmatrix} \mathbf{v}_{\Delta\mathbf{\alpha\beta}0} \\ \dfrac{\mathbf{v}_{\sum\mathbf{\alpha\beta}0}}{2} \end{bmatrix} \tag{3.24}$$

Note that a third harmonic injection based on the min-max zero sequence compensation has been added in the voltage difference $v_{s\alpha\beta}^{*}$ to increase 15% the operating range of the converter. Therefore, voltages $v_{\Delta\alpha\beta 0}$ and $v_{\Sigma\alpha\beta 0}$ yields.

$$\left[\mathbf{v}_{\mathbf{\Delta\alpha\beta 0}}\right] = \begin{bmatrix} v_{\Delta\alpha} \\ v_{\Delta\beta} \\ v_{N} \end{bmatrix}, \qquad \left[\mathbf{v}_{\mathbf{\Sigma\alpha\beta 0}}\right] = \begin{bmatrix} v_{\Sigma\alpha} \\ v_{\Sigma\beta} \\ 0 \end{bmatrix} \tag{3.25}$$

In order to control the reactive power delivered to the grid, a power control loop set the q component of the output current reference according to a certain reference level. This controller is based on a PI configuration to ensure zero error in steady state operation.

Remember that the purpose of the circulating current reference is to define the power difference inside the converter. While the *d* component is commanded by the active power difference, the *q* component has not been defined yet. In this chapter we define $i_{cq} = 0$, however in the next chapter we will harness this component to balance the series connection of modules in one arm by shifting the output voltage.

3.7 Simulation results

Using the approach discussed in Chapter 2 and the control proposed in previous sections, the three-phase IMMC was simulated based on the configuration illustrated in Fig. 3.19. The simulation cases were chosen based on a 6 MW power converter with 3 modules per arm. Therefore, each module was capable of providing up to 1 MW. An equivalent PV panel represents the series and parallel connection of several strings to reach the voltage and current level required to generate 1 MW. In order to study the effect of the circulating current, different power levels were set in all modules of one arm at the same time. Even though, this is not the most realistic case, as each module is able to generate different power levels, this scenario allowed us to validate the inner current and the average dc voltage controller previously described. The effect of different power levels introduced between modules of the same arm and the mathematical analysis to describe the voltage control required to allow this scenario are covered in detail in next chapter.

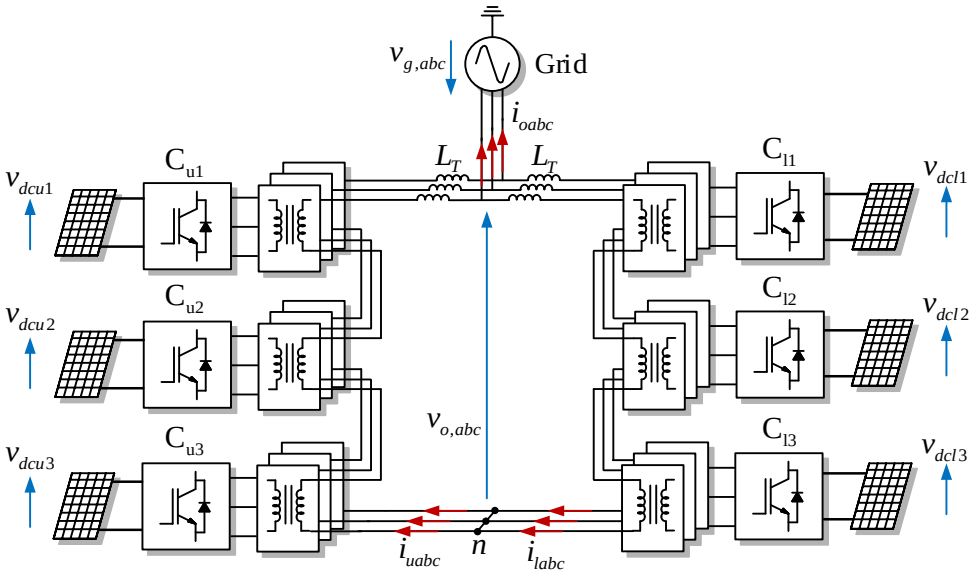

Fig. 3.19 Simulation setup of the three-phase IMMC

Each module is formed by a two-level voltage source converter (2L-VSC). The ac side is connected to an isolated transformer and the dc side is connected to a PV string. Fig. 3.19 illustrates the three-phase simulation setup used in the following study cases. The parallel connection between the upper and the lower arms generates the ac voltage $v_{o,abc}$, which

represents the total voltage given by the series connection of modules. The voltages $v_{dcu,i}$ and $v_{dcl,i}$ are the dc voltages measured in the PV terminals and the variables i_{uabc} and i_{labc} are the current arms flowing through the converter.

The control algorithm used in the study cases is shown in Fig. 3.20. In the central control, the outer controllers regulate the square value of the total dc voltages and the reactive power, while the inner controllers regulate the output and circulating currents. Note that the voltage balancing control block embedded in each module is not considered in this analysis as we do not balance the energy difference between modules of the same arm. The current arms are required to set the output and circulating currents, while the dc voltages are required to define the active power references. It is important to mention that due to the control requirements and boundary conditions, the modulation indexes are equally distributed in all modules of the upper and lower arms.

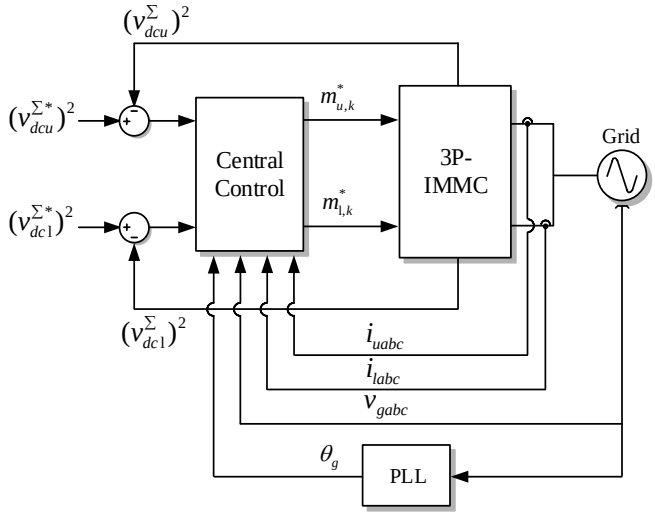

Fig. 3.20 Control configuration used in simulation results

The equivalent PV strings operate at 700V when providing the maximum power level, and at 820V in open-voltage operation. The low frequency transformers step-up the ac voltage and connect the secondary side to a medium voltage collector. As the voltage and frequency stability analysis are out of scope in this work, we considered a stiff grid with a line-to-line voltage equal to 13.5 kV - 50Hz. The rest of parameters are described in Table 3.5.

Table 3.5. Parameters of simulation setup

Parameters	Symbol	Value
Grid and converter parameters		
Nominal power	P_T	6 MW
Nominal power per module	P_M	1 MW
Grid voltage	v_g	13.5 kV
Grid frequency	f_s	50 Hz
Number of modules per arm	N	3
dc-link capacitor	C_{sm}	4.7 mF
Switching frequency	f_c	2500 Hz
Transformer parameters		
Transformer power	S_T	1 MW
Transformer ratio	r_t	1:12
Total winding inductance	L_T	7.6 mH
PV panel parameters		
Voltage in open-circuit operation	V_{OC}	820V
Voltage in maximum power operation	V_{MPP}	700V
Current in maximum power operation	I_{MPP}	1.44kA
Short circuit current	I_{SC}	1.58kA
Base parameter for pu transformation		
Power	S_B	6 MW
AC voltage	v_B	13.5 kV
DC voltage	v_{dcB}	700 V

The two study cases were evaluated in imbalance operation as a consequence of power changes in the primary sources. These scenarios were defined by different weather conditions associated to irradiation and temperature changes. In order to understand how the power provided by the PV panels was affected, in Fig. 3.21 is shown two simulation results where the active power changed under different dc voltage levels. In the first case, we appreciate how the active power behaved when the temperature increased from 5ºC to 45ªC. For instance, the yellow signal represents the power response at 25ºC. In this curve, we can see how a voltage increase resulted in a power increase as well, reaching the maximum power level at 1 pu. However, a severe power decrease happened when the voltage exceed its nominal value, returning the power to zero at open-circuit level. A similar behavior was observed with lower and higher temperature levels. Note that the blue signal

represents the power response at 45ºC, while the orange signal represents the power behavior at 5ºC.

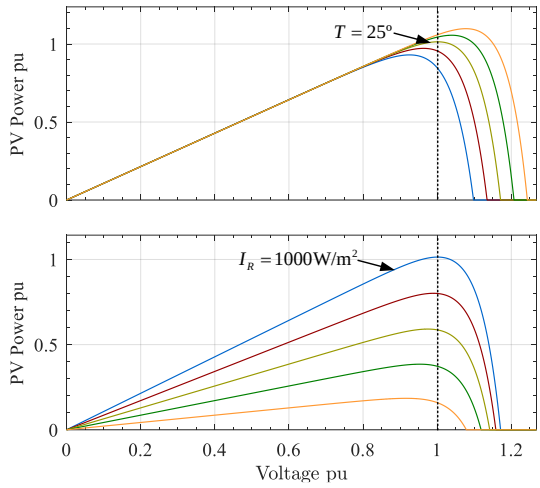

Fig. 3.21 Active power response under different temperature and irradiation conditions.

The second simulation result of Fig. 3.21 shows the power response under different irradiation conditions. Five irradiation steps of 200 W/m2 were studied. We can see that the maximum irradiation level generates the maximum power in the PV panels. An important aspect to be considered is the fact that, regardless of the irradiation level, the maximum power was reached at the same voltage (1pu). Unlike temperature changes where the dc voltage required to generate the maximum power was associated to the temperature level.

The first study case contemplates an irradiation step in the upper and lower arms. Therefore, it is studied how the converter and its control algorithm are able to deal under power imbalances with similar dc voltages. In the second study case, a voltage step was forced to emulate a temperature change. Since, temperature changes do not generate large voltage variations at the maximum power operation, a voltage step is set to provide a critical scenario. The two study cases are described in next section.

3.7.1 Study case I: Irradiation step in upper and lower arms

In the first study case, the equivalent PV panels were affected by irradiation steps to generate an imbalance operation between the upper and lower arms. The first irradiation step of 400 W/m2 was introduced at the same time in all modules of the upper arm, giving rise to a power decrease and at the same time an increase of the circulating current. Then, to compensate such power imbalance, a similar irradiation step was introduced in all modules of the lower arm. Fig. 3.22 to Fig. 3.24 show the current and voltages signals during both events. It is important to point out that all results are studied in per unit based on the parameters described in Table 3.5.

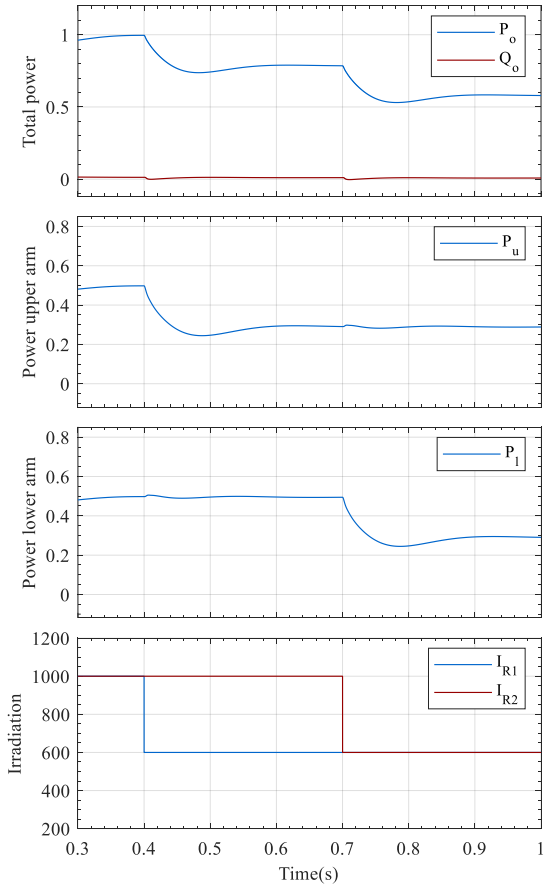

Fig. 3.22 Simulation results of total power delivered into the grid, average power produced by the upper and lower arms, irradiation steps in the equivalent PV modules.

The proposed scenario started with all modules operating at their maximum power point. Therefore, the average active power generated in the upper and lower arm was 0.5 pu. Note that the total active power delivered into the grid was equal to 1 pu while no reactive power was set.

According to Fig. 3.21, the maximum power was achieved when the voltage in the PV panels was 1 pu. Because all modules were connected to PV panels with equal characteristics, both arms produced the same power level. This balance state is also observed in the current signals. In the first 0.1 second of Fig. 3.24 the current arms had the same amplitude but shifted 180º. As a result, no circulating current appeared.

Event 1 – Irradiation step in modules of upper arm. At t = 0.4s, the irradiation level I_{r1} in all modules of the upper arm was reduced from 1000 W/m2 to 600 W/m2. Therefore, the average active power produced by the upper arm decreased to 0.3 pu, while modules in the lower arm maintained their maximum power at 0.5 pu. This power difference reduced the total power to 0.8 pu.

The power change created a perturbation in the dc voltages of all modules of the upper arm. However, they returned to their reference value to generate the maximum power again as seen in Fig. 3.23

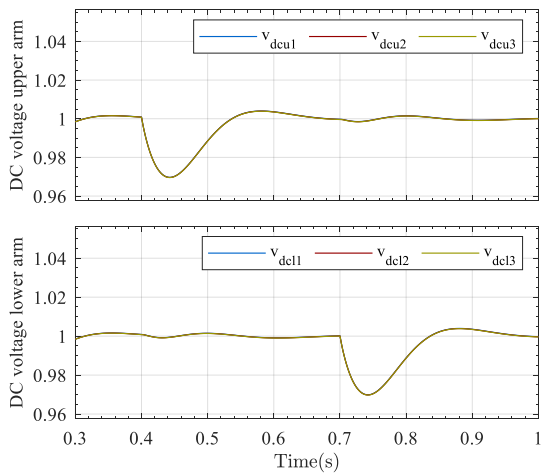

Fig. 3.23 DC voltage response in modules of the upper and lower arm under irradiation steps

As discussed before, the power imbalance generated different current levels in the arms and as a consequence, a circulating current emerged. Fig. 3.24 shows the time when the current in the upper arm decreased while the circulating current increased. Note that the

dynamic response of these currents is tied to the dynamic response of the dc voltage controllers. In the case of the output current, we can appreciate a decrease of its amplitude due to this power reduction.

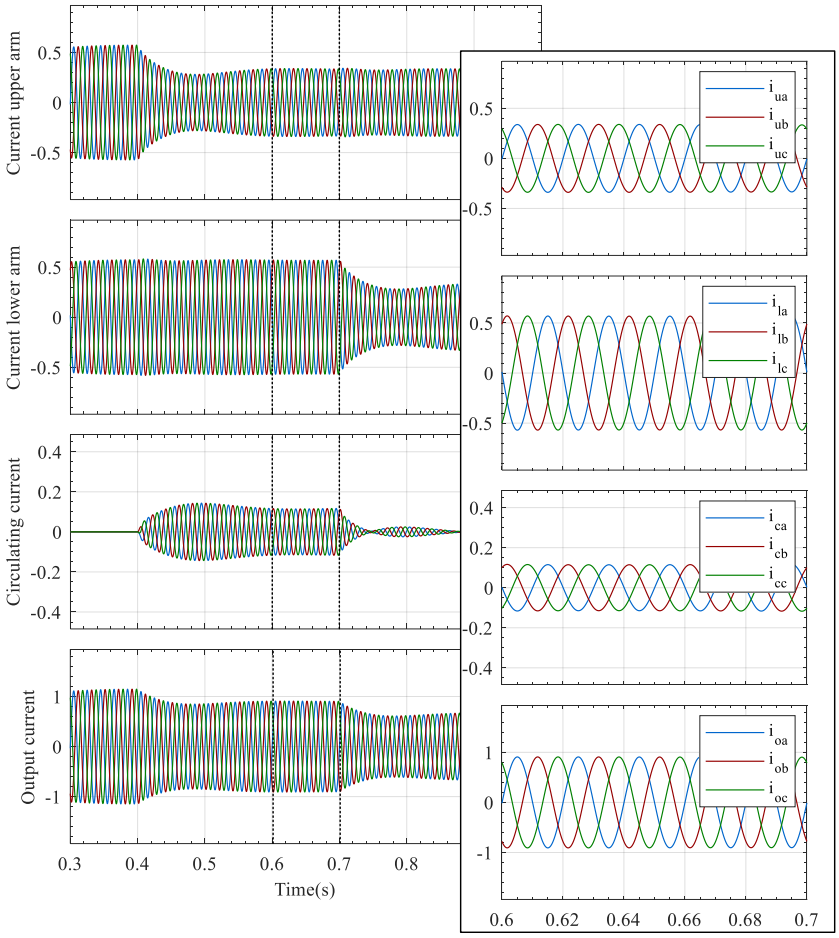

Fig. 3.24 Dynamic and steady state response of current arms, circulating current and output current under irradiation steps.

Event 2 – Irradiation step in modules of lower arm. A second event was introduced at 0.7s to study the effect of a power decrease in all modules of the lower arm when the irradiation level changed from 1000W/m2 to 600 W/m2. In Fig. 3.22 is shown how the power decrease from 0.5 to 0.3 pu created a balance operation between the arms again. This power variation also affected the dc voltage level in modules of the lower arm which returned to their reference value after 250 ms.

Because the irradiation in modules the lower arm decreased to the same irradiation level in modules of the upper arm, the current in both arms achieved the same amplitude. This effect reduced the circulating current to zero.

3.7.2 Study case II: DC voltage step in lower arm

In order to study an imbalance operation when different dc voltages are applied to PV panels. In this study case we introduced a voltage step in all modules of the lower arm after an irradiation step is set in modules of the upper arm. Similar to previous study case the same irradiation step was introduced. Fig. 3.25 to Fig. 3.27 show the power, voltage and current signals during the study case.

In Fig. 3.25 we observe the total power delivered to the grid as well as the average power provided by the upper and lower arms. Since all modules operated at nominal power during the first 0.4s, the total active power was 1 pu, while the power provided by each arm was 0.5 pu. In order to achieve these power levels, the dc voltages were set to 1 pu as shown in Fig. 3.26.

At 0.4s an irradiation step of 400 W/m2 was introduced in modules of the upper arm, giving rise to the same power and dc voltage behavior descried in previous section. Fig. 3.26 illustrates the dc voltage response during such event.

Event – dc voltage step in modules of lower arm. In this event, a dc voltage reference of 1.1 pu was set in all modules of the lower arm. Remember that a dc voltage increase triggers to a power decrease in the PV panels as shown in Fig. 3.21. Therefore, as expected, in Fig. 3.25 we can see how the total active power experienced a drastic change due to this new voltage reference. Because all modules of the lower arm were affected by the same voltage step, the dc voltage in all modules increased to the same dc voltage level.

The power change is also observed in the current arms. As seen in Fig. 3.27, at 0.7s the current amplitude of the lower arm decreased, giving rise to a reduction of the ac current injected to the grid. Furthermore, this event reduced the power difference between the upper and lower arm. Therefore, less circulating current flowed through the converter.

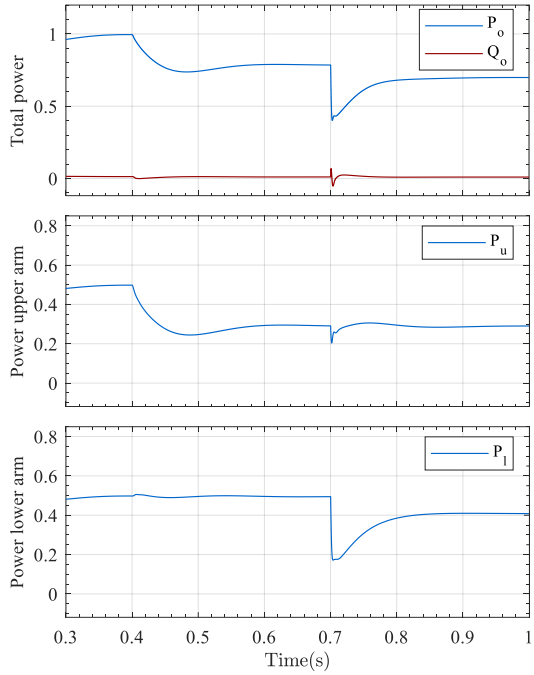

Fig. 3.25 Simulation results of total power and average power produced by the upper and lower arms under irradiation and dc voltage changes.

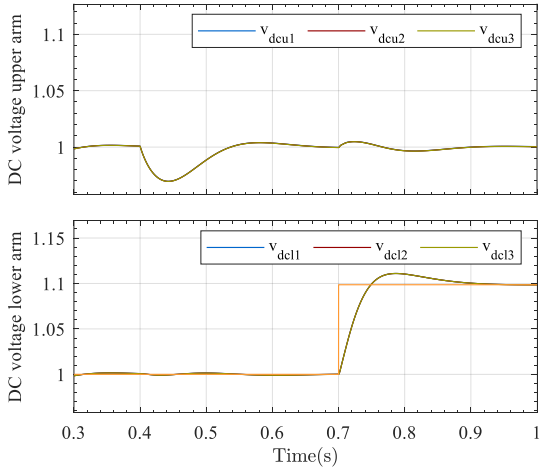

Fig. 3.26 DC voltage response in modules of the upper and lower arms under irradiation and dc voltage changes.

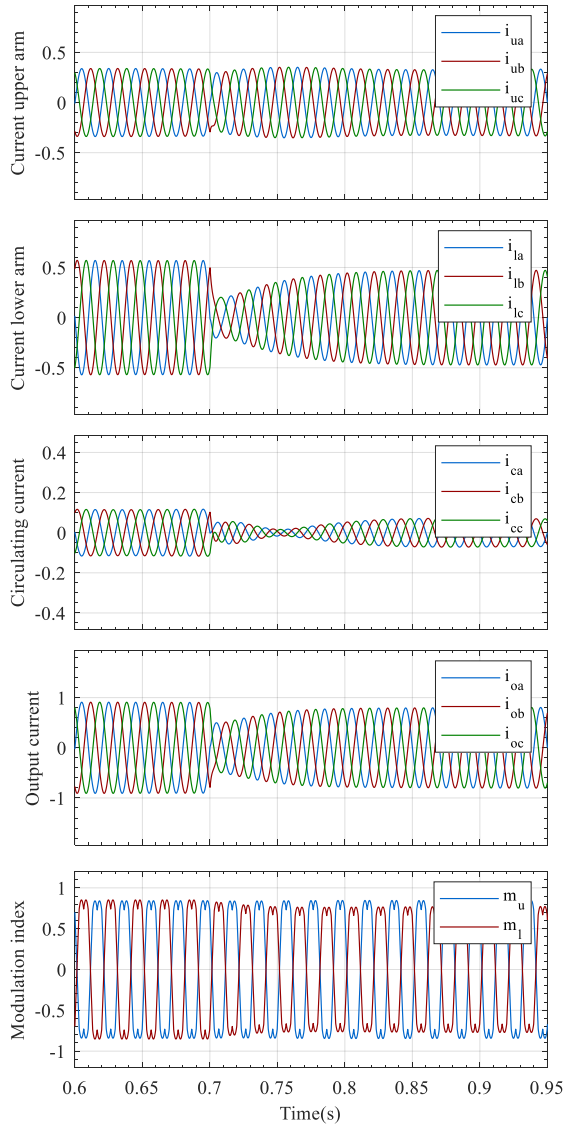

Fig. 3.27 Dynamic and steady state response of current arms, circulating current, output current and modulation indexes under irradiation and dc voltage changes.

An important result are the modulation indexes. Fig. 3.27 shows the general modulation indexes in the upper and lower arms provided by the central control before and after the imbalance operations. During the imbalance operation created by the irradiation step, the dc voltage in all modules remained at 1 pu, thus both modulation indexes maintained the same

amplitude despite of the power difference between the arms. However, after the second event, modules of the lower arm increased their dc voltage. Therefore, their modulation index decreased its amplitude to compensate such voltage difference.

3.8 Summary of the chapter

In this chapter, the control of the IMMC was described based on the analytical model studied in Chapter 2. The control proposed has a cascaded configuration with two inner controllers to regulate the output and circulating currents and two outer controllers to define the current references based on the square value of the total dc voltage in the upper and lower arms. Because the outer controllers regulate the total dc voltage, this control strategy does not differentiate when modules operate at different voltage levels. This is the reason why an internal control loop embedded in each module is required to allow an imbalance operation between modules of the same arm.

A tuning strategy based on the crossover frequency and phase margin technique was introduced to define the parameters in all control loops according to the requirements defined by the bandwidth and phase margin. Additionally, we evaluated the dynamic response through the complementary and load disturbance sensitivity functions by using the voltage and current models previously identified.

After tuning the voltage and current controllers, a general control architecture, including a synchronization technique was described. It is important to remark that the output and the circulating current control loops define the average modulation indexes for the upper and lower arms. This control stage was called central controller.

Simulation results based on a three-phase configuration with three modules per arm validated the operation principle through two study cases. These results analyzed the voltage and current behavior in a balance and imbalance operation by changing the irradiation and dc voltage levels in the PV panels. In an attempt to validate the central controller, we considered that all modules of one arm were affected by the same irradiation and voltage steps. However, this is not the most realistic case, as it will be shown in next chapter, where the series connection of modules in one arm may be affected by different voltage and irradiation conditions.

Chapter
4.

Amplitude and Quadrature Voltage Compensation

Previous chapter introduced and validated the central control architecture of the IMMC considering the same power distribution between modules of the same arm. As the central control is not able to operate under different power imbalances, in this chapter are studied two strategies to achieve this requirement. The Amplitude and Quadrature Voltage Compensation are located inside of each module, so the control signals can be tailored based on individual requirements. The work presented in this chapter is based on the publications "Energy balancing with wide range of operation in the Isolated Multi-Modular Converter", IEEE Access 2010 and "Quadrature Voltage Compensation for Imbalance Energy Operation in the IMMC", *Under revision*

4.1 Concept description

The series connection of modules and the power generation from independent dc sources bring several challenges to provide a stable operation in the IMMC. We have shown in Chapter 3 that a power imbalance between arms creates an inherent circulating current with no impact on the output current. The analysis presented considered the series connection of modules as an equivalent voltage source, which is not able to identify energy imbalances

when dc sources provide different power levels. However, using this approach it is easy to identify the effect of voltage and current signals on the active power.

In Chapter 2, the power in the upper and lower arms were studied in a three-phase system based on a synchronous reference frame. According to the analysis introduced, the active power per arm is reduced to.

$$\begin{aligned} p_{ou} &= \frac{3}{4}\left(v_{ud}i_{od} + v_{uq}i_{oq}\right) + \frac{3}{2}\left(v_{ud}i_{cd} + v_{uq}i_{cq}\right) \\ p_{ol} &= -\frac{3}{4}\left(v_{ld}i_{od} + v_{lq}i_{oq}\right) + \frac{3}{2}\left(v_{ld}i_{cd} + v_{lq}i_{cq}\right) \end{aligned} \tag{4.1}$$

From previous expressions we can summarize the following aspects:

- The power arms are commanded by two independent components. The first terms is associated to the output current, while the second term is associated to the circulatung current. By controlling both current independently, it is possible to regulate the power flow and compensate energy imbalances.
- Considering a small couple inductance, the voltage arms can be replaced by the output voltage. According to expression (2.4), the equivalent voltage in the upper and lower arms are reduced to $v_{u,dq} = -v_{o,dq}$ and $v_{l,dq} = v_{o,dq}$.
- The addition of both expressions described in (4.1) defines the total power deliveded into the grid. As it was demostrated in Chapter 2, this power depends on the output current. On the other side, the power difference between the arms depends on the circulatung current.
- A proper grid synchronization can be used to force to zero the output voltage v_{oq}. In this sense, the total active power is related to the *d* component of the output current while the power difference is related to the circulating current i_{cd}.

Focusing our attention on the power generated per module, the active power is reduced to:

$$P_{ci,k} = P_{dci,k} - P_{oi,k} \tag{4.2}$$

Where $P_{ci,k}$ is the absorbed or delivered power from the dc capacitor, $P_{dci,k}$ is the power provided by the external dc source and $P_{oi,k}$ is the output power. Because unpredictable conditions can affect the external dc sources, giving rise to uncertain power fluctuation, the power flow can be controlled through the output power, while $P_{dci,k}$ is considered as a perturbation.

This output power is defined by the current arm and the output voltage. In order to identify their effect on the active power, we can use the polar coordinates as described below.

$$p_{oi,k} = v_{i,k} i_i \cos(\theta_{i,k}) \tag{4.3}$$

Where $v_{i,k}$ is the output voltage of module *k* in arm ©, i_i is the current arm and $\theta_{i,k}$ is the angle difference between $v_{i,k}$ and i_i. There are important aspects that can be observed in expression (4.3). If the voltage or the current change, the power will also change. But, as the current arm impacts on the power flow of all modules at the same time, no individual power compensation is possible. Nevertheless, the voltage can be adjusted individually in each module without affecting the rest of modules. Therefore, different power levels can be achieved. Under this concept, we are able to modify the power flow, maintaining a stable operation. The output voltage can be adjusted either based on its amplitude or phase-angle. However, each of them will have different impacts on the power flow. Using this approach, the Amplitude and Quadrature voltage compensation are introduced and described to demonstrate their effectivity under different power imbalances.

4.2 Amplitude voltage compensation

The amplitude voltage compensation is a control strategy widely used in cascaded converters to operate with power modules under diverse imbalance states. The control strategy has been used in many converters, some of them are the classical CHB and T-Type [115]–[119]. This modifies the modulated voltage according to the difference between the power generated and absorbed. In this sense, modules will increase or reduce the voltage amplitude to control the power flow.

As it was described in Chapter 2, the output voltage in each module is represented according to the modulation index and the dc voltage as follows.

$$v_{i,k} = \frac{v_{dc,i,k}}{2} m_{i,k} \tag{4.4}$$

Considering a constant dc voltage level, the modulation index $m_{i,k}$ can be used to control the output voltage. This is represented as a sinusoidal signal with an amplitude $\hat{m}$ and phase angle $\theta_{i,k}$.

$$m_{i,k} = \hat{m}_{i,k} \cos(\omega t + \theta_{i,k}) \tag{4.5}$$

Combining equations (4.3), (4.4) and (4.5), it is observed that the power flow is controlled by changing the modulation index amplitude. If the modulation index increases, the output power also increases. Otherwise, when the modulation index decreases, the power decreases. Based on this concept we can introduce a control algorithm to regulate the power flow.

4.2.1 Control description

As described in previous section, the modulation index can be used to control the power flow by changing its amplitude. Replacing equation (4.4) in (4.1) and reorganizing each element according to the *dq* components, the active power per module is rewritten as.

$$\begin{aligned} p_{ou,k} &= \frac{3}{4} v_{dcu,k} m_{ud,k} \left(\frac{i_{od}}{2} + i_{cd} \right) + \frac{3}{4} v_{dc,k} m_{uq,k} \left(\frac{i_{oq}}{2} + i_{cq} \right) \\ p_{ol,k} &= \frac{3}{4} v_{dcl,k} m_{ld,k} \left(-\frac{i_{od}}{2} + i_{cd} \right) + \frac{3}{4} v_{dcl,k} m_{lq,k} \left(-\frac{i_{oq}}{2} + i_{cq} \right) \end{aligned} \tag{4.6}$$

The synchronization angle forces the *d* component of the voltage equal to the amplitude. Therefore, $m_{id,k}$ is related to the modulation index amplitude, while $m_{iq,k}$ is related to its phase angle. Because this control strategy aims to compensate the modulation index amplitude, $m_{id,k}$ can be defined as follows.

$$m_{id,k} = m_{id} + \Delta m_{id,k} \tag{4.7}$$

According to (4.7), the modulation index m_{id} represents the control signal given by the central control, while $\Delta m_{id,k}$ is the compensation required to adapt the power flow in module *k*. The central control studied in previous chapter regulates the total dc voltage per arm based on the output and circulating current control loops. The decoupling of their output signals through equation (4.8) and (4.9) are used to define the modulated voltage in the upper and lower arms.

$$\begin{bmatrix} \mathbf{v_u} \\ \mathbf{v_l} \end{bmatrix} = T_{IMMC}^{-1} \begin{bmatrix} \mathbf{v_{\Delta\alpha\beta 0}} \\ \dfrac{\mathbf{v_{\Sigma\alpha\beta 0}}}{2} \end{bmatrix} \tag{4.8}$$

Where $\mathbf{v_{\Delta\alpha\beta 0}}$ is related to the voltage difference $\mathbf{v_{s\alpha\beta 0}}$ and $\mathbf{v_{\Sigma\alpha\beta 0}}$ is related to the drop voltage $\mathbf{v_{c\alpha\beta}}$ by.

$$\begin{bmatrix} \mathbf{2v_{s\alpha\beta 0}} \\ \mathbf{v_{c\alpha\beta}} \end{bmatrix} = -\begin{bmatrix} \mathbf{v_{\Delta\alpha\beta 0}} \\ \dfrac{\mathbf{v_{\Sigma\alpha\beta 0}}}{\mathbf{2}} \end{bmatrix} \tag{4.9}$$

Introducing equation (4.7) in (4.6), the output power yields.

$$\begin{aligned} p_{ou,k} &= \frac{3}{4} v_{dcu,k} (m_{ud} + \Delta m_{ud,k}) \left(\frac{i_{od}}{2} + i_{cd} \right) + \frac{3}{4} v_{dc,k} m_{uq,k} \left(\frac{i_{oq}}{2} + i_{cq} \right) \\ &= \bar{p}_{ou,k} + \Delta p_{ou,k} \end{aligned} \tag{4.10}$$

$$\begin{aligned} p_{ol,k} &= \frac{3}{4} v_{dcl,k} (m_{ld} + \Delta m_{ld,k}) \left(-\frac{i_{od}}{2} + i_{cd} \right) + \frac{3}{4} v_{dcl,k} m_{lq,k} \left(-\frac{i_{oq}}{2} + i_{cq} \right) \\ &= \bar{p}_{ol,k} + \Delta p_{ol,k} \end{aligned} \tag{4.11}$$

There is an important aspect in expressions (4.10) and (4.11). The output power can be divided in two components: the average power $\bar{p}_{ox,k}$ related to the modulation index given by the central control and the power compensation $\Delta p_{ox,k}$ required to control the power flow under possible imbalances. As we know from previous analysis, the grid synchronization aids to decouple the *dq* components and attribute the *d* component of the modulation index to the active power, while the *q* component is related to the reactive power. Because no power compensation is provided by $m_{iq,k}$, the average power can be affected by the output current i_{oq} and the circulating current i_{cq}. If no phase angle is introduced in the output voltage, the modulation index $m_{iq,k}$ is zero. Therefore, neither the circulating current i_{cq} or the output current i_{oq} have an effect on the active power. However, when a phase angle is introduced in the output voltage, the modulation index $m_{iq,k}$ is different from zero, creating a dependency between the active power and the circulating current i_{cq}. Considering the case when no phase angle is introduced in the output voltage, the power compensation is reduced to.

$$\Delta p_{ou,k} = \frac{3}{4} v_{dcu,k} \Delta m_{ud,k} \left(\frac{i_{od}}{2} + i_{cd} \right) \tag{4.12}$$

$$\Delta p_{ol,k} = \frac{3}{4} v_{dcl,k} \Delta m_{ld,k} \left(-\frac{i_{od}}{2} + i_{cd} \right) \tag{4.13}$$

In order to define the proper power compensation, we can adopt the analysis introduced in Fig.2.5, where the current provided by the external dc source $i_{dci,k}$ is formed by the current flowing through the dc capacitor $i_{ci,k}$ and the current flowing through module *k*.

$$\begin{aligned} i_{dci,k} &= i_{ci,k} + i'_{dci,k} \\ &= C_{sm} \frac{dv_{dci,k}}{dt} + m_{i,k} i_i \end{aligned} \tag{4.14}$$

The current $i_{ci,k}$ is defined by the dynamic response of the dc capacitor, while $i'_{dci,k}$ is set by the current arm and the modulation index. In order to decouple the control strategy from the current arm, we need to divide the modulation index by i_i. This could trigger to high compensation levels when the current arm is close to zero, giving rise to possible unstable states. To solve this problem, we consider the nominal current level, reducing the performance of the controller but ensuring a proper voltage compensation.

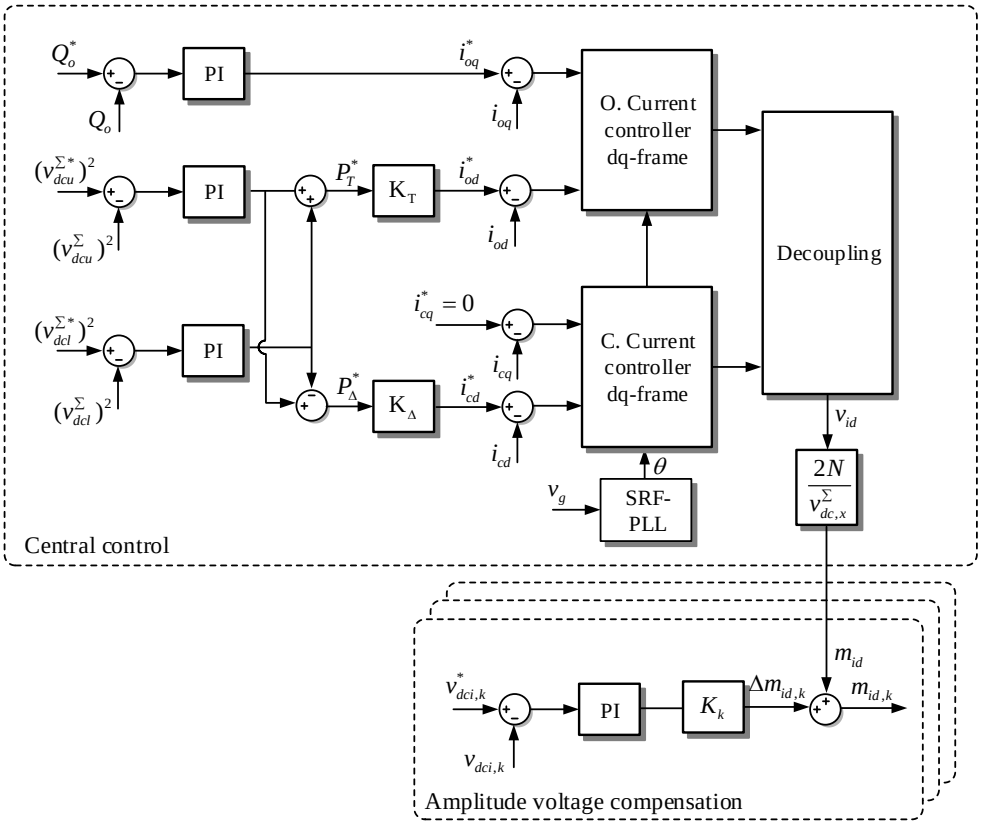

Fig. 4.1 Amplitude voltage compensation strategy for modules in upper and lower arm

Fig. 4.1 illustrates the connection between the central control and the amplitude voltage compensation. The voltage difference between the reference $v_{dci,k}^*$ and the measurement voltage $v_{dci,k}$ is processed through a PI controller, which defines the compensation $\Delta m_{id,k}$ added to the general modulation index m_{id}. Note that the general modulation index is normalized through the voltage $v_{dc,i}^{\Sigma}$ and the number of modules per arm. Therefore, its value fluctuates between -1 and 1. Additionally, a constant k_x is defined to add the

compensation $\Delta m_{id,k}$ in modules of the upper arm and substract the compensation from modules of the lower arm.

4.2.2 Effect of amplitude voltage compensation on imbalance operation

The amplitude voltage compensation provides the capability to withstand different power imbalances. The tailored modulation index provided by each module can be achieved using the control architecture shown in Fig. 4.2. The central control is formed by the voltage and current controllers which define the general modulation index m_u and m_l. Then, the local control set the modulation index $m_{u,k}$ and $m_{l,k}$ for each module.

Using the IMMC shown in Fig.3.17 where a three-phase configuration with three modules per arm is studied, we are able to define different irradiation levels, so each module operates at difference operating points. However, before continuing, a few things regarding the limitations of the amplitude voltage compensation should be pointed out. When the modulated voltage is normalized, its operating range oscillates between -1 and 1. Therefore, its amplitude must fulfill the following expression.

$$\sqrt{(m_{id} + \Delta m_{id,k})^2 + m_{iq}^2} \leq 1 \tag{4.15}$$

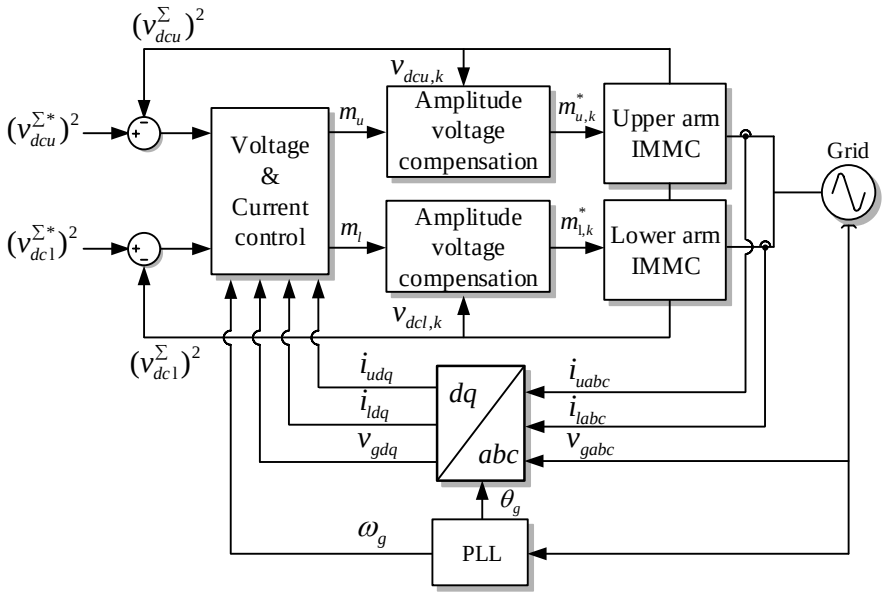

Fig. 4.2 Control architecture based on the amplitude voltage compensation

As higher the central modulation index m_{id} is, lower is the capability to withstand larger power imbalances. This limitation has to be taken into consideration when defining the maximum power imbalance.

To evaluate the performance of this control strategy, simulation scenarios are presented considering irradiation steps in two modules of the upper arm and one module of the lower arm. These scenarios were chosen based on the initial steady state operation at nominal power, with each module providing 1 MW of power at 1000 W/m2. Note that next results are in per unit.

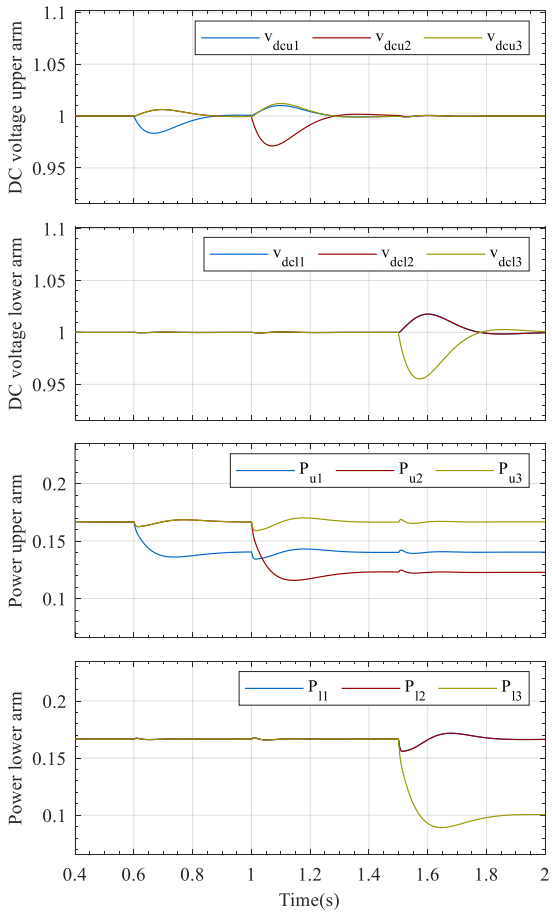

Fig. 4.3 Simulation results of dc voltages and active power in modules of the upper and lower arms using the amplitude voltage compensation

Fig. 4.3 illustrates the dc voltages and the active powers in all modules. At t = 0.6 s, the irradiation level in the first module of the upper arm decreased from 1000 W/m2 to 850

W/m2. This irradiation step reduced the power P_{u1} provided by module M_{u1} in 18% (from 0.166 pu to 0.137 pu), triggering to a small change in $v_{dcu,1}$. However, the voltage reference given by the MPPT algorithm did not change, forcing the local controller to compensate the modulation index, and thus returning the dc voltage $v_{dcu,1}$ to its reference value. This power difference reduced the total power in the upper arm, creating an imbalance operation.

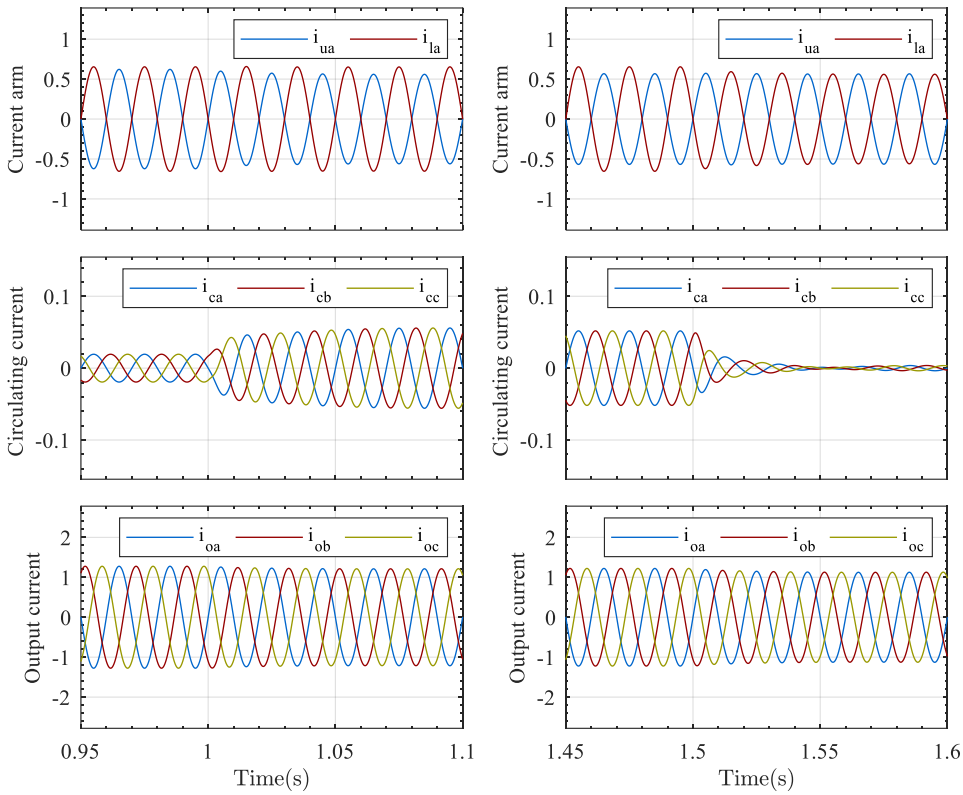

Fig. 4.4 Simulation results of current arms, circulating current and output current using the amplitude voltage compensation. (a) Irradiation step in module M_{u2}, (b) Irradiation step in module M_{l3}

At t = 1s, the second module of the upper arm decreased its irradiation level from 1000 W/m2 to 750 W/m2. Therefore, the power P_{u2} provided by M_{u2} decreased in 27%. With this second power decrease, the power difference between the arms became larger. Creating

a higher current difference between the arms and a circulating current flowing through the converter as can be seen in Fig. 4.4a.

Note that before the second event happened, the current arms described a slight difference in their amplitudes due to the irradiation step introduced in the first event. This difference created a small circulating current which was intrinsically related to the power difference P_{Δ} illustrated in the control diagram of Fig. 4.1.

The last irradiation step was introduced in the third module M_{l3} of the lower arm at t = 1.4 s. On this occasion, the irradiation decreased in 380 W/m2, reducing the power P_{l3} in 40% as seen in Fig. 4.3. This power change reduced the amplitude of the lower current arm and thus, the difference between i_u and i_l. As a result, the circulating current decreased to almost zero as illustrated in Fig. 4.4b.

The capability to withstand the three irradiation steps was possible thanks to the compensation provided the amplitude voltage compensation. The reaction of the modulation indexes under these three events is illustrated in Fig. 4.5.

Fig. 4.5.a shows how the power decrease in module M_{u1} increased the modulation index m_{u2} and m_{u3} while the modulation index m_{u1} decreased. As M_{u2} and M_{u3} generated the same power level, both modules held the same modulation amplitude. However, this situation changed after the second event happened as seen in Fig. 4.5b, where the power generated by module M_{u2} decreased. In this case, the modulation index m_{u2} reduced its amplitude to the lowest level while m_{u3} increased its amplitude close to 1. Note that all modules of the lower arm did not provide any compensation to their modulation indexes as they operated at the same power level.

Finally, the third power change in module M_{l3} increased the amplitude of the modulation indexes m_{l1} and m_{l2} at the same level while m_{l3} was significantly reduced. Compare to previous events, a similar result was achieved in the first event, when module M_{u1} reduced its power level. Analyzing the three different scenarios, we can conclude that the amplitude voltage compensation increases the modulation index when modules compensate higher power levels and reduce the modulation index when the power compensation is smaller.

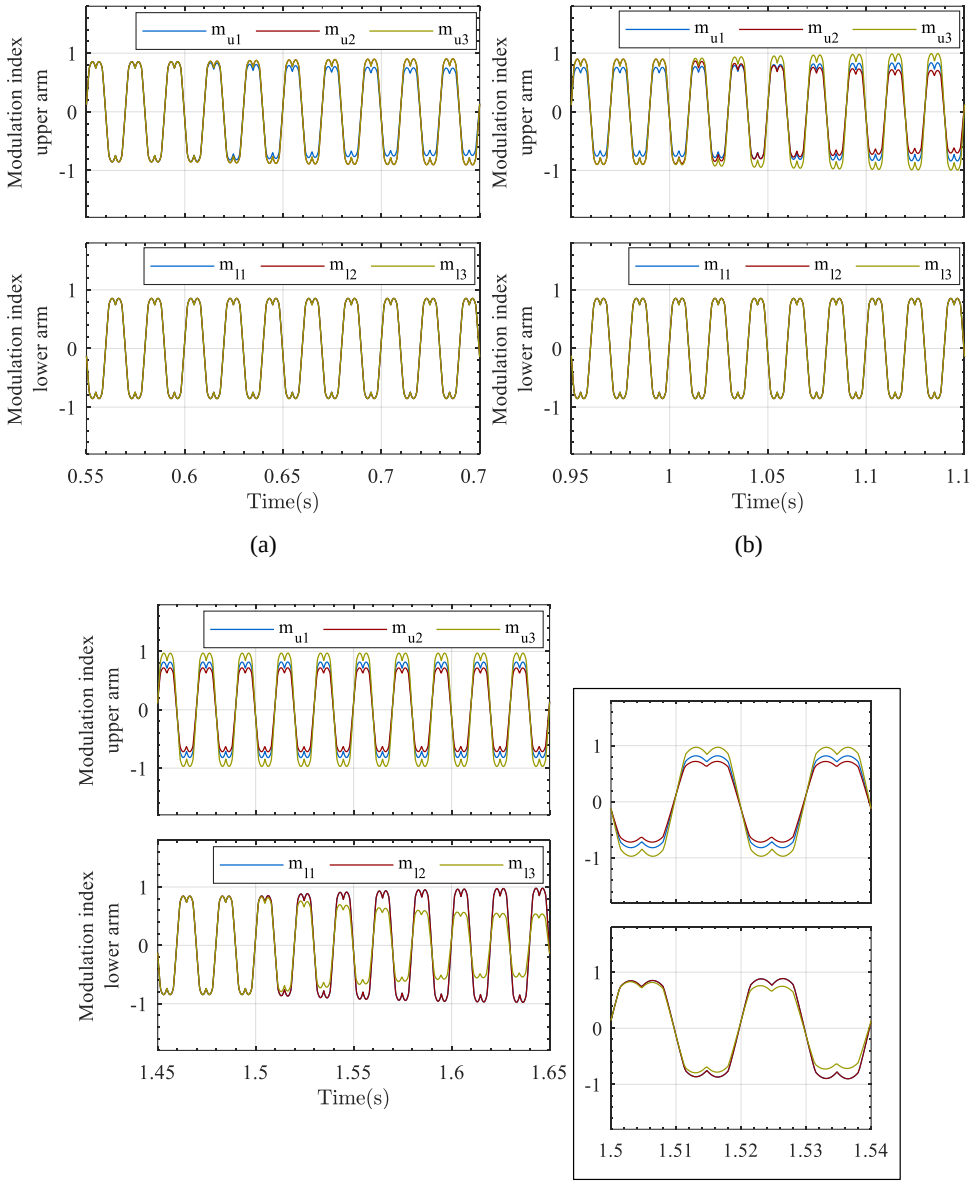

Fig. 4.5 Simulation results of modulation indexes in modules of the upper and lower arms under irradiation steps. (a) Event 1, (b) Event 2, (c) Event 3

4.2.3 Experimental results

In order to evaluate the performance of the amplitude voltage compensation, experimental results were conducted using the downscale prototype introduced in Appendix A. The laboratory setup has a nominal power of 4.8 kW and is formed by two modules connected in series through three-phase transformers. PV panels are emulated through constant dc sources connected in series to dc resistors. In this sense, each module is able to operate between its open circuit level (when no power is generated) and the maximum power level.

The set-up was initiated with all modules operating at nominal power and with a constant dc voltage level of 360 V as seen in Fig. 4.6. As all modules generated their maximum power, the upper and lower current arm had a similar amplitude but shifted 180º. In Fig. 4.7 is illustrated the phase *a* of the current arms and the three phases of the circulating current flowing through the converter. Note that a small circulating current is observed when all modules operated at nominal power due to a slight difference between the power generated in both arms.

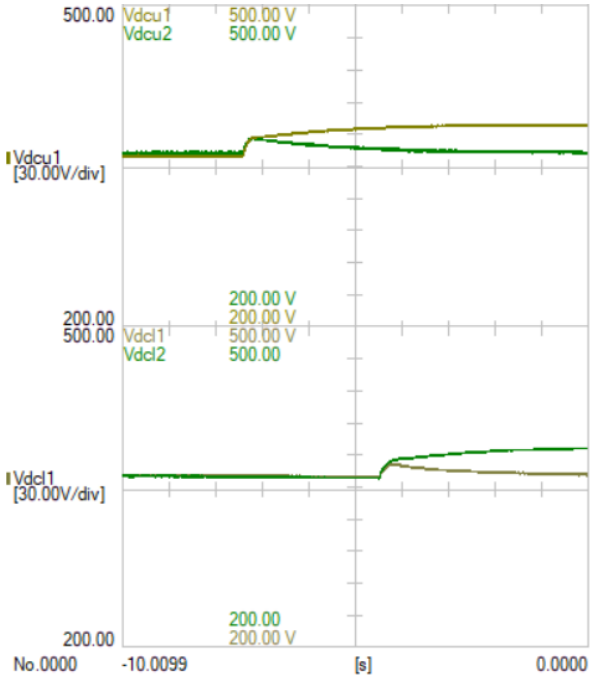

Fig. 4.6 Experimental results of dc voltage steps in modules of upper and lower arms using the amplitude voltage compensation

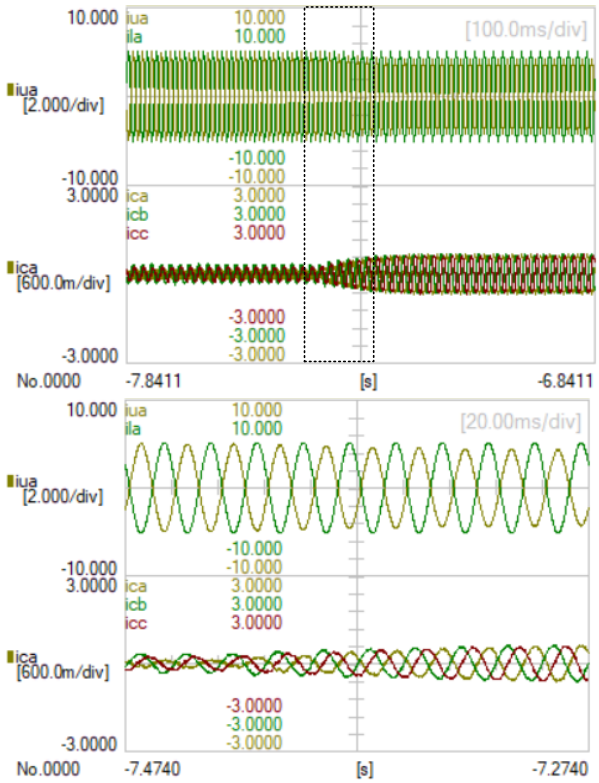

Fig. 4.7 Experimental results of first event. Current arm, and circulating current using the amplitude voltage compensation

In the first event, the dc voltage v_{dcu1} of module M_{u1} increased from 360 V to 390 V, giving rise to a power decrease of 390 W. It is important to point out that larger voltage steps are not possible because the modulation index may go beyond the maximum level imposed by the overmodulation. Results in Fig. 4.7 illustrate how the current in the upper arm i_{ua} decreased its amplitude as the dc voltage v_{dcu1} increased. Moreover, it can be seen how the three-phase circulating current flowing through the converter also increased as a consequence of the power imbalance between the arms.

In the second event, a dc voltage was set in module M_{l2} to compensate the first power imbalance introduced by module M_{u1}. In Fig. 4.6 is shown the time when v_{dcl2} increased while module M_{l1} maintained the same voltage level. This event reduced the power generated in the lower arm by 390 W, decreasing the current arm amplitude i_l as seen in Fig. 4.8.

After the dynamic transient, both current arms operated under similar amplitude levels, so the circulating current decreased close to zero

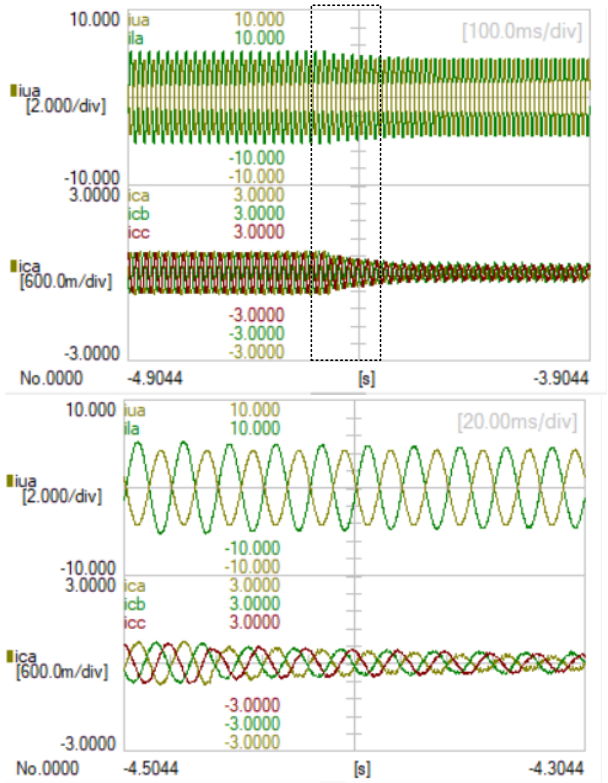

Fig. 4.8 Experimental results of second event. Current arm and circulating current using the amplitude voltage compensation

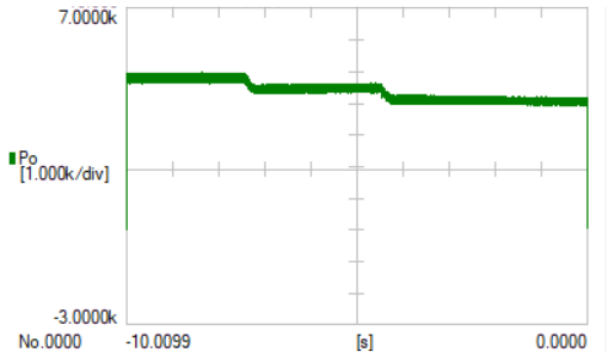

Fig. 4.9 Experimental result of active power using the amplitude voltage compensation

To finalize, the dynamic response of the active power delivered to the grid under all dc voltage steps is illustrated in Fig. 4.9. It can be seen how the first voltage step introduced by M_{u1} reduced the total power in approximately 390W and then the second voltage step introduced by M_{l2} reduced the power in 390W again.

4.3 Quadrature voltage compensation

So far we have use the amplitude voltage compensation to operate under power imbalances between modules of the same arm. Even though, this control strategy describes a high performance and fast response, the limitation to withstand large power imbalances reduces its flexibility. In PV applications, it is expected that each module is able to track its maximum power at any time. However, when modules operate at different power levels, the maximum power level might not be achieved. In this section we introduce a control strategy called quadrature voltage compensation which phase shifts the output voltage to withstand larger levels of power imbalances.

Equation (4.3) demonstrated that the power provided by each module depends on the current amplitude, voltage amplitude and angle difference between both signals. The amplitude voltage compensation was focused on changing the voltage amplitude through the modulation index. So, each module could adapt its $m_{id,k}$ component based on the dc voltage level. On this occasion we modify the angle difference between the output voltage and current arm.

According to (4.6), the output power of each module is given by the output current, the circulating current and the *dq* components of the modulation index. The angle set by the synchronization control loop relates the *d* component of the output voltage to $m_{id,k}$, while $m_{iq,k}$ is related to the phase angle. In order to control the power flow through the phase angle, we will control the *q* component of the modulation index as follows.

$$m_{iq,k} = m_{iq} + \Delta m_{iq,k} \tag{4.16}$$

Where m_{iq} is given by the central control and $\Delta m_{iq,k}$ is the compensation given by the local controller embedded in module *k*. Note that in this occasion there is no compensation in the *d* component $m_{id,k}$. Introducing equation (4.16) in (4.6), the power provided by module *k* in the upper and lower arms is reduced to.

$$p_{ou,k} = \frac{3}{4} v_{dcu,k} m_{ud,k} \left(\frac{i_{od}}{2} + i_{cd} \right) + \frac{3}{4} v_{dcu,k} \left(m_{uq,k} + \Delta m_{uq,k} \right) \left(\frac{i_{oq}}{2} + i_{cq} \right) \\ = \bar{p}_{ou,k} + \Delta p_{ou,k} \tag{4.17}$$

$$p_{ol,k} = \frac{3}{4} v_{dcl,k} m_{ld,k} \left(-\frac{i_{od}}{2} + i_{cd} \right) + \frac{3}{4} v_{dcl,k} \left(m_{lq,k} + \Delta m_{lq,k} \right) \left(-\frac{i_{oq}}{2} + i_{cq} \right) \\ = \bar{p}_{ol,k} + \Delta p_{ol,k} \tag{4.18}$$

In both arms, the output power can be divided in two components. The average power $\bar{p}_{oi,k}$ defined by the *dq* components of the output and circulating currents multiplied by the average modulation index, and the compensation power $\Delta p_{oi,k}$ provided by the *q* component of the output and circulating currents multiplied by the compensation $\Delta m_{iq,k}$. In the case of the average power, there is no difference between expressions (4.17)-(4.18) and expressions (4.10)-(4.11). However, the power given by the quadrature voltage compensation is reduced to.

$$\Delta p_{ou,k} = \frac{3}{4} v_{dcu,k} \Delta m_{uq,k} \left(\frac{i_{oq}}{2} + i_{cq} \right) \tag{4.19}$$

$$\Delta p_{ol,k} = \frac{3}{4} v_{dcl,k} \Delta m_{lq,k} \left(-\frac{i_{oq}}{2} + i_{cq} \right) \tag{4.20}$$

The output current i_{oq} controls the reactive power delivered to the grid, while i_{cq} is a circulating current flowing inside the converter. In previous section we determined that the current component i_{cd} arrives when there is a power difference between the upper and lower arm. However, i_{cq} was freely chosen as it does not have any influence on the power imbalance. Therefore, for the amplitude voltage compensation, the current reference i_{cq} was set to zero. On this occasion, as seen in equations (4.19) and (4.20), the power compensation can be provided by the circulating current i_{cq} if necessary. For instance, when no reactive power is delivered to the grid, the current i_{oq} is zero, so a minimum current i_{cq} is required to provide a proper power compensation.

In order to control the power flow, it is possible to increase or decrease the circulating current i_{cq}, so the level of $\Delta m_{iq,k}$ can be adapted. The relationship between both components is described below.

4.3.1 Dependency between circulating current and modulation index

The circulating current flows through the arms, so it can be used to change the power in all modules at the same time. However, the right power compensation will be provided by the local modulation index $m_{iq,k}$. This component phase shifts the output voltage in each module, so the power changes individually. In Fig. 4.10 is illustrated the operation principle of the quadrature voltage compensation in three consecutive modules connected in series. v_{oi} is the arm voltage formed by the addition of the output voltages $v_{i,k}$, $v_{i,k+1}$ and $v_{i,k+2}$ respectively, which can be decomposed into their *d* and *q* components.

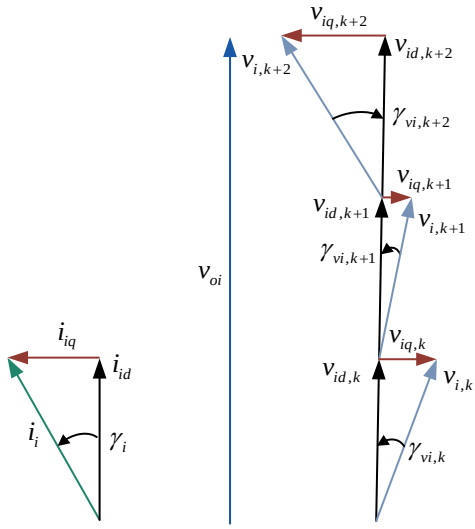

Fig. 4.10 Representation of output voltage based on the series connection of three consecutive modules

Similar to the output voltage vectors, the current arm can also be decomposed into its *dq* components. However, both signals depend on the output and circulating currents. So, any change in their references will modify the current angle γ_i. For instance, when no reactive power is delivered into the grid, the current i_{oq} is zero, thus the current component i_{iq} is only commanded by the circulating current.

As mentioned, the individual compensation is provided by the output voltage. When the voltage component $v_{iq,k}$ increases, the phase angle $\gamma_{v,k}$ also increases. This angle can be defined based on *dq* components of the output voltage or modulation index as follows.

$$\gamma_{vi,k} = \tan^{-1}\left(\frac{v_{iq,k}}{v_{id,k}}\right) = \tan^{-1}\left(\frac{m_{iq,k}}{m_{id,k}}\right) \tag{4.21}$$

The addition of the *dq* components of all modules in one arm will define the total voltage v_{oi} as.

$$v_{oi} = \sum_{k=1}^{N} v_{i,k} = \sum_{k=1}^{N} v_{id,k} + j\sum_{k=1}^{N} v_{iq,k} \tag{4.22}$$

In order to evaluate the effect of the circulating current i_{cq} and the phase angle γ_{vd} on the power response, Fig. 4.11 and Fig. 4.12 illustrate two different cases, where the power changes in one module of the upper and lower arm. In this analysis, balance operation refers when there is no power difference between the arms, so the total power provided is the same. On the other hand, the imbalance operation is given when there is a power difference between both arms. Fig. 4.11 analyzes the power response in balance operation.

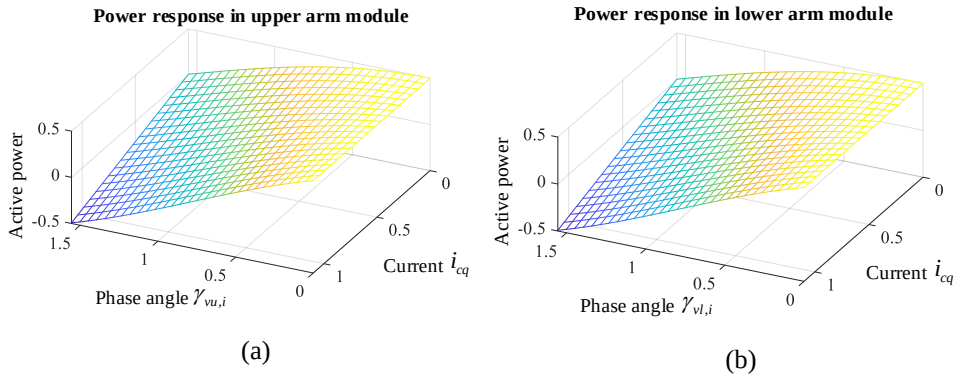

Fig. 4.11 Active power response in balance operation under circulating current and phase angle variations. (a) Power in module of upper arm, (b) Power in module of lower arm

The nominal power provided by each module is 0.5. When no circulating current i_{cq} flows through the arms, there is no power compensation regardless the phase angle γ_{vi} value. This response confirms the analysis introduced in (4.17) and (4.18), where it was stated that a *q* component of output or circulating current is required to control the power flow in the quadrature voltage compensation. When the circulating current i_{cq} is different from zero, small changes in the phase angle affects the active power provided by the module. The impact of the phase angle becomes larger as the circulating current increases. For instance, a circulating current of 0.51 pu requires a phase angle of 0.4 radians to compensate

30 % of power, the same compensation is achieved when the phase angle is 0.83 radians with a circulating current of 0.16 pu.

In imbalance operation, a circulating current i_{cd} flows through the converter due to a power difference between the arm. This current may change the phase angle γ_i as the current arm depends on the output and circulating currents. Equation (4.23) represents the upper and lower current arm in the *dq* reference frame.

$$\begin{aligned} i_u &= \left(\frac{i_{od}}{2} + i_{cd}\right) + j\left(\frac{i_{oq}}{2} + i_{cq}\right) \\ i_l &= \left(-\frac{i_{od}}{2} + i_{cd}\right) + j\left(-\frac{i_{oq}}{2} + i_{cq}\right) \end{aligned} \tag{4.23}$$

However, the individual power variation is given by the output voltage $v_{iq,k}$. Fig. 4.12 illustrates the power response when there is a power difference of 40% between both arms. On this occasion, module of the lower arm provides an initial power of 0.2 pu, while module of the upper arm generates 0.5 pu. Similar to previous scenario, no circulating current i_{cq} limits the capability to change the power when the phase angle of the output voltage increases. However, a small change in the circulating current increases the compensation as long as the phase angle γ_{vi} increases.

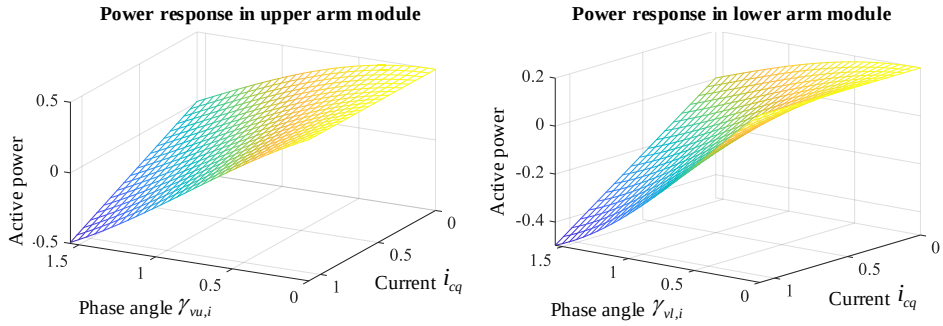

(a) (b)

Fig. 4.12 Active power response in imbalance operation under circulating current and phase angle variations. (a) Power in module of upper arm, (b) Power in module of lower arm

Negative values of active power means that the module consume power. For PV applications, the minimum power comes about when no energy is provided by the primary

sources, i.e. when the active power is zero. Combining expressions (4.17) to (4.21), the phase angle can be represented in terms of the active power and the current arm as follows.

$$\gamma_{vi,k} = \tan^{-1}\left(\frac{1}{i_{iq}}\left(\frac{2}{3}\frac{p_{i,k}}{v_{id,k}} - i_{id}\right)\right) \tag{4.24}$$

For values of i_{iq} close to zero, the phase angle $\gamma_{vi,k}$ is approximately $\pi/2$. Therefore, an output voltage almost orthogonal to the current arm is required to generate a certain power level. However, this value will demand a high level of $v_{iq,k}$, which is not always affordable. Conversely, higher values of i_{iq} will give us more flexibility to compensate a certain power level, demanding lower values of phase angle $\gamma_{vi,k}$. The maximum operation of the quadrature voltage compensation can be defined based on the overmodulation level through the following expression.

$$\sqrt{m_{id}^2 + (m_{iq} + \Delta m_{iq,k})^2} \leq 1 \tag{4.25}$$

On this occasion, the average modulation index m_{id} and m_{iq} are given by the central control, while the compensation $\Delta m_{iq,k}$ is set by the local control. The representation of the central control in combination with the quadrature voltage compensation is illustrated in Fig. 4.13. Similar to the amplitude voltage compensation described in previous section, the current references are given by outer control loops. However, the circulating current i_{cq} is defined according to a droop gain $\mathrm{K_{iq}}$ which provides a certain current level based on the maximum current allowed and the level of power imbalance. The difference between the reference and the dc voltage is processed through a PI controller, which defines the compensation $\Delta m_{iq,k}$ required in each module. This component is multiplied by the circulating current sign and then multiplied by k_k to add or subtract $\Delta m_{iq,k}$ from the average modulation index m_{iq}. Note that k_k is 1 for modules of the upper arm and -1 for modules of the lower arm.

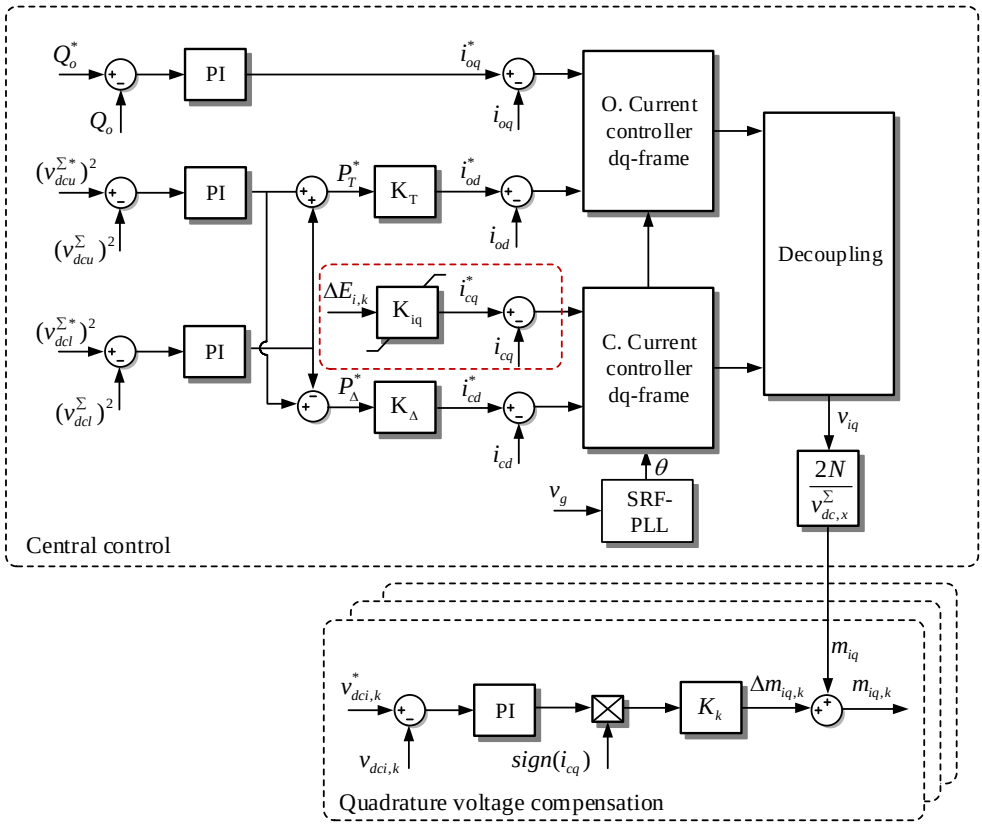

Fig. 4.13 Quadrature voltage compensation strategy for modules in upper and lower arms

4.3.2 Effect of quadrature voltage compensation on imbalance operation

To evaluate the quadrature voltage compensation, simulation results are studied based on the setup implemented in previous section. The three-phase IMMC configuration illustrated in Fig.3.17 has a nominal power of 6MW with each module providing up to 1MW. The electrical parameters are described in table 3.5.

Before the irradiation level changes in the primary sources, all modules operated at nominal power. However, when module M_{u1} reduced its irradiation from 1000 W/m2 to 850 W/m2, the power provided by M_{u1} decreased in 18%. This sudden irradiation step affected the dc voltage, which was quickly compensated. In Fig. 4.14 it is illustrated how the dc voltage returned to its reference value after the irradiation step was introduced. Note

that a small perturbation in the output power came out as a result of the circulating current i_{cq} required to compensate the power imbalance between modules in the upper arm.

After 0.7 s, a second irradiation step was introduced in the second module of the upper arm. Similar to the analysis presented in the amplitude voltage compensation, the irradiation decreased from 1000 W/m2 to 750 W/m2, reducing the power provided by M_{u2} in 28%. Due to this power decrease, the dc voltage $v_{dcu,2}$ reduced its value, but it was quickly compensated through the local controller embedded in each module, returning to its reference value at 1 pu. Because the amplitude voltage compensation affects the phase angle of the output voltage, a higher oscillation is observed in the dc side.

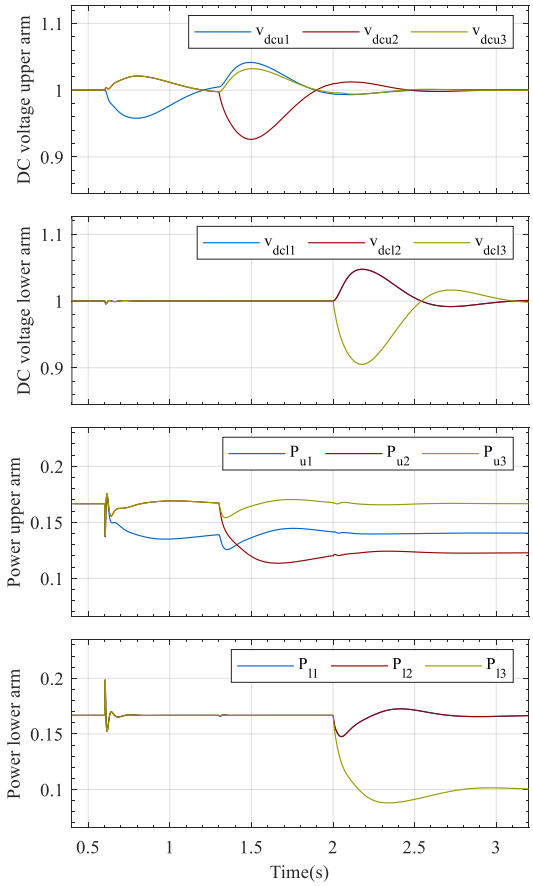

Fig. 4.14 Simulation results of dc voltages and active power in modules of the upper and lower arms using the quadrature voltage compensation

The voltage compensation was possible thanks to the circulating current i_{cq} introduced, which phase shifted the angle difference between the current arms. Fig. 4.15 shows the current response before and after the first even happened. While both arms generated the same power level, the current arms had the same amplitude but shifted 180º. This difference was given by the current definition of the converter in Chapter 2, which defined both component in opposite direction. When the irradiation decreased in module M_{u1}, the power difference between modules of the upper arm triggered an increase of the circulating current as seen in the second result of Fig. 4.15. This current was intentionally set at 25% of the nominal current arm, creating an angle difference as seen in the first result of Fig. 4.15. This power difference also created a small deviation between the current amplitudes, and thus a circulating current i_{cd} flowing inside the converter. Therefore, the circulating current was formed by i_{cd} and the current i_{cq} imposed to control the power imbalance.

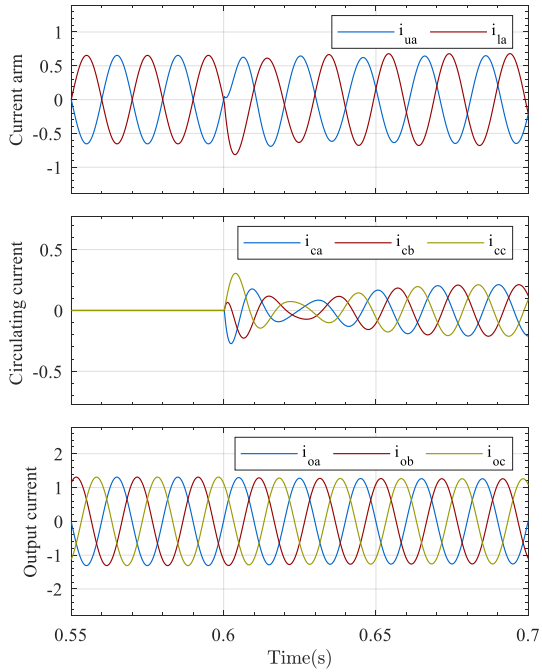

Fig. 4.15 Simulation results of first irradiation step using the quadrature voltage compensation. Current arms, circulating current and output current

In order to create a complete imbalance operation, a third irradiation step was introduced in module M_{l3}. At t = 2 s, the irradiation decreased from 1000 W/m2 to 620 W/m2,

triggering to a power decrease of 40%. In Fig. 4.14, we can see how the power variation created an oscillation in the dc voltage, which was quickly compensated.

The effect of this power variation is also observed on the current arm i_{la}. Fig. 4.16 shows the time when the irradiation level of module M_{l3} decreased. We can see that the current i_{la} reduced its amplitude while the power decreased. Because the circulating current i_{cq} maintained the same level defined in the first irradiation step, the angle difference between both current arms remained unchanged. In the case of the output current, there was a decrease of its amplitude level since less power was delivered into the grid.

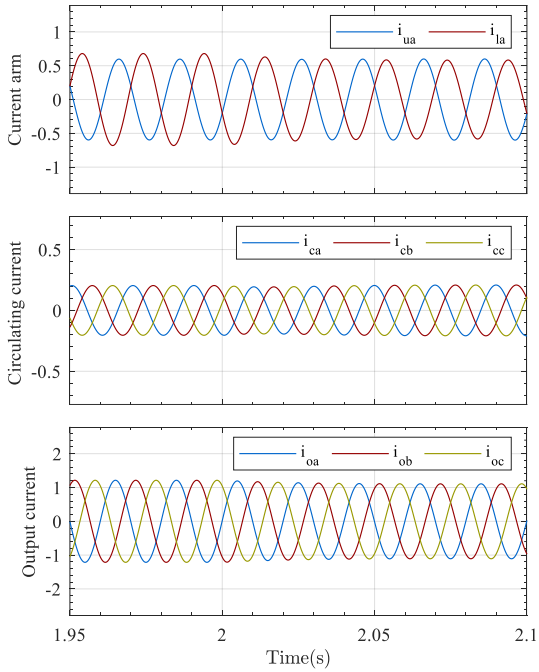

Fig. 4.16 Simulation results of third irradiation step using the quadrature voltage compensation. Current arms, circulating current and output current

As already pointed out, the capability to operate at different power imbalances is not possible if we only use the circulating current i_{cq}. According to (4.17) and (4.18), the tailored power compensation is possible with the local control which phase shifts the output voltage by changing $v_{oq,k}$. According to the control diagram illustrated in Fig. 4.13, when there is a power imbalance, the quadrature voltage compensation changes the modulation index through a dc voltage control loop. Fig. 4.17 shows how the three events described before affected the modulation index in all modules.

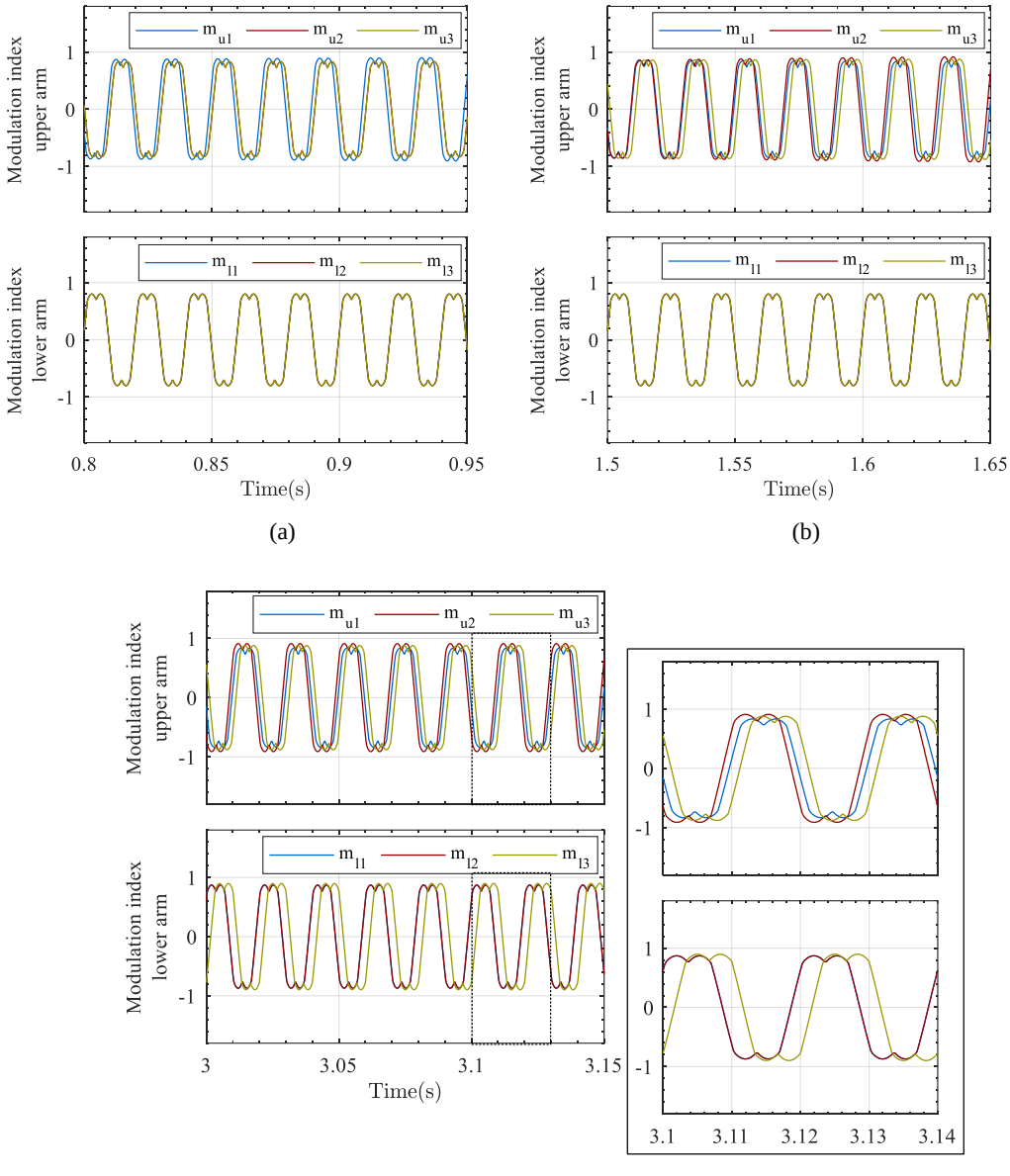

Fig. 4.17 Simulation results of modulation indexes in modules of upper and lower arms under irradiation steps. (a) Event 1, (b) Event 2, (c) Event 3

Modulation index reaction after the first event happened is illustrated in Fig. 4.17.a. Due to the power decrease in module M_{u1}, the modulation index m_{u1} was brought forward to compensate such power difference. However, modulation indexes m_{u2} and m_{u3} were in phase with similar amplitudes as they operated at the same power level. In the second event, module M_{u2} decreased its power, so the modulation index in all modules of the upper arm changed to compensate the power difference as seen in Fig. 4.17.b. Because all modules of the lower arm operated at the same power level, their modulation index did not change.

Similar to previous scenarios, the power decrease in M_{l3} led to a phase shift of the modulation index m_{l3} as seen in Fig. 4.17.c. A zoom of the modulation indexes after the third event happened shows how modules of the upper arm had different amplitude and phase angles, while modules of the lower arm were affected depending on their power difference. Because modules M_{l1} and M_{l2} generated the same power level, they were in phase.

An important aspect has to be mentioned when comparing the amplitude and quadrature voltage compensation. In the amplitude voltage compensation, the first module of the upper arm reached its maximum modulation index after the irradiation steps. However, in the quadrature voltage compensation no module reached its overmodulation even though similar irradiation steps were used. This difference demonstrates how the quadrature voltage compensation provides a higher capability to withstand power imbalances, but at the expense of introducing a circulating current i_{cq} flowing through the arms.

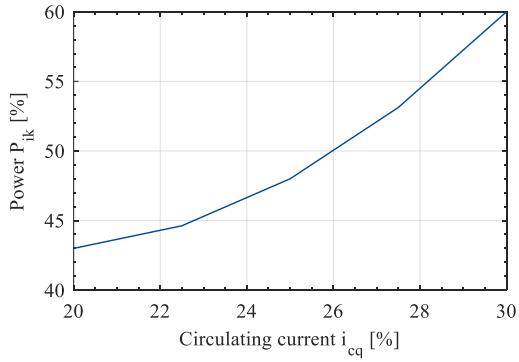

Fig. 4.18 Maximum power imbalance affordable under different circulating current levels

In order to evaluate the maximum capability of the quadrature voltage compensation, Fig. 4.18 shows the maximum power imbalance affordable under specific circulating current levels. We can see that as the circulating current increases, the capability to withstand power imbalances also increases. When the circulating current was 25%, the

maximum power imbalance was 48%, that means 8% higher than the amplitude voltage compensation. For a circulating current of 30% the nominal current arm, the maximum power compensation was close to 60%.

4.3.3 Experimental results

The hardware setup used to evaluate the quadrature voltage compensation has a nominal power of 4.8 kW and two modules per arm. Remember that the PV panels are emulated between the maximum power level and the open circuit operation through an external dc source connected to dc resistors. More details about the hardware setup and its parameters are described in Appendix A.

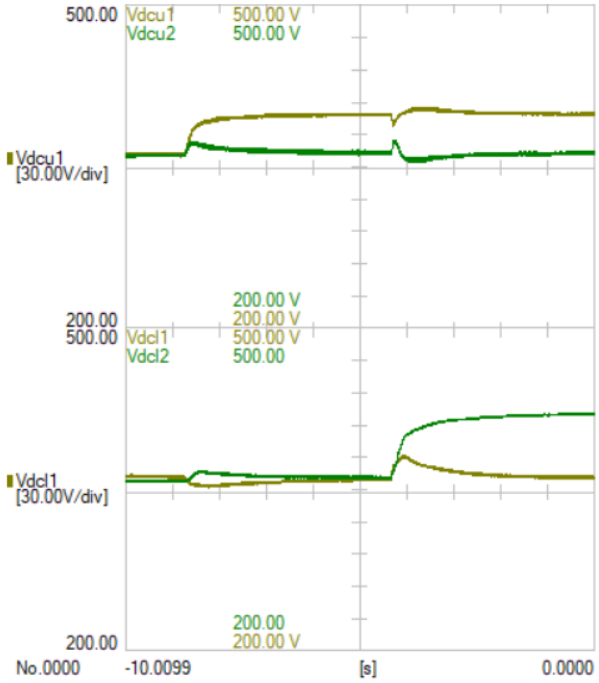

Fig. 4.19 Experimental results of dc voltage steps in modules of upper and lower arms using the quadrature voltage compensation

The experimental setup started with all modules providing their nominal power. During this state, the power generated by each module was 1.2 kW with a dc voltage equal to 360 V. To evaluate the performance of the quadrature voltage compensation, two dc voltage steps were introduced. The first voltage step was set in module M_{u1} of the upper arm, while the second voltage step was introduced in module M_{l2} of the lower arm, providing a

complete imbalance scenario. In the first event the dc voltage v_{dcu1} increased in 40 V as seen in Fig. 4.19, giving rise to a power decrease of 510 W. To withstand this power difference, a circulating current i_{cq} was set in the central control, so the phase angle between the current arms changed.

Fig. 4.20 illustrates the dynamic response of one phase of the current arms and the three-phases of the circulating current when the dc voltage $v_{dcu,1}$ increased. Before the voltage step was applied, the current arms were shifted 180º with similar amplitude levels. However, the increase of the circulating current i_{cq} phase shifted both current arms. The circulating current was intentionally set at 35% the nominal current, creating an angle difference of 61º. Additionally, the power change in M_{u1} reduced the amplitude of the current arm i_{ua}, increasing the circulating current i_{cd}.

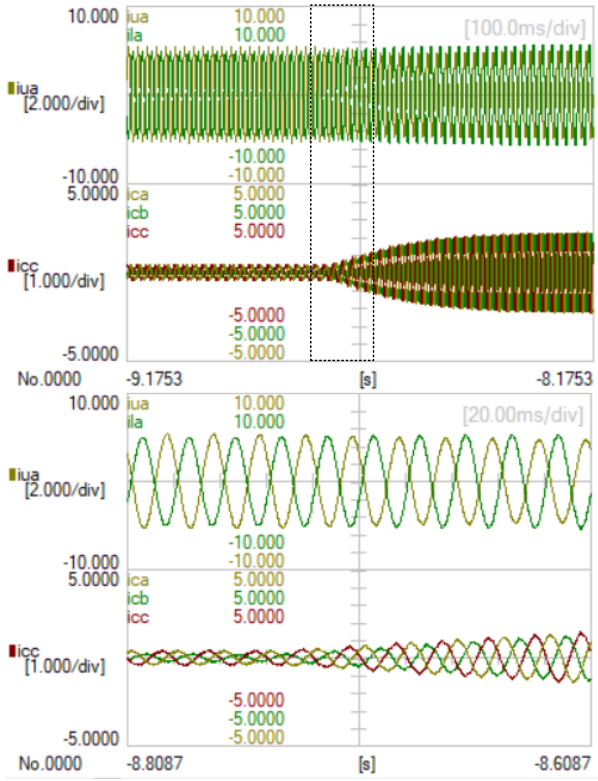

Fig. 4.20 Experimental results of first event. Current arm and circulating current using the quadrature voltage compensation

To evaluate the maximum capability of the quadrature voltage compensation to withstand different power imbalances, the second voltage step introduced in module M_{l2}

was set to 60 V, increasing the dc voltage level from 360 V to 420 V. This large voltage difference illustrated in Fig. 4.19 created a power decrease of 810 W in module M_{l2}, that means 67% of its nominal power. Remember that the maximum power imbalance is achieved when the modulation index is equal to 1.

The effect of the second voltage step on the current arms is illustrated in Fig. 4.21. Before the second event happened, the current in the upper and lower arms had an angle difference defined by the circulating current i_{cq} and an amplitude difference due to the power imbalance introduced in the first event. After the voltage $v_{dcl,2}$ increased, the current in the lower arm was considerably reduced. A zoom of the current signals shows how the current i_{la} reached an amplitude level lower than the current i_{ua}. This current difference increased the circulating current i_{cd} as seen in Fig. 4.21. Because the circulating current i_{cq} remained as in the previous event, the angle difference did not change.

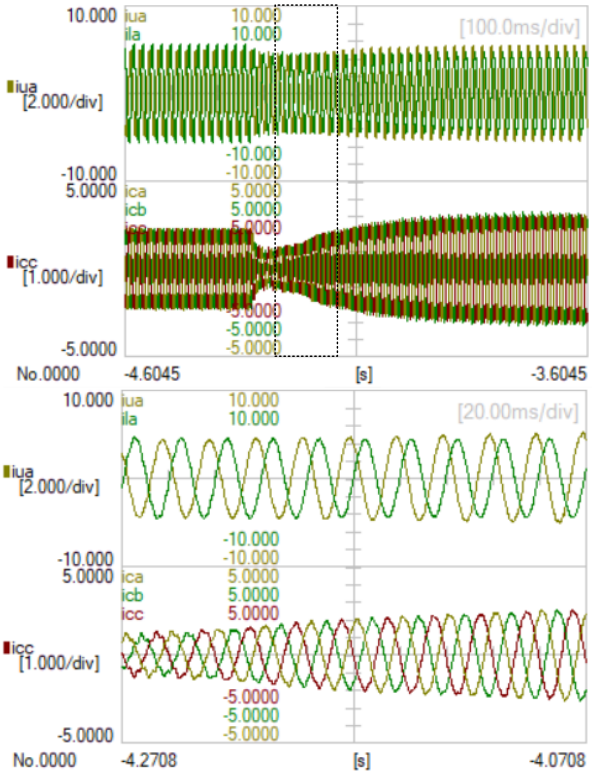

Fig. 4.21 Experimental results of second event. Current arm and circulating current using the quadrature voltage compensation

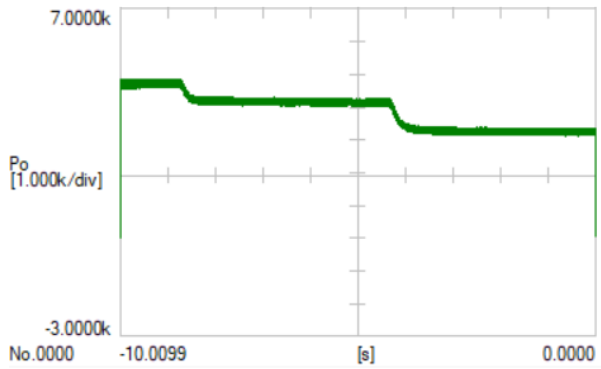

Fig. 4.22 Experimental result of active power using the quadrature voltage compensation

Finally, the power response of both events are illustrated in Fig. 4.22. It is observed how the voltage steps reduced the total power delivered into the grid. After the first event, the power decreased in 510 W and after the second event, the power decreased in 810 W.

4.4 Combination of both control strategies

In previous sections we presented two possible control strategies to withstand different power imbalances between modules of the same arm. In the amplitude voltage compensation, the power flow is controlled by changing the voltage amplitude in the output terminals. So, modules with higher power level increase their amplitude, while modules with lower power reduce their amplitude. On the other hand, the quadrature voltage compensation is able to withstand power imbalances by combining a circulating current i_{cq} with a phase angle in the output voltage. This control strategy demonstrated a higher flexibility to control the power flow as the compensation is given by either changing the q component of the current arm or the phase angle $\gamma_{vi,k}$. Even though, the quadrature voltage compensation allows larger power imbalances, it requires a circulating current which may increase the power losses in the converter.

By combining both control strategies, it is possible to extend the range of operation, providing a higher capability to withstand power imbalances. As pointing out in equations (4.15) and (4.25), the maximum level of power compensation is given by the overmodulation. The idea is to adjust at the same time the dq components of the modulation index, so the limitation provided by one component can be mitigated using the second component. Fig. 4.23 illustrates the concept of combining both control strategies in the local control. The output voltage $v_{i,k}$ is defined based on its dq components, which determine the phase angle $\gamma_{vi.k}$. For instance, if the modulation index $m_{id,k}$ decreases, the output

voltage $v_{id,k}$ also decreases. This can affect the phase angle depending on the voltage level of $v_{iq,k}$. When $v_{iq,k}$ maintains the same value, a change of $v_{id,k}$ will increase the phase angle $\gamma_{vi,k}$, reducing the power provided by module *k*. However, the same result can be achieved by increasing the voltage component $v_{iq,k}$, while keeping the same value of $v_{id,k}$. In a second case, it can be necessary to increase the power flow, so the angle difference between the current arm and the output voltage has to decrease. This requirement can be achieved by either increasing the voltage $v_{id,k}$ or reducing the voltage $v_{iq,k}$.

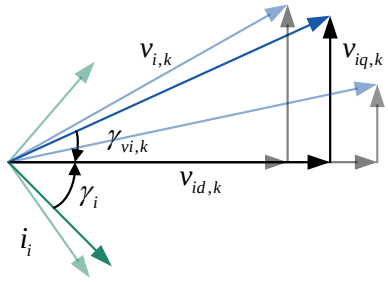

Fig. 4.23 Combination of amplitude and quadrature voltage compensation in one module

As can be seen, there are many options to provide the appropriate power compensation. From Fig. 4.23 we can conclude that when the current arm has an inductive behavior, an increase in the phase angle will reduce the power level. However, when the current arm has a capacitive behavior, the same power can be achieved by increasing the phase angle.

On that basis, it is possible to define each component of the modulation index according to the expressions defined in sections 4.2 and 4.3.

$$\begin{aligned} m_{od,k} &= m_{od} + \Delta m_{id,k} \\ m_{oq,k} &= m_{oq} + \Delta m_{iq,k} \end{aligned} \tag{4.26}$$

The benefit of combining both control strategies can be studied with the analysis of the power response illustrated in Fig. 4.24. The analysis evaluates three different scenarios, with the x-axis representing the power compensation provided by one module and the y-axis representing the modulation index formed by its average value given by the central control plus the compensation given by the local control. As we know, the power compensation can be affected by two main factors: the amplitude of the output voltage and the angle difference between the current arm and the output voltage. In the analysis, different values of circulating current i_{cq} are applied to change the phase angle, affecting the level of $\Delta m_{iq,k}$ required to compensate a certain power.

In the first case, the compensation $m_{id,k}$ is intentionally set to zero, so the power response is only affected by the quadrature voltage compensation. Note that the initial value of the modulation index is set to 0.8. When the circulating current i_{cq} is equal to zero, no matter the value of $\Delta m_{iq,k}$, the power compensation does not change as seen in all scenarios of Fig. 4.24. However, as the circulating current increases, the capability to withstand different levels of power gets higher while the modulation $\Delta m_{iq,k}$ increases. For a circulating current i_{cq} equal to 0.1 pu, the maximum compensation before overmodulation is 18% of the nominal power. But, for a circulating current equal to 0.3 pu, the maximum power compensation is 58%.

Introducing the amplitude voltage compensation, it is clearly observed the wide range of operation. For $\Delta m_{id,k}$ equal to -0.1, the power compensation starts at 12.5% and as the modulation index $\Delta m_{iq,k}$ increases, the power compensation gets higher. Considering a circulating current of 0.1 pu, the maximum power achieved before overmodulation is 35%, that means 17% more power compared to the previous scenario. When the circulating current increases to 0.3 pu, the maximum power compensation is 78%. Note that the compensation provided by $\Delta m_{id,k}$ reduces the initial value of the modulation index. This behavior help us to increases the capability to withstand higher power levels. A similar result can be achieved by decreasing the phase angle $\gamma_{vi,k}$.

In the third study case, the amplitude voltage compensation provides a modulation $\Delta m_{id,k}$ equal to -0.15, so the initial power compensation starts at 18.7% as seen in Fig. 4.24.c. Compared to the previous case, where the modulation index $\Delta m_{id,k}$ was -0.1, the initial power compensation increased in 6.2%. When the circulating current is equal to 0.1 pu, the maximum power compensation before overmodulation is 42%, that means 7% more power than previous case. However, when the circulating current is 0.3 pu, the maximum power compensation before overmodulation is almost 90%. Compared to the first case where the local control was only based on the quadrature voltage compensation, the capability to tolerate power imbalances increased in more than 30%.

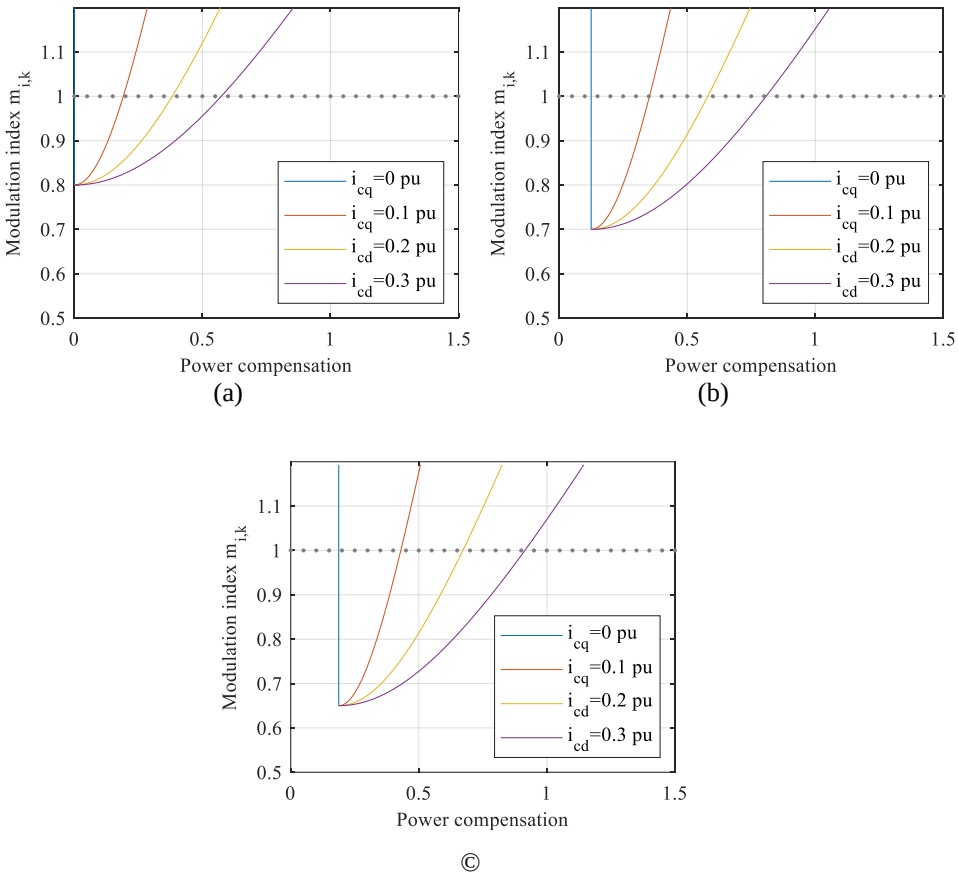

Fig. 4.24 Power response using the amplitude and quadrature voltage compensation. (a) Analysis based on $\Delta m_{id,k} = 0$, (b) Analysis based on $\Delta m_{id,k} = -0.1$, (c) Analysis based on $\Delta m_{id,k} = -0.15$

4.4.1 Experimental results

To evaluate the performance when combining both control strategies, experimental results are presented in this section. The setup used has the same characteristics described in section 4.2 and 4.3. A detail information of the converter, including its architecture and control parameters are found in Appendix A.

Similar to the analysis presented in experimental results of previous sections, two dc voltage steps were introduced to decrease the power provided by module M_{u1} of the upper arm and module M_{l2} of the lower arm. The idea was to validate the capability to withstand

higher power levels compared to the amplitude and quadrature voltage compensation when working individually. Fig. 4.25 illustrates the steady and dynamic state operation of the dc voltages. In the initial state all modules operated at nominal power, providing 1.2 kW with a dc voltage equal to 360 V. In the first event, the dc voltage reference of module M_{u1} increased from 360 V to 400 V as seen in Fig. 4.25. This voltage increase demanded a circulating current i_{cq} to compensate the power change when using the quadrature voltage compensation. To make a fair comparison, the circulating current was intentionally set at 0.35 pu, introducing a phase shift between the current arms

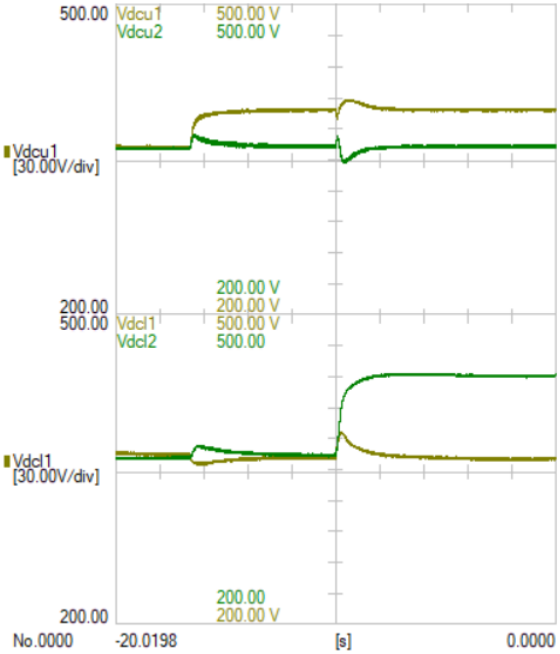

Fig. 4.25 Experimental results of dc voltage steps in modules M_{u1} and M_{l2} using the amplitude and quadrature voltage compensation

Fig. 4.26 illustrates the current arm of phase *a* before and after the dc voltage step took place. In balance operation, both current were shifted in 180º, however, the circulating current i_{cq} triggered a phase shifts of 61º. Additionally, due to the power decrease in module M_{u1}, the current amplitude of the upper arm also decreased.

In the second scenario, module M_{l2} of the lower arm increased drastically its dc voltage from 360 V to 440 V. Remember that the external dc voltage source represents a PV panel working between the maximum power and the open circuit operation, being 360 V when the module provides its maximum power and 440 V when the module operates at open

circuit. Therefore, by increasing the dc voltage reference from 360 V to 440 V, module M_{12} decreased its power operation from 1.2 kW to zero. The impact of the large voltage step on module M_{12} is illustrated in Fig. 4.25. It is shown how the converter was capable to withstand the large voltage difference due to the combination of both control strategies.

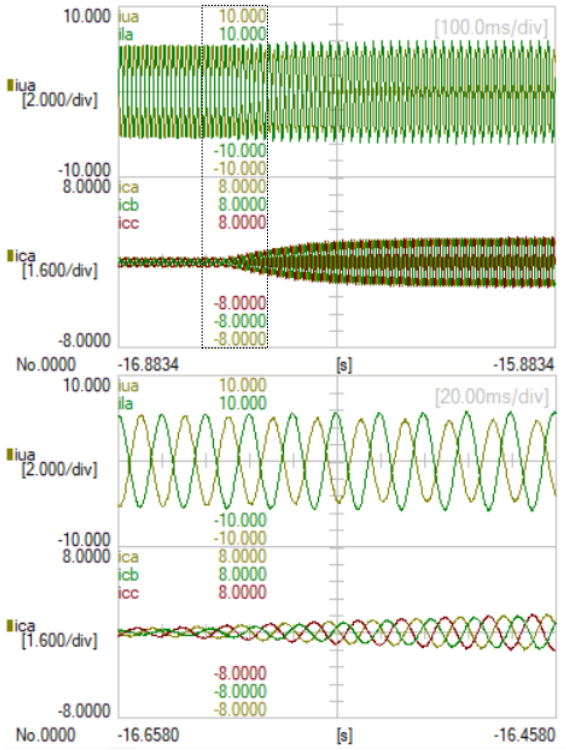

Fig. 4.26 Experimental results of first event based on the amplitude and quadrature voltage compensation. Current arm and circulating current

The power decrease in the lower arm created an increase of the circulating current i_{cd} as seen in Fig. 4.27. Note that the circulating current i_{cq} remained as before (0.35 pu). Compared to the quadrature voltage compensation working individually, the same circulating current i_{cq} allowed a maximum power compensation of 67%. In this case, the combination of both control strategies allowed a power decrease of 100%. The large dc voltage step affected the output current delivered to the grid, decreasing its amplitude level from 9.1 A to 5.8. A similar effect can also be observed in the output power. In Fig. 4.28 it is shown how the active power decreased from 4.8 kW to 4.25 kW after the first voltage step and to 2.9 kW after the second voltage step.

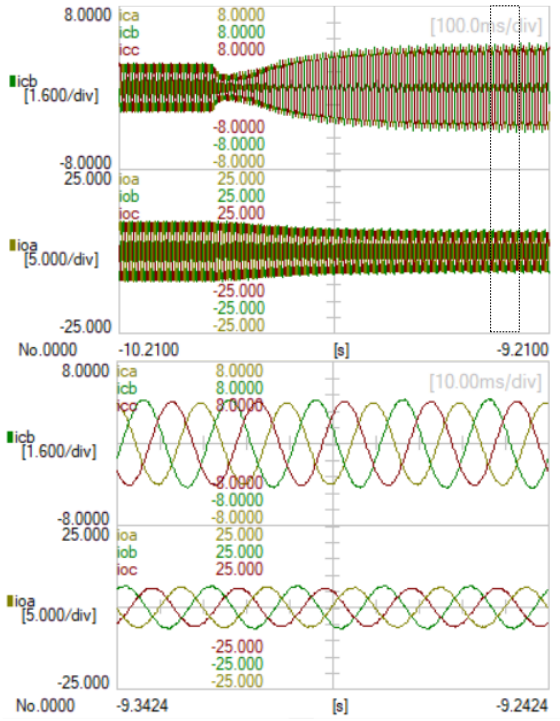

Fig. 4.27 Experimental results of second event based on the amplitude and quadrature voltage compensation. Circulating and output current

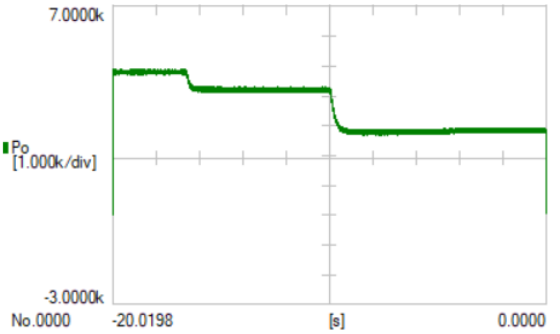

Fig. 4.28 Experimental result of active power using the amplitude and quadrature voltage compensation

4.5 Summary of the chapter

This chapter presented the local control algorithm required to operate under different power imbalances between modules of the same arm. In this approach, the average

modulation index provided by the central control is tailored by each module based on their voltage and power levels. To achieve this goal, two possible control strategies were described based on the well-known representation of the active power, which considers the relationship between the current arm and the output voltage.

In the first control strategy, the amplitude voltage compensation was proposed to regulate the voltage amplitude through the *d* component of the modulation index. A dc voltage control loop is used to generate the proper compensation which increases the modulation index in modules with higher power level and reduces it in modules with lower power. Similarly, the quadrature voltage compensation was proposed to regulate the angle difference between the current arm and the output voltage. By introducing a circulating current i_{cq} in the central control, it was possible to shift the angle of the current arm. Additionally, a dc voltage controller embedded in each module was required to change the phase angle of the output voltage. We demonstrated that by using the quadrature voltage compensation, higher power imbalances are possible, as the power compensation can be achieved by either increasing the circulating current i_{cq} or the *q* component of the output voltage. However, high level of circulating current may increase the converter losses.

Besides working both control strategies individually, it is possible to combine them, so higher levels of power imbalances can be tolerated.

The proposed methods were validated in simulation by implementing the same environment used in previous chapter. However, different scenarios were running in order to provide power imbalances between modules of the same arm. Additionally, experimental results based on a downscale testbench with two modules per arm were presented to evaluate the three possible configurations. The results demonstrated that the combination of both control strategies can be used to compensate a certain power level with a small circulating current when compared with the quadrature voltage compensation.

Chapter 5.

Conclusions and future work

5.1 Conclusions

The work presented in this PhD dissertation was focused on the description, analysis and validation of the three-phase Isolated Multi Modular Converter (IMMC). The IMMC combines a cascaded architecture with several modules connected to increase the voltage level in its terminals and a parallel connection between two arms to provide a higher power rating and flexibility to withstand energy imbalances.

The converter proposed has been used in PV applications where galvanic isolation is an important concern to avoid leakage currents and high floating voltages. Taking the advantages of multilevel converters and the requirements of PV systems into consideration, the challenges and ideas proposed guided us to develop the configuration described in this PhD dissertation.

An analysis of multilevel converters with galvanic isolation in the dc and ac side was first evaluated to propose the IMMC which combines the concept of cascaded converters with ac transformers. The advantages of CTMIs and the well-known modular multilevel converter gave us the idea to develop the configuration proposed, which satisfies the minimum requirements of PV applications in terms of insulation constraints and power imbalance operation. As described in Chapter 2, we introduced the operating principle and

the design considerations for the single-phase IMMC that combines the dynamic response of the current and voltage signals in order to provide a generic and flexible model. Afterward, based on a similar approach, we introduced the three-phase configuration in matrix form, demonstrating with a simple mathematical analysis the behavior of the converter in term of two independent electrical circuits. The fact that two arms are connected in parallel might bring about a circulating current inside the converter when a power imbalance arises. Considering this condition, the generic model was represented based on equivalent models. These components determine the internal dynamics of the IMMC, while the energy response defines the proper references to control the power flow. Thus, a power analysis based on the dc voltages was also studied. The combination of both models covered the first purpose of this dissertation.

Once we developed the generic model for the single and three-phase IMMC, a control architecture to regulate the current and dc voltages was proposed. This control has a cascaded configuration with inner loops to control the current signals and outer loops to control the dc voltages. This is reflected in the analysis introduced in Chapter 3. Additionally, a control strategy based on the traditional cross-over frequency and phase margin technique was introduced to determine the optimal parameters in all controllers. Through the complementary and load sensitivity functions, we demonstrated satisfactory results, providing a stable solution to run the converter under dynamic and steady state scenarios.

The inner controllers regulate the output and circulating currents, while the external controllers determine the total energy per arm. This energy contemplates the sum of all modules, without differentiate between energy levels of consecutive modules. Even though, this is not a realistic case as modules may be connected to individual PV strings with different operating points, this control is focused on the total energy response and not in the energy imbalance operation inside the arm. Through the current controllers we define the general modulation index, representing the series connection of modules as a single unit. In order to work property, it would require a second control unit to restore the dc voltage level back to its reference after external conditions trigger imbalance states. The control proposed was implemented in a *dq* synchronous reference frame, so all minimum needs such as PI controllers and the PLL were introduced to work successfully under this scenario. The performance of the central control was validated through several simulation scenarios. However, taking the limitation mentioned into account, three modules per arm were used, but working with the same dc voltage and power levels. The results demonstrated that the

converter could operate under nominal conditions and power imbalances between arms, but not between modules of the same arm.

During the control design, it became clear that a second control strategy was required to allow power imbalances between modules of the same arm. So, each module can control its dc voltage and power level individually. The deployment of this second control loop is based on the power analysis introduced in Chapter 4, where the power delivered to the grid can be analyzed in terms of the output voltage of each module and the current arm. The analysis presented demonstrated that the power is affected by two different components: the output voltage amplitude and the phase angle between the voltage and current signal, so two different approaches could be introduced to withstand power imbalances. In the first approach, the control strategy used was aimed at controlling the output voltage amplitude, while maintaining a constant phase angle. This strategy called amplitude voltage compensation is embedded in each module, so the modulation index provided by the central control can be individually adapted based on the power and voltage requirements. We demonstrated that during similar conditions, the series connection of modules maintain a similar modulation index amplitude. However, as the power imbalance increases, the difference between the amplitudes becomes larger. The analysis demonstrated that modules with lower power reduces their modulation index, while modules with higher power level increases the modulation index. Nevertheless, this control strategy registered a low capability to tolerate power imbalances. Therefore, small power differences can be tolerated. In order to evaluate the dynamic and steady state operation of this approach, simulation and experimental results were conducted, validating the analysis introduced.

The limitation registered in the amplitude voltage compensation demanded the requirement of another approach to operate under larger power imbalances. So, the second degree of freedom provided by the power analysis was used. This control strategy called quadrature voltage compensation controls the angle difference between the output voltage and the current arm through the q component of the circulating current given by the central control and the phase angle of the output voltage generated in a local control. Because the d component of the modulation index is related to the voltage amplitude, the phase angle is given by the compensation in its q component. Through a simple analysis, we demonstrated that higher levels of power can be tolerated by either increasing the q component of the circulating current or the q component of the modulation index. However, higher levels of circulating current may increase the current losses of the converter, while lower current levels will demand higher levels of compensation in the modulation index. This last scenario could decrease the capability to withstand power imbalances when modules operate close

to their overmodulation level. After the analysis conducted, it was proposed to combine both control strategies, so each module was able to regulate its power flow through the amplitude and phase angle of the output voltage at the same time. The analysis demonstrated that by using this approach, higher levels of power compensation can be allowed with small levels of circulating current. Through simulation and experimental results, it was corroborated the analysis introduced. Demonstrating that modules can operate at different power and voltage levels.

Overall, this dissertation attempted to develop a multilevel converter with galvanic isolation which can be used for PV applications. Additionally, in order to achieve different operating condition with the capacity to withstand imbalance power levels, a hierarchical control architecture was developed and validated through simulation and experimental results. While we were able to cover several aspects regarding the operation of the IMMC, some points we did not get to approach in this thesis, however, we think that they are essential for the real implementation of the complete system. These points are described in next section.

5.2 Future works

As discussed in previous chapters, the IMMC has a cascaded configuration with modules connected through ac transformers. In the literature it was demonstrated that even though low frequency transformers are bulky and less efficient that high frequency transformers, they can provide positive results. Therefore, as implemented in CTMI configurations, the IMMC was proposed based on low frequency transformers. However, an important aspect that was completely left out of the scope are the power losses. When these transformers are connected to high frequency sources, high losses may arise. This problem not only impact on the performance of the converter, but also its reliability. In order to solve this issue, it is necessary to analyze emerging manufacturing technologies of transformers which are able to operate with higher frequencies. Typical core material of classical low frequency transformers is based on grain oriented electrical steel (GOES). However, investigations in different materials such as iron alloys have been proposed to increase their permeability. This is the case of Metglas 2605SA, which is focused on distributed transformers, providing low core losses and high permeability. Having this solution in mind, it may be interesting to evaluate their performance.

Focusing on the same aspect, it would be interesting to investigate other kind of transformers such as medium frequency or multi-winding configurations. In the last one, a single core can be used while the series connection of modules is performed through the

windings round it. This configuration can reduce the equivalent transformer size along with implementation costs.

One of the features about CTMI configurations, is the possibility to operate with asymmetrical voltage levels. In this regard, different numbers of turn ratios can be used in the transformers to increases the number of stepped voltages. As mentioned, a symmetric configuration generates $2k + 1$ number of levels, however, a binary or ternary geometric progression reach up to $2^{k+1} + 1$ or 3^k levels respectively. This approach will contribute to reduce the base frequency of each module, while maintaining a certain equivalent frequency in the output voltage.

Another aspect that was left out is the effect of communication delays. Because the IMMC has a cascaded configuration, a reliable synchronization among all modules and a robust communication between the central and local controllers is absolutely necessary. Although, it is possible to find high speed communication buses, in order to fulfill this requirement, we need to evaluate the effect of communication delays and propose possible solutions to compensate them.

The impact of renewable energies has significantly increased during the last years, the lack of inertia in these primary sources may reduce the grid stability, increasing its vulnerability under frequency changes. Many studies have been proposed to compensate this issue in the past, providing successful results. Because the IMMC is intended to be connected to PV applications, it would be interesting to evaluate control strategies such as virtual synchronous generators in combination with the control architecture proposed in order to provide grid auxiliary services.

References

[1] International Renewable Energy Agency, *Global Renewables Outlook: Energy transformation 2050*. 2020.

[2] IRENA, *Future of Photovoltaic - deployment, investment, technology, grid integration and socio-economic aspects*. 2019.

[3] Kusch-Brandt, *Renewables 2019 Global Status Report*, vol. 8, no. 3. 2019.

[4] A. Cabrera-Tobar, E. Bullich-Massagué, M. Aragüés-Peñalba, and O. Gomis-Bellmunt, "Topologies for large scale photovoltaic power plants," *Renew. Sustain. Energy Rev.*, vol. 59, pp. 309–319, 2016.

[5] M. Şenol, S. Abbasoğlu, O. Kükrer, and A. A. Babatunde, "A guide in installing large-scale PV power plant for self consumption mechanism," *Sol. Energy*, vol. 132, pp. 518–537, 2016.

[6] A. Cabrera-Tobar, E. Bullich-Massagué, M. Aragüés-Peñalba, and O. Gomis-Bellmunt, "Review of advanced grid requirements for the integration of large scale photovoltaic power plants in the transmission system," *Renew. Sustain. Energy Rev.*, vol. 62, pp. 971–987, 2016.

[7] L. Hassaine, E. Olias, J. Quintero, and V. Salas, "Overview of power inverter topologies and control structures for grid connected photovoltaic systems," *Renew. Sustain. Energy Rev.*, vol. 30, pp. 796–807, 2014.

[8] R. Shah, N. Mithulananthan, R. C. Bansal, and V. K. Ramachandaramurthy, "A review of key power system stability challenges for large-scale PV integration," *Renew. Sustain. Energy Rev.*, vol. 41, pp. 1423–1436, 2015.

[9] S. Kouro, J. I. Leon, D. Vinnikov, and L. G. Franquelo, "Grid-connected photovoltaic systems: An overview of recent research and emerging PV converter technology," *IEEE Ind. Electron. Mag.*, vol. 9, no. 1, pp. 47–61, 2015.

[10] E. Bullich-Massagué, R. Ferrer-San-josé, M. Aragüés-Peñalba, L. Serrano-Salamanca, C. Pacheco-Navas, and O. Gomis-Bellmunt, "Power plant control in

large-scale photovoltaic plants: Design, implementation and validation in a 9.4 MW photovoltaic plant," *IET Renew. Power Gener.*, vol. 10, no. 1, pp. 50–62, 2016.

[11] E. X. Dan Xu, Chen Du and T. T. Frp, "Research and Simulation Analysis of Control Strategies for the Large-Scale Grid-Connected Photovoltaic System."

[12] J. Rodríguez, J. S. Lai, and F. Z. Peng, "Multilevel inverters: A survey of topologies, controls, and applications," *IEEE Trans. Ind. Electron.*, vol. 49, no. 4, pp. 724–738, 2002.

[13] J. Rodríguez, S. Bernet, B. Wu, J. O. Pontt, and S. Kouro, "Multilevel voltage-source-converter topologies for industrial medium-voltage drives," *IEEE Trans. Ind. Electron.*, vol. 54, no. 6, pp. 2930–2945, 2007.

[14] M. Malinowski, K. Gopakumar, J. Rodriguez, and M. A. Perez, "A survey on cascaded multilevel inverters," *IEEE Trans. Ind. Electron.*, vol. 57, no. 7, pp. 2197–2206, 2010.

[15] S. Kouro *et al.*, "Recent Advances and Industrial Applications of Multilevel Converters," *IEEE Trans. Ind. Electron.*, vol. 57, no. 8, pp. 2553–2580, 2010.

[16] C. D. Fuentes, C. A. Rojas, H. Renaudineau, S. Kouro, M. A. Perez, and T. Meynard, "Experimental Validation of a Single DC Bus Cascaded H-Bridge Multilevel Inverter for Multistring Photovoltaic Systems," *IEEE Trans. Ind. Electron.*, vol. 64, no. 2, pp. 930–934, 2017.

[17] H. Okumura, "Power electronics innovation by Silicon Carbide power semiconductor devices," *IMFEDK 2014 - 2014 Int. Meet. Futur. Electron Devices, Kansai*, pp. 0–1, 2014.

[18] A. Mantooth, "Devices and Components for New Power Converter Developments," *IEE Power Electron. Mag.*, no. June, pp. 53–56, 2016.

[19] H. Jain, S. Rajawat, and P. Agrawal, "Comparision of wide band gap semiconductors for power electronics applications," *2008 Int. Conf. Recent Adv. Microw. Theory Appl. Microw. 2008*, pp. 878–881, 2008.

[20] T. Stiasny *et al.*, "Large area (150mm) high voltage (6.5kV) reverse conducting IGCT," *2017 19th Eur. Conf. Power Electron. Appl. EPE 2017 ECCE Eur.*, vol. 2017-Janua, pp. 1–8, 2017.

[21] H. Abu-Rub, J. Holtz, J. Rodriguez, and G. Baoming, "Medium-voltage multilevel converters State of the art, challenges, and requirements in Industrial applications," *IEEE Trans. Ind. Electron.*, vol. 57, no. 8, pp. 2581–2596, 2010.

[22] J. Rodriguez, S. Member, S. Bernet, P. K. Steimer, and I. E. Lizama, "A Survey on Neutral-Point-Clamped Inverters," vol. 57, no. 7, pp. 2219–2230, 2010.

[23] T. Brückner, S. Bernet, and H. Güldner, "The active NPC converter and its loss-balancing control," *IEEE Trans. Ind. Electron.*, vol. 52, no. 3, pp. 855–868, 2005.

[24] N. Celanovic and D. Boroyevich, "A comprehensive study of neutral-point voltage

balancing problem in three-level neutral-point-clamped voltage source PWM inverters," *IEEE Trans. Power Electron.*, vol. 15, no. 2, pp. 242–249, 2000.

[25] A. New, C. Osawa, and Y. Matsumoto, "A New Neutral-Point-Clamped PWM Inverter," *... 1997., Proc. ...*, vol. I, no. 5, pp. 225–230, 1981.

[26] M. Schweizer and J. W. Kolar, "Design and implementation of a highly efficient three-level T-type converter for low-voltage applications," *IEEE Trans. Power Electron.*, vol. 28, no. 2, pp. 899–907, 2013.

[27] P. Alemi, Y. C. Jeung, and D. C. Lee, "DC-Link capacitance minimization in t-type three-level AC/DC/AC PWM converters," *IEEE Trans. Ind. Electron.*, vol. 62, no. 3, pp. 1382–1391, 2015.

[28] E. Gurpinar and A. Castellazzi, "Single-Phase T-Type Inverter Performance," *IEEE Trans. Power Electron.*, vol. 31, no. 10, pp. 7148–7160, 2016.

[29] S. Busquets-Monge, J. Rocabert, P. Rodríguez, S. Alepuz, and J. Bordonau, "Multilevel diode-clamped converter for photovoltaic generators with independent voltage control of each solar array," *IEEE Trans. Ind. Electron.*, vol. 55, no. 7, pp. 2713–2723, 2008.

[30] S. Mersche, D. Bernet, and M. Hiller, "Quasi-two-level flying-capacitor-converter for medium voltage grid applications," *2019 IEEE Energy Convers. Congr. Expo. ECCE 2019*, pp. 3666–3673, 2019.

[31] W. Li, J. Hu, S. Hu, H. Yang, H. Yang, and X. He, "Capacitor Voltage Balance Control of Five-Level Modular Composited Converter with Hybrid Space Vector Modulation," *IEEE Trans. Power Electron.*, vol. 33, no. 7, pp. 5629–5640, 2018.

[32] Y. Zhang, J. T. Sun, and Y. F. Wang, "Hybrid boost three-level DC-DC converter with high voltage gain for photovoltaic generation systems," *IEEE Trans. Power Electron.*, vol. 28, no. 8, pp. 3659–3664, 2013.

[33] B. P. McGrath and D. G. Holmes, "Multicarrier PWM strategies for multilevel inverters," *IEEE Trans. Ind. Electron.*, vol. 49, no. 4, pp. 858–867, 2002.

[34] N. M. A. Costa, L. C. De Freitas, B. V. João, E. A. A. Coelho, V. J. Farias, and L. C. G. Freitas, "New approach on multilevel cascaded inverters using EIE commutation cells," *2010 IEEE Energy Convers. Congr. Expo. ECCE 2010 - Proc.*, pp. 2127–2132, 2010.

[35] Y. Yu, G. Konstantinou, B. Hredzak, and V. G. Agelidis, "Power Balance Optimization of Cascaded H-Bridge Multilevel Converters for Large-Scale Photovoltaic Integration," *IEEE Trans. Power Electron.*, vol. 31, no. 2, pp. 1108–1120, 2016.

[36] C. D. Townsend, Y. Yu, G. Konstantinou, and V. G. Agelidis, "Cascaded H-Bridge Multilevel PV Topology for Alleviation of Per-Phase Power Imbalances and Reduction of Second Harmonic Voltage Ripple," *IEEE Trans. Power Electron.*, vol. 31, no. 8, pp. 5574–5586, 2016.

[37] Y. Yu, G. Konstantinou, C. D. Townsend, R. P. Aguilera, B. Hredzak, and V. G. Agelidis, “Delta-connected cascaded H-bridge multilevel photovoltaic converters,” *IECON 2015 - 41st Annu. Conf. IEEE Ind. Electron. Soc.*, pp. 2229–2234, 2015.

[38] M. Hagiwara and H. Akagi, “Control and Experiment of Pulsewidth-Modulated Modular Multilevel Converters,” *IEEE Trans. Power Electron.*, vol. 24, no. 7, pp. 1737–1746, 2009.

[39] S. Debnath, J. Qin, B. Bahrani, M. Saeedifard, and P. Barbosa, “Operation, control, and applications of the modular multilevel converter: A review,” *IEEE Trans. Power Electron.*, vol. 30, no. 1, pp. 37–53, 2015.

[40] B. Wu, A. Dekka, N. R. Zargari, R. L. Fuentes, and M. Perez, “Evolution of Topologies, Modeling, Control Schemes, and Applications of Modular Multilevel Converters,” *IEEE J. Emerg. Sel. Top. Power Electron.*, vol. 5, no. 4, pp. 1631–1656, 2017.

[41] P. W. Wheeler, J. Rodríguez, J. C. Clare, L. Empringham, and A. Weinstein, “Matrix converters: A technology review,” *IEEE Trans. Ind. Electron.*, vol. 49, no. 2, pp. 276–288, 2002.

[42] M. Glinka and R. Marquardt, “A new AC/AC multilevel converter family,” *IEEE Trans. Ind. Electron.*, vol. 52, no. 3, pp. 662–669, 2005.

[43] D. Borojević, “Space Vector Modulated Three-Phase to Three-Phase Matrix Converter with Input Power Factor Correction,” *IEEE Trans. Ind. Appl.*, vol. 31, no. 6, pp. 1234–1246, 1995.

[44] E. Serban, M. Ordonez, and C. Pondiche, “DC-Bus Voltage Range Extension in 1500 v Photovoltaic Inverters,” *IEEE J. Emerg. Sel. Top. Power Electron.*, vol. 3, no. 4, pp. 901–917, 2015.

[45] Marchesoni M., Mazzucchelli M.,Tenconi S., “A non Conventional Power Converter for Plasma Stabilization,” p. 400, 316AD.

[46] C. Material, N. Kensington, and C. Der, “a New Approach To Enihance Powier Quality for,” pp. 231–235, 1995.

[47] Y. Yu, G. Konstantinou, B. Hredzak, and V. G. Agelidis, “Power Balance of Cascaded H-Bridge Multilevel Converters for Large-Scale Photovoltaic Integration,” *IEEE Trans. Power Electron.*, vol. 31, no. 1, pp. 292–303, 2016.

[48] S. Mariethoz and A. Rufer, “Design and control of asymmetrical multi-level inverters,” *IECON Proc. (Industrial Electron. Conf.*, vol. 1, pp. 840–845, 2002.

[49] M. Veenstra and A. Rufer, “Control of a hybrid asymmetric multilevel inverter for competitive medium-voltage industrial drives,” *IEEE Trans. Ind. Appl.*, vol. 41, no. 2, pp. 655–664, 2005.

[50] T. Lipo, “Hybrid Topology for Multilevel Power Conversion,” WO99/41828, 1999.

[51] C. A. Rojas, S. Kouro, M. A. Perez, and J. Echeverria, “DC-DC MMC for HVdc

Grid Interface of Utility-Scale Photovoltaic Conversion Systems," *IEEE Trans. Ind. Electron.*, vol. 65, no. 1, pp. 352–362, 2018.

[52] A. Chub, D. Vinnikov, R. Kosenko, and E. Liivik, "Wide Input Voltage Range Photovoltaic Microconverter with Reconfigurable Buck-Boost Switching Stage," *IEEE Trans. Ind. Electron.*, vol. 64, no. 7, pp. 5974–5983, 2017.

[53] K. I. Hwu and T. J. Peng, "A novel buck-boost converter combining KY and buck converters," *IEEE Trans. Power Electron.*, vol. 27, no. 5, pp. 2236–2241, 2012.

[54] A. C. Kyritsis, E. C. Tatakis, and N. P. Papanikolaou, "Optimum design of the current-source flyback inverter for decentralized grid-connected photovoltaic systems," *IEEE Trans. Energy Convers.*, vol. 23, no. 1, pp. 281–293, 2008.

[55] H. K. Jahan, K. Zare, and M. Abapour, "Verification of a Low Component Nine-Level," *IEEE J. Emerg. Sel. Top. Power Electron.*, vol. 6, no. 1, pp. 429–440, 2018.

[56] F. S. Kang, S. J. Park, and C. U. Kim, "Multilevel Inverter Employing Cascaded Transformers," *IECON Proc. (Industrial Electron. Conf.*, vol. 3, pp. 2185–2190, 2003.

[57] A. S. Gadalla, X. Yan, S. Y. Altahir, and H. Hasabelrasul, "Evaluating the capacity of power and energy balance for cascaded H-bridge multilevel inverter using different PWM techniques," *J. Eng.*, vol. 2017, no. 13, pp. 1713–1718, 2017.

[58] N. A. Rahim, M. F. M. Elias, and W. P. Hew, "Transistor-clamped H-bridge based cascaded multilevel inverter with new method of capacitor voltage balancing," *IEEE Trans. Ind. Electron.*, vol. 60, no. 8, pp. 2943–2956, 2013.

[59] F. S. Kang, S. E. Cho, S. J. Park, C. U. Kim, and T. Ise, "A new control scheme of a cascaded transformer type multilevel PWM inverter for a residential photovoltaic power conditioning system," *Sol. Energy*, vol. 78, no. 6, pp. 727–738, 2005.

[60] O. Lopez-Santos, C. A. Jacanamejoy-Jamioy, D. F. Salazar-D'Antonio, J. R. Corredor-Ramirez, G. Garcia, and L. Martinez-Salamero, "A Single-Phase Transformer-Based Cascaded Asymmetric Multilevel Inverter With Balanced Power Distribution," *IEEE Access*, vol. 7, pp. 98182–98196, 2019.

[61] J. Pereda and J. Dixon, "High-frequency link: A solution for using only one DC source in asymmetric cascaded multilevel inverters," *IEEE Trans. Ind. Electron.*, vol. 58, no. 9, pp. 3884–3892, 2011.

[62] A. A. Gandomi, S. Saeidabadi, S. H. Hosseini, E. Babaei, and M. Sabahi, "Transformer-based inverter with reduced number of switches for renewable energy applications," *IET Power Electron.*, vol. 8, no. 10, pp. 1875–1884, 2015.

[63] M. R. Banaei, H. Khounjahan, and E. Salary, "Single-source cascaded transformers multilevel inverter with reduced number of switches," *IET Power Electron.*, vol. 5, no. 9, pp. 1748–1753, 2012.

[64] S. Salehahari, E. Babaei, S. H. Hosseini, and A. Ajami, "Transformer-based multilevel inverters: Analysis, design and implementation," *IET Power Electron.*,

vol. 12, no. 1, pp. 1–10, 2019.

[65] C. B. Jacobina and A. P. Monteiro, “Multilevel Single-Phase PWM Converters with Shared Legs and Cascaded Transformers,” *2019*, pp. 5878–5885, 2019.

[66] N. N. V. Surendra Babu and B. G. Fernandes, “Cascaded two-level inverter-based multilevel STATCOM for high-power applications,” *IEEE Trans. Power Deliv.*, vol. 29, no. 3, pp. 993–1001, 2014.

[67] A. K. Panda and Y. Suresh, “Performance of cascaded multilevel inverter by employing single and three-phase transformers,” *IET Power Electron.*, vol. 5, no. 9, pp. 1694–1705, 2012.

[68] A. Lashab *et al.*, “Cascaded Multilevel PV Inverter with Improved Harmonic Performance During Power Imbalance Between Power Cells,” *IEEE Trans. Ind. Appl.*, vol. 56, no. 3, pp. 1–1, 2020.

[69] T. S. Basu and S. Maiti, “A Hybrid Modular Multilevel Converter for Solar Power Integration,” *IEEE Trans. Ind. Appl.*, vol. 55, no. 5, pp. 5166–5177, 2019.

[70] L. T. Manjrekar Madhav, Steimer Peter, “Hybrid Multilevel Power Conversion System: a competitive solution for high power applications,” pp. 10–17, 1999.

[71] S. Kouro, B. Wu, Á. Moya, E. Villanueva, P. Correa, and J. Rodríguez, “Control of a cascaded H-bridge multilevel converter for grid connection of photovoltaic systems,” *IECON Proc. (Industrial Electron. Conf.*, pp. 3976–3982, 2009.

[72] H. Nademi, A. Das, R. Burgos, and L. E. Norum, “A New Circuit Performance of Modular Multilevel Inverter Suitable for Photovoltaic Conversion Plants,” *IEEE J. Emerg. Sel. Top. Power Electron.*, vol. 4, no. 2, pp. 393–404, 2016.

[73] H. Bayat and A. Yazdani, “A Power Mismatch Elimination Strategy for an MMC-based PV System in Unbalanced Grids,” *2018 IEEE Electr. Power Energy Conf. EPEC 2018*, vol. 33, no. 3, pp. 1519–1528, 2018.

[74] P. Sochor and H. Akagi, “Theoretical comparison in energy-balancing capability between star- and delta-configured modular multilevel cascade inverters for utility-scale photovoltaic systems,” *IEEE Trans. Power Electron.*, vol. 31, no. 3, pp. 1980–1992, 2016.

[75] A. Alexander and M. Thathan, “Modelling and analysis of modular multilevel converter for solar photovoltaic applications to improve power quality,” *IET Renew. Power Gener.*, vol. 9, no. 1, pp. 78–88, 2015.

[76] H. Bayat and A. Yazdani, “A Hybrid MMC-Based Photovoltaic and Battery Energy Storage System,” *IEEE Power Energy Technol. Syst. J.*, vol. 6, no. 1, pp. 32–40, 2019.

[77] P. Wu, W. Huang, and N. Tai, “Novel grid connection interface for utility-scale PV power plants based on MMC,” *J. Eng.*, vol. 2019, no. 16, pp. 2683–2686, 2019.

[78] A. Shahirinia and A. Hajizadeh, “Model Predictive Control of Grid Connected

Modular Multilevel Converter for Integration of Photovoltaic Power Systems," pp. 3092–3095, 2018.

[79] A. Rashwan, "A New Topology for the Large-Scale Photovoltaic Systems Grid Connection Based on Modular Multilevel Converter," *2018 20th Int. Middle East Power Syst. Conf. MEPCON 2018 - Proc.*, pp. 286–291, 2019.

[80] M. A. Perez, D. Arancibia, S. Kouro, and J. Rodriguez, "Modular multilevel converter with integrated storage for solar photovoltaic applications," *IECON Proc. (Industrial Electron. Conf.*, pp. 6993–6998, 2013.

[81] G. Generator *et al.*, "Modular Multilevel Inverter with New Modulation Method and Its Application to Photovoltaic Grid-Connected Generator," *IEEE Trans. Power Electron.*, vol. 28, no. 11, pp. 5063–5073, 2013.

[82] H. Nademi, A. Elahidoost, and L. E. Norum, "Comparative analysis of different MPPT schemes for photovoltaic integration of modular multilevel converter," *2016 IEEE 17th Work. Control Model. Power Electron. COMPEL 2016*, pp. 1–5, 2016.

[83] F. Rong, X. Gong, and S. Huang, "A Novel Grid-Connected PV System Based on MMC to Get the Maximum Power under Partial Shading Conditions," *IEEE Trans. Power Electron.*, vol. 32, no. 6, pp. 4320–4333, 2017.

[84] K. Shen, D. Zhao, G. Zhao, and S. Wang, "Photovoltaic supplied grid-connected modular multilevel converter with active power injection and reactive power compensation capability," *Proc. IECON 2017 - 43rd Annu. Conf. IEEE Ind. Electron. Soc.*, vol. 2017-Janua, no. 51507142, pp. 7837–7842, 2017.

[85] M. R. Islam, A. M. Mahfuz-Ur-Rahman, M. M. Islam, Y. G. Guo, and J. G. Zhu, "Modular Medium-Voltage Grid-Connected Converter with Improved Switching Techniques for Solar Photovoltaic Systems," *IEEE Trans. Ind. Electron.*, vol. 64, no. 11, pp. 8887–8896, 2017.

[86] G. J. Kish, M. Ranjram, and P. W. Lehn, "A modular multilevel DC/DC converter with fault blocking capability for HVDC interconnects," *IEEE Trans. Power Electron.*, vol. 30, no. 1, pp. 148–162, 2015.

[87] Y. Chen, Y. Cui, X. Wang, X. Wei, and Y. Kang, "Design and implementation of the low computational burden phase-shifted modulation for DC-DC modular multilevel converter," *IET Power Electron.*, vol. 9, no. 2, pp. 256–269, 2016.

[88] G. P. Adam, I. A. Gowaid, S. J. Finney, D. Holliday, and B. W. Williams, "Review of dc-dc converters for multi-terminal HVDC transmission networks," *IET Power Electron.*, vol. 9, no. 2, pp. 281–296, 2016.

[89] Y. Suresh and A. K. Panda, "Research on a cascaded multilevel inverter by employing three-phase transformers," *IET Power Electron.*, vol. 5, no. 5, pp. 561–570, 2012.

[90] S. J. Park, F. S. Kang, S. E. Cho, C. J. Moon, and H. K. Nam, "A novel switching strategy for improving modularity and manufacturability of cascaded-transformer-

based multilevel inverters," *Electr. Power Syst. Res.*, vol. 74, no. 3, pp. 409–416, 2005.

[91] H. S. Krishnamoorthy, S. Essakiappan, P. N. Enjeti, R. S. Balog, and S. Ahmed, "A new multilevel converter for megawatt scale solar photovoltaic utility integration," *Conf. Proc. - IEEE Appl. Power Electron. Conf. Expo. - APEC*, pp. 1431–1438, 2012.

[92] F. Z. Peng and J. Wang, "A universal STATCOM with delta-connected cascade multilevel inverter," *PESC Rec. - IEEE Annu. Power Electron. Spec. Conf.*, vol. 5, pp. 3529–3533, 2004.

[93] S. G. Song, F. S. Kang, and S. J. Park, "Cascaded multilevel inverter employing three-phase transformers and single DC input," *IEEE Trans. Ind. Electron.*, vol. 56, no. 6, pp. 2005–2014, 2009.

[94] E. C. Topology and B. M. Inverter, "Performance of Cascade Multilevel H-Bridge Inverter with Single DC Source by Employing Low Frequency Three-Phase Transformers," *Electr. Eng.*, pp. 1975–1980, 2010.

[95] G. A. De Almeida Carlos, C. B. Jacobina, J. P. R. A. Méllo, and E. C. Dos Santos, "Cascaded Open-End Winding Transformer Based DVR," *IEEE Trans. Ind. Appl.*, vol. 54, no. 2, pp. 1490–1501, 2018.

[96] H. K. Jahan, M. Naseri, M. M. Haji-Esmaeili, M. Abapour, and K. Zare, "Low component merged cells cascaded-transformer multilevel inverter featuring an enhanced reliability," *IET Power Electron.*, vol. 10, no. 8, pp. 855–862, 2017.

[97] S. Behara, N. Sandeep, and U. R. Yaragatti, "Design and Implementation of Transformer-Based Multilevel Inverter Topology with Reduced Components," *IEEE Trans. Ind. Appl.*, vol. 54, no. 5, pp. 4632–4639, 2018.

[98] S. Park, "Half-bridge and Full-bridge Cell based Multilevel PWM Inverter with Cascaded Transformers," pp. 273–276.

[99] J. P. R. A. Mello, C. B. Jacobina, and M. B. De Rossiter Correa, "Three-Phase Four-Wire Inverters Based on Cascaded Three-Phase Converters with Four and Three Legs," *IEEE Trans. Ind. Appl.*, vol. 53, no. 6, pp. 5539–5552, 2017.

[100] K. Komoto *et al.*, *Energy from the Desert: Very Large Scale PV Power Plants for Shifting to Renewable Energy Future*, no. IEA PVPS T8-01:2015. 2015.

[101] S. Rohner, S. Bernet, M. Hiller, and R. Sommer, "Analysis and simulation of a 6 kV, 6MVA modular multilevel converter," *IECON Proc. (Industrial Electron. Conf.*, pp. 225–230, 2009.

[102] B. Wu, *High-Power Converters and AC Drives*. Wiley-Interscience, 2016.

[103] R. Iravani, Yazdani; Amirnaser, *Voltage-Sourced Converters in Power System. Modeling, Control, and Applications*. John Wiley & Sons, 2010.

[104] L. Marin, A. Tarraso, I. Candela, R. Rye, and P. Rodriguez, "Influence of the ICFF

Decoupling Technique on the Stability of the Current Control Loop of a Grid-Tied VSC," *2019 IEEE Energy Convers. Congr. Expo. ECCE 2019*, pp. 2622–2628, 2019.

[105] M. Goodwin, Graham; Graebe, Stefan, Salgado, *Control Systems Design*. Prentice Hall, 2000.

[106] D. G. Holmes, T. A. Lipo, B. P. McGrath, and W. Y. Kong, "Optimized design of stationary frame three phase AC Current regulators," *IEEE Trans. Power Electron.*, vol. 24, no. 11, pp. 2417–2426, 2009.

[107] A. Vidal *et al.*, "Assessment and optimization of the transient response of proportional-resonant current controllers for distributed power generation systems," *IEEE Trans. Ind. Electron.*, vol. 60, no. 4, pp. 1367–1383, 2013.

[108] S. Buso and P. Mattavelli, *Digital control in power electronics*, vol. 2. Morgan &Claypool Publishers, 2006.

[109] J. Z. Zhou, H. Ding, S. Fan, Y. Zhang, and A. M. Gole, "Impact of short-circuit ratio and phase-locked-loop parameters on the small-signal behavior? of a VSC-HVDC converter," *IEEE Trans. Power Deliv.*, vol. 29, no. 5, pp. 2287–2296, 2014.

[110] S. Haghbin and T. Thiringer, "DC bus current harmonics of a three-phase PWM inverter with the zero sequence injection," *2014 IEEE Transp. Electrif. Conf. Expo Components, Syst. Power Electron. - From Technol. to Bus. Public Policy, ITEC 2014*, 2014.

[111] G. Hsieh, "Phase-Locked Loop Techniques-A Survey," vol. 43, no. 6, 1996.

[112] P. Teodorescu, Remus; Liserre, Marco; Rodriguez, *Grid Converters for Photovoltaic and Photovoltaic and*, John Wiley. 2011.

[113] M. Ciobotaru, R. Teodorescu, and F. Blaabjerg, "A new single-phase PLL structure based on second order generalized integrator," *PESC Rec. - IEEE Annu. Power Electron. Spec. Conf.*, 2006.

[114] S. Golestan and J. M. Guerrero, "Conventional synchronous reference frame phase-locked loop is an adaptive complex filter," *IEEE Trans. Ind. Electron.*, vol. 62, no. 3, pp. 1679–1682, 2015.

[115] Z. Liu, B. Liu, S. Duan, and Y. Kang, "A Novel DC Capacitor Voltage Balance Control Method for Cascade Multilevel STATCOM," *IEEE Trans. Power Electron.*, vol. 27, no. 1, pp. 14–27, 2012.

[116] C. Verdugo, S. Kouro, M. A. Perez, M. Malinowski, and T. Meynard, "Series-connected T-type Inverters for single-phase grid-connected Photovoltaic Energy System," in *IECON Proceedings (Industrial Electronics Conference)*, 2013.

[117] C. Verdugo, S. Kouro, C. A. Rojas, M. A. Perez, T. Meynard, and M. Malinowski, "Five-level T-type cascade converter for rooftop grid-connected photovoltaic systems," *Energies*, vol. 12, no. 9, pp. 1–20, 2019.

[118] S. Rivera, S. Kouro, B. Wu, J. I. Leon, J. Rodríiguez, and L. G. Franquelo, "Cascaded H-bridge multilevel converter multistring topology for large scale photovoltaic systems," *Proc. - ISIE 2011 2011 IEEE Int. Symp. Ind. Electron.*, pp. 1837–1844, 2011.

[119] Y. Li and B. Wu, "A novel DC voltage detection technique in the CHB inverter-based STATCOM," *IEEE Trans. Power Deliv.*, vol. 23, no. 3, pp. 1613–1619, 2008.

Appendix A.

Laboratory Setup

The validation of the IMMC was performed through experimental results. The testbench used for executing these analysis is described in this appendix.

6.1 Laboratory description

A block diagram of the converter setup and its hardware implementation are illustrated in Fig. 6.1 and Fig. 6.2 respectively. The converter has two modules per arm electrically connected through low frequency transformers. Each module is formed by a three-phase inverter, an ac filter, a measurement board and a control platform. On the other hand, the grid connection is performed through an autotransformer which is used for changing the amplitude of the grid voltage.

The main core of the local control embedded in each module is based on a DSP TMS320F28335 from Texas Instruments, which integrates the amplitude and quadrature voltage compensation techniques and a protection function for overvoltage and overcurrent detection. Similarly, the central control is also based on a DSP TMS320F28335 which includes the output and circulating current controllers in addition to the total energy loops. To control these signals, the central control measures the three phases of the current arms and the three phases of the output voltage. This last one is used to synchronize the converter to operate in a synchronous *dq* reference frame.

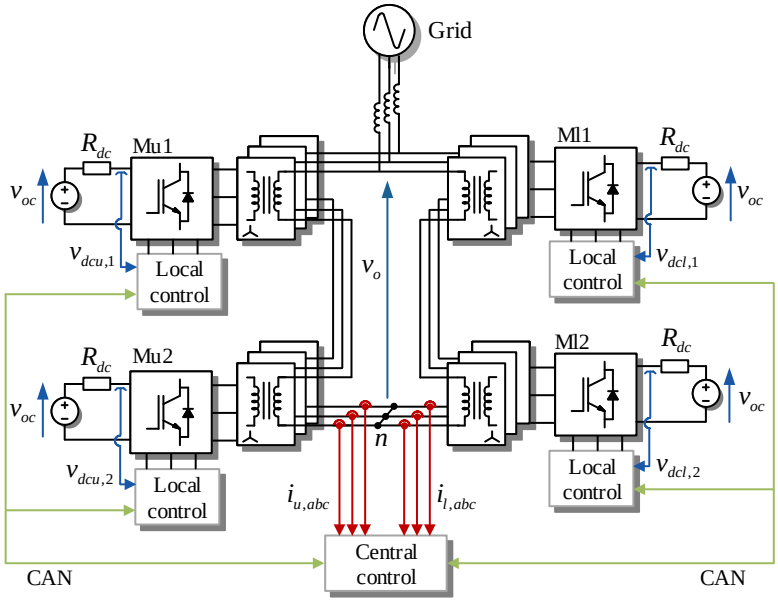

Fig. 6.1 Block diagram of testbench laboratory setup

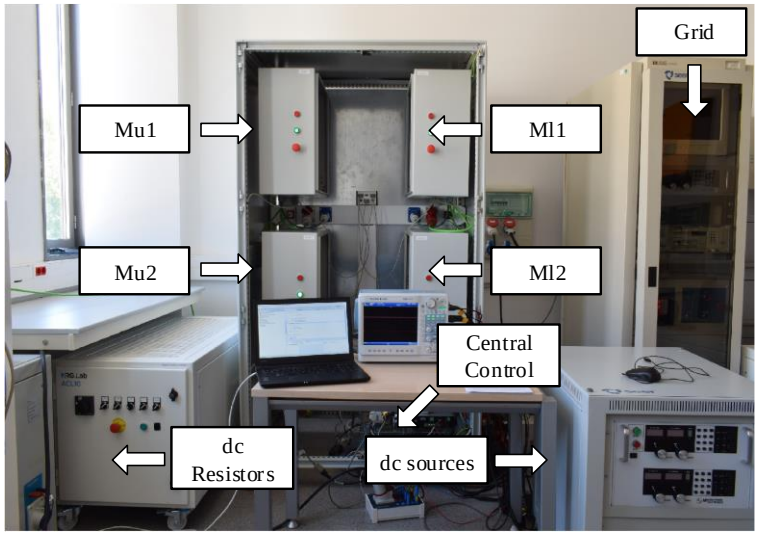

Fig. 6.2 Laboratory setup

The communication between all modules and the central control is performed through a Controller Area Network (CAN bus). This is a simple and low cost communication which provides a one point of entry to communicate all element, enabling central diagnostic and data logging. The data is transmitted in a frame sequentially among all devices with an

identification number which provides priorities, so that top priority data gets immediate bus access without interruption of other frames. In this case, the highest priority is given by the central control, which sends the modulation index, synchronous angle and status signals. References and control signals are set in a host computer connected to the central control via JTAG.

In order to emulate the PV characteristic, the dc side of each module is connected to a programmable dc source Magna-Power TSD1000-20/36 through a resistor, so they can operate between their maximum power level and zero. In order to understand the concept behind this, Fig. 6.3 illustrates the connection between one module with the programmable dc source. The dc voltage fluctuates between its maximum level $v_{\max}$ and the open circuit operation v_{oc}. When the dc voltage is $v_{\max}$, the power generated by each module is 1.2 kW. However, as the voltage $v_{dci,k}$ increases, the drop voltage in the resistor decreases. This reduces the current $i_{dci,k}$ and as a result the power generated.

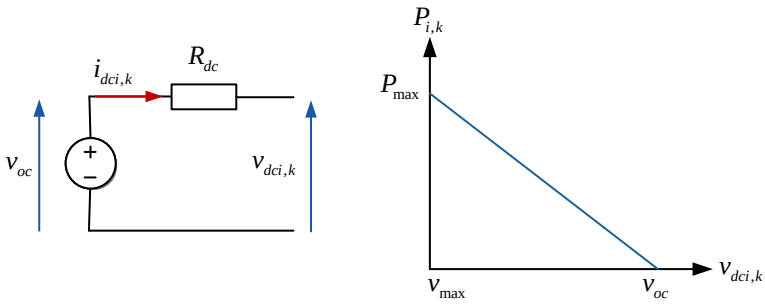

Fig. 6.3 Electrical representation of the programmable dc source connected to each module.

Power behavior based on dc voltage regulation

The power is defined based on the ratio between the voltage difference $v_{oc} - v_{dci,k}$ and the resistor R_{dc} multiplied by the voltage $v_{dci,k}$ as follows.

$$P_{dci,k} = \frac{\left(v_{oc} - v_{dci,k}\right)}{R_{dc}} \cdot v_{dci,k} \qquad \text{(A.1)}$$

The programmable dc source set the open circuit voltage level v_{oc} at 440V, while the maximum voltage is equal to 360V. All parameters of the testbench setup are described in Table 6.1.

Table 6.1 Parameters of experimental setup

Parameters	Symbol	Value
Grid and converter parameters		
Nominal power	P_T	4.8 kW
Nominal power per module	P_M	1.2 kW
Grid voltage (rms)	v_g	320 V
Grid frequency	f_s	50 Hz
Number of modules per arm	N	2
dc-link capacitor	C_{sm}	4.7 mF
Switching frequency	f_c	8.2 kHz
Inductance filter	L_f	3 mH
Capacitor filter	C_f	5 μF
Transformer parameters		
Transformer power	S_T	2 kW
Nominal voltage	V_T	400 V
Transformer ratio	r_t	1:1
Total winding inductance	L_T	8.3 mH
DC connection		
Voltage in open-circuit operation	V_{OC}	440V
Voltage in maximum power operation	V_{MPP}	360V
Resistor	R_{dc}	22.5 Ω

As mentioned, the series connection of modules is performed through the secondary side of transformers, while the primary side is connected to each module. Fig. 6.4 illustrates the transformers used in the laboratory setup and Fig. 6.5 shows a representation of their electrical connection. The primary side is connected in wye configuration, while the secondary side connects each phase in series. Note that the last transformer connects one terminal of all phases to a common point *n*.

Fig. 6.4 also illustrates the central control platform connected to the measurement board. Each board is equipped with LEM sensors to measure the current arms, while the output voltage is measured directly in the control platform.

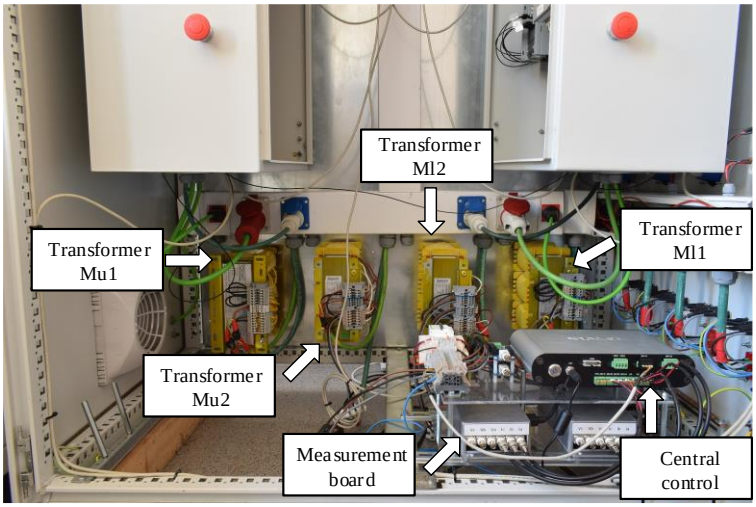

Fig. 6.4 AC transformers and central control platform

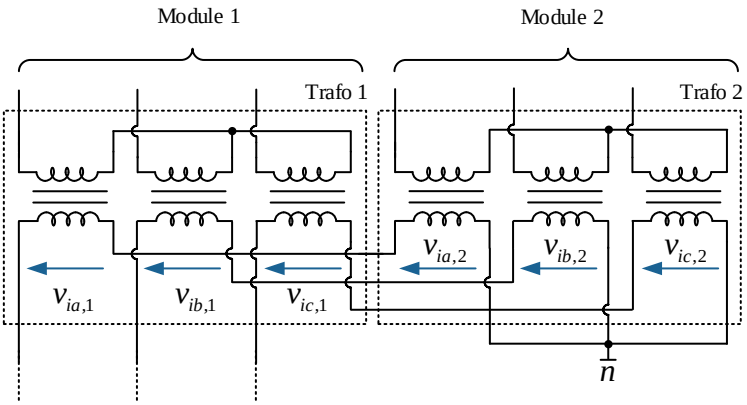

Fig. 6.5 Electric diagram of two transformers connected in series

In Fig. 6.2 each cabinet represents a module, which is formed by one inverter, a measurement board and a control platform. Fig. 6.6 illustrates the distribution of all these elements inside of the cabinet. The inverter is a 2L-VSC with a gate driver circuit coupled. The control signals are sent via fiber optic from the control platform to the gate driver while the current and voltage signals are measured in the measurement board and sent to adc channels. The electrical representation of one module is shown in Fig. 6.7.

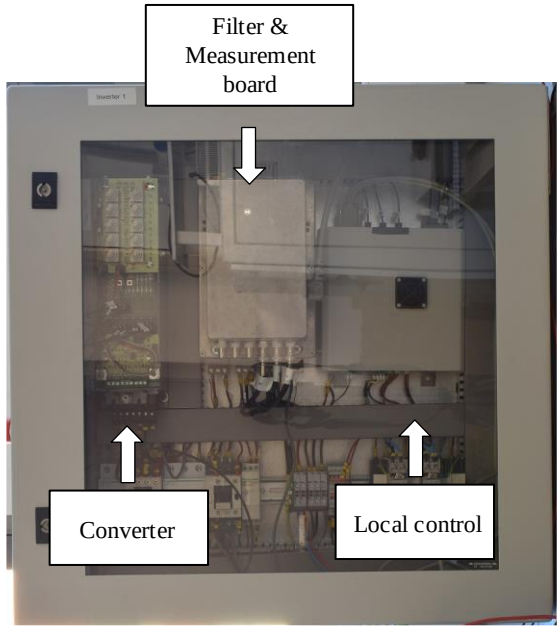

Fig. 6.6 Module configuration

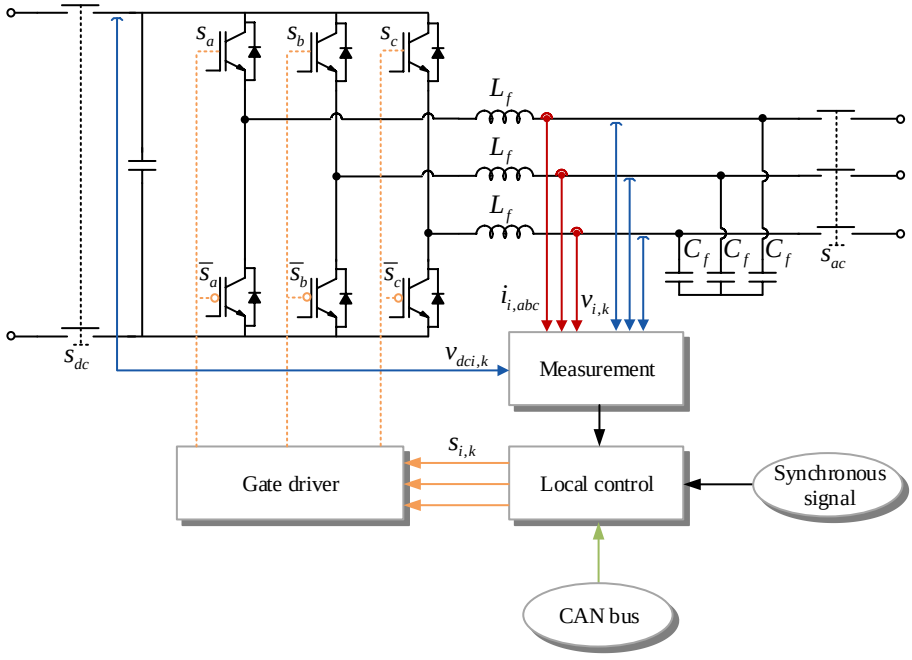

Fig. 6.7 Electrical representation of one module

Two breakers are connected to the dc and ac side which are commanded by external buttons. The ac filter has a LC configuration and is used to mitigate high switching components. The local control receives the data via CAN bus and a synchronous signal via fiber optic from the central platform. This synchronous signals is used to trigger the PWM modulation in each module with a certain phase angle, so the PS-PWM used in cascaded configurations is achieved.

To finalize, a diagram of the control platform implemented in the central and local controllers is illustrated in Fig. 6.8.

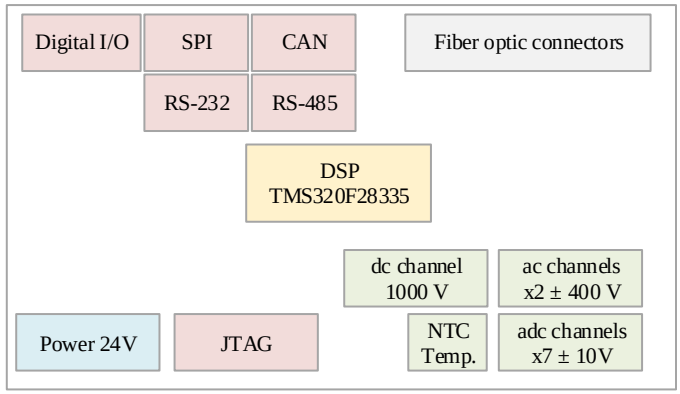

Fig. 6.8 Configuration of control platform.